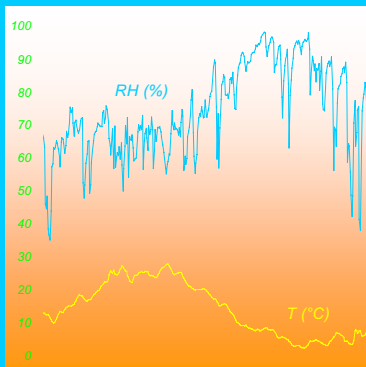


Diss. ETH No. 16567

# Modelling Indoor Climate and Salt Behaviour in Historical Buildings: A Case Study

Davide Bionda



DISS. ETH NO. 16567

**MODELLING INDOOR CLIMATE AND SALT BEHAVIOUR IN  
HISTORICAL BUILDINGS: A CASE STUDY**

A dissertation submitted to the  
SWISS FEDERAL INSTITUTE OF TECHNOLOGY ZURICH

for the degree of  
DOCTOR OF SCIENCES

presented by

**Davide Bionda**  
dipl. geol. University of Zurich

born 16.09.1968  
citizen of Preonzo (TI)

accepted on the recommendation of

Prof. Dr. Georg Mörsch, examiner  
Prof. Dr. Renato Zenobi, co-examiner  
Dr. Hans Simmler, co-examiner

2006



# Contents

<b>Abstract.....</b>	<b>iii</b>
<b>Zusammenfassung.....</b>	<b>iv</b>
<b>Riassunto .....</b>	<b>v</b>
<b>Acknowledgements.....</b>	<b>vi</b>
<b>1 INTRODUCTION.....</b>	<b>1</b>
1.1 Problem definition.....	1
1.2 Aims.....	2
1.3 Study object .....	3
<b>2 INDOOR CLIMATE .....</b>	<b>9</b>
2.1 Introduction.....	9
2.2 Methods .....	11
2.2.1 Monitoring.....	11
2.2.2 Thermal simulation .....	13
2.2.3 Hygic simulation.....	29
2.3 Results .....	36
2.3.1 Thermal simulation .....	36
2.3.2 Hygic simulation.....	42
2.3.3 Sensitivity tests.....	45
2.3.4 Building modifications and indoor climate .....	57
2.3.5 Reconstruction of past indoor climate.....	59
2.4 Discussion .....	63
<b>3 SALTS .....</b>	<b>66</b>
3.1 Introduction.....	66
3.2 Methods .....	70
3.2.1 Salt identification .....	70
3.2.2 Salt content of building materials.....	70
3.2.3 Critical relative humidities .....	70
3.2.4 ECOS simulations .....	71
3.2.5 Mineral saturation indexes .....	73



3.3	<i>Results</i> .....	74
3.3.1	Salt species and distribution on surfaces.....	74
3.3.2	Salt behaviour in relation to indoor climate .....	79
3.3.3	Soluble salts in building materials .....	82
3.3.4	ECOS simulations .....	85
3.3.5	Saturation state of pore solutions .....	89
3.3.6	Reconstruction of phase transitions in the past .....	91
3.4	<i>Discussion</i> .....	93
4	<b>CONCLUSIONS</b> .....	96
5	<b>REFERENCES</b> .....	99
	<b>Appendices</b> .....	105
	<b>Curriculum Vitae</b> .....	121

# Abstract

Indoor climate is a key factor determining the development of damage inside historical buildings. Processes like salt weathering are largely controlled by the temperature and the relative humidity of the environment.

In the present work hygrothermal simulations of the indoor climate of a church were performed with a novel hygric model used in combination with the HELIOS thermal code. The applicability of these models to a real, historical building was to be tested. The combination of HELIOS with the hygric model proved to be a viable method for hygrothermal simulations in historical buildings, provided that thermal simulations are as accurate as possible. Considerations on the quality of the relevant building parameters required for modelling are provided. The applicability of indoor climate models to historical buildings provides the opportunity to use these tools to perform risk assessment and investigations of the climatic conditions over a period of many years, without having to rely on long-term in situ measurements.

The behaviour of hygroscopic salts in relation to indoor climate was investigated. The principal salt species observed in the study building were mirabilite ( $\text{Na}_2\text{SO}_4 \cdot 10\text{H}_2\text{O}$ ), thenardite ( $\text{Na}_2\text{SO}_4$ ), epsomite ( $\text{MgSO}_4 \cdot 7\text{H}_2\text{O}$ ), trona ( $\text{Na}_3\text{H}(\text{CO}_3)_2 \cdot 2\text{H}_2\text{O}$ ) and niter ( $\text{KNO}_3$ ). No other activity in response to climate fluctuations than the phase transition between mirabilite and thenardite was observed. The ECOS thermodynamic model, which predicts the behaviour of salt mixtures in relation to climate, was tested by comparing simulation results with the observations of salt species growing on plasters. Results are presented for plasters on which efflorescences of mirabilite, thenardite and epsomite were detected. Saturation indexes for the relevant soluble salt species in the pore solutions were calculated. A correlation between efflorescences on the plasters and calculated saturation indexes has been observed.

# Zusammenfassung

Das Raumklima spielt eine sehr wichtige Rolle bei der Entstehung von Schäden in historischen Gebäuden. Schadensprozesse wie Salzverwitterung sind stark durch die Temperatur und die relative Feuchte der Umgebung kontrolliert.

In der vorliegenden Arbeit wurde das Raumklima einer Kirche anhand eines neuen hygrischen Modells, welches mit dem thermischen Gebäudesimulationsprogramm HELIOS kombiniert wurde, simuliert. Ziel war es, die Anwendbarkeit dieser Modelle an realen, historischen Gebäuden zu testen. Die Kombination von HELIOS mit dem hygrischen Modell erwies sich als geeignet, um Raumklimasimulationen in historischen Gebäuden durchzuführen, unter der Voraussetzung, dass die thermischen Simulationen möglichst sorgfältig durchgeführt werden. Die für die Simulation relevanten Gebäudeparameter werden dargestellt und diskutiert. Die Anwendung von Raumklimamodellen in historischen Gebäuden bietet die Möglichkeit, Risikoabschätzungen und Untersuchungen des Raumklimas während mehrjähriger Perioden durchzuführen, ohne dabei auf Langzeitmessungen in situ angewiesen zu sein.

Das Verhalten von hygroskopischen Salzen in Zusammenhang mit Raumklima wurde erforscht. Die wichtigsten, im untersuchten Gebäude beobachteten Salze waren Mirabilit ( $\text{Na}_2\text{SO}_4 \cdot 10\text{H}_2\text{O}$ ), Thenardit ( $\text{Na}_2\text{SO}_4$ ), Epsomit ( $\text{MgSO}_4 \cdot 7\text{H}_2\text{O}$ ), Trona ( $\text{Na}_3\text{H}(\text{CO}_3)_2 \cdot 2\text{H}_2\text{O}$ ) und Nitrokalit ( $\text{KNO}_3$ ). Die einzige festgestellte Salzaktivität in Zusammenhang mit den gemessenen Raumklimafluktuationen war die Phasenumwandlung zwischen Mirabilit und Thenardit. Das thermodynamische Modell ECOS, welches das Verhalten von Salzmischungen in Abhängigkeit vom Klima beschreibt, wurde getestet, indem die Ergebnisse der Simulationen mit den Beobachtungen der Salzspezies auf Verputzen verglichen wurden. Die entsprechenden Ergebnisse für Verputze mit Ausblühungen von Mirabilit, Thenardit und Epsomit werden dargestellt. Die Sättigungsindices der relevanten Salzspezies in Porenlösungen wurden berechnet. Eine Korrelation zwischen Salzausblühungen auf Verputzen und den berechneten Sättigungsindices wurde festgestellt.

# Riassunto

Il clima all'interno degli edifici storici svolge un ruolo determinante nello sviluppo di danni all'infrastruttura e agli oggetti. Fenomeni quali il degrado dovuto all'azione di sali igroscopici sono in gran parte controllati dalla temperatura e dall'umidità relativa dell'ambiente.

Nell'ambito di questo studio sono state eseguite delle simulazioni del clima all'interno di una chiesa con l'ausilio di un nuovo modello igrometrico usato in combinazione con il modello termico HELIOS. L'obiettivo era di verificare l'applicabilità di questi modelli ad edifici storici. La combinazione di HELIOS con il modello igrometrico si è dimostrata adatta per simulazioni del clima in edifici storici a condizione che le simulazioni termiche vengano eseguite con la massima accuratezza. I parametri dell'edificio riconosciuti come importanti per la modellizzazione vengono presentati e discussi. L'applicabilità di modelli termoigrometrici ad edifici storici permette di effettuare valutazioni del rischio e studi sul clima dell'ambiente interno per periodi pluriennali senza dovere far capo a misurazioni in situ a lungo termine.

Il comportamento dei sali igroscopici è stato studiato in relazione alle fluttuazioni climatiche misurate. I principali sali osservati nell'edificio in questione sono mirabilite ( $\text{Na}_2\text{SO}_4 \cdot 10\text{H}_2\text{O}$ ), tenardite ( $\text{Na}_2\text{SO}_4$ ), epsomite ( $\text{MgSO}_4 \cdot 7\text{H}_2\text{O}$ ), trona ( $\text{Na}_3\text{H}(\text{CO}_3)_2 \cdot 2\text{H}_2\text{O}$ ) e nitrato di potassio ( $\text{KNO}_3$ ). L'unica reazione alle fluttuazioni climatiche osservata è stata la transizione di fase tra mirabilite e tenardite. Il modello termodinamico ECOS, il quale descrive il comportamento di miscele di sali in funzione del clima, è stato testato paragonandone i risultati con le osservazioni delle efflorescenze sugli intonaci. Vengono presentati i risultati delle simulazioni relative agli intonaci con efflorescenze di mirabilite, tenardite ed epsomite. Per i sali rilevanti sono stati calcolati gli indici di saturazione nelle soluzioni acquose del sistema poroso degli intonaci. Si è notato che questi indici correlano con le efflorescenze osservate sugli intonaci.

# Acknowledgements

I would like to sincerely thank:

- Prof. Dr. Georg Mörsch for the opportunity to carry out this study and for agreeing to advise this thesis.
- Prof. Dr. Renato Zenobi for kindly accepting on short notice to co-advise this thesis.
- Dr. Konrad Zehnder who started this project, thoroughly introduced me to the field of conservation science and very generously assisted and supported me for the whole duration of this work.
- Dr. Hans Simmler (EMPA) for co-advising this thesis and for valuable support and competent advice particularly on the aspects of the study pertaining building physics and modelling.
- Prof. Dr. Ing. Uta Hassler for allowing a three-months extension of the project grant.
- Dr. Christine Bläuer Böhm and Dr. Per Storemyr (Expert-Center Zürich) for continuous competent advice, discussions, comments and proof-reading of parts of the manuscript.
- Thomas Frank (EMPA) for introducing me to HELIOS and for providing me a modified version of the program.
- Roger Vonbank (EMPA) for sorption tests of building materials in climate chambers.
- Andreas Küng (Expert-Center Zürich) who kindly offered his know-how whenever I needed help for salt identification by means of microscopy.
- Adam Krzystek (Expert-Center Zürich) for excellent laboratory support.
- Dr. Bénédicte Rousset (Expert-Center Lausanne) for porosity determination of mortars.
- Dr. Michael Steiger (University Hamburg) for the helpful discussions on salt chemistry.
- Alexander Voûte (Swiss National Museum) for Gandolfi camera analyses of some salts.
- Dr. Günter Kahr for XRD analyses of some mortar samples.
- Architect Werner Schaub for providing invaluable information and documentation about the church San Pietro Martire.
- Bruna Schaub for kindly providing service attendance data for the church San Pietro Martire.
- The Parish of Gnosca for giving me the opportunity to use the church San Pietro Martire as a study object and for allowing unrestricted access to the building.
- Dr. Giovanna Di Pietro, Katja Feldmann, Kathrin Hauri, Susanne Mühlhaus Ebersole, Dr. Marcel Stalder and Dr. Sophie Wolf for discussions and for making this time enjoyable.
- My father Plinio for his readiness to help whenever necessary during fieldwork.
- My greatest thanks goes to Silvia, the most patient human being in the universe, for her continuous and unconditional support, encouragement, help and interest in this work.

# 1 INTRODUCTION

## 1.1 Problem definition

Indoor climate is a key factor determining the development of damage inside historical buildings. Processes like salt weathering, swelling and shrinking of materials as well as growth of microorganisms are largely controlled by the temperature and the relative humidity of the environment.

It is one of the aims of preventive conservation studies to attempt to limit damage by gaining a better understanding and control of the indoor environmental conditions. This usually implies in situ monitoring of air temperature and humidity. An estimation of the indoor climate during prolonged periods can however also be achieved by modelling, a valuable tool which allows to generate large amounts of data without having to rely on long-term measurements. Yet, while indoor climate simulation tools are generally used by building physics specialists, their use among conservation scientists is still not popular.

Building energy simulation programs are usually employed during the planning phase of new buildings to answer questions pertaining to energy consumption and human comfort. They have reached nowadays a degree of reliability that allows to compute the indoor air temperature with high accuracy (e.g. DOE-2, EnergyPlus, ESPr, HELIOS and TRNSYS). On the contrary, and despite the fact that hygroscopic materials play an important role in the humidity balance of indoor air, models able to simulate indoor air humidity taking into account the sorption characteristics of building components are rare and their development is still in progress. Known codes are actually research tools that are not yet ready for a general use. These include: HAMLab/HAMBase (Schijndel and Hensen, 2005; Wit, 2004); WUFI<sup>®</sup>+ (Holm et al., 2003; Künzle et al., 2005); the International Building Physics Toolbox software library (Weitzmann et al., 2003); the hygric model from Simmler et al. (1995; 1996).

The lack of established, fully validated, whole building hygrothermal programs is a major drawback when modelling is supposed to be applied to investigations within the context of conservation sciences. Air humidity plays a crucial role in the formation of climate-related damage and it is therefore essential to be able to rely on accurate data.

One of the processes that is largely controlled by relative humidity and temperature is salt weathering, which is generally acknowledged as one of the major factors leading to the deterioration of porous building materials. Environmental control has long been proposed as a possible method for avoiding or limiting damage (Arnold and Zehnder, 1991; Price and Brimblecombe, 1994). This means keeping temperature and relative humidity in ranges where salt weathering activity is reduced to a minimum. The thermodynamic relationships linking the behaviour of common hygroscopic salts or simple salt mixtures to the environmental conditions are generally known both theoretically, as well as from laboratory experiments.

For multi-component salt mixtures, which are commonplace in building materials, the complexity of the interactions involved and the lack of experimental data for every possible salt combination impose the use of models. A thermodynamic model for predicting the behaviour of such mixtures in relation to temperature and relative humidity has been developed (Price, 2000), but published results of its application are still rare.

In order to optimise indoor climate and salt models, and to make them more useful for applications in the field of the preventive conservation, there is thus a need to assess their validity and applicability to full-scale buildings under real situations.

## **1.2 Aims**

The aims of the present thesis are:

- Test a combination of a novel hygric model with a thermal code for simulations in a real, historical building. The hygric model is based on Simmler et al. (1995; 1996) and has been recently further developed by H. Simmler (EMPA<sup>1</sup>, Laboratory for Applied Physics in Building). So far it has only been tested in climate chambers under strictly controlled conditions; there are no studies available assessing its validity and applicability to a real, full-scale building. The hygric model is to be tested in combination with the thermal code HELIOS (Frank, 1982; Frank et al., 1982-1992). At present, there are plans at EMPA to integrate the two codes into a single program.
- Investigate the behaviour of hygroscopic salts in a historical building and their relationship to indoor climate conditions.
- Test the thermodynamic model ECOS (Price, 2000). The model is to be used to predict the behaviour of salt mixtures present in the walls of a historical building; the results are to be compared with in situ observations.

---

<sup>1</sup> Swiss Federal Laboratories for Materials Testing and Research.

### 1.3 Study object

The investigations were carried out in the church San Pietro Martire, located in Gnosca, southern Switzerland (Fig. 1-1 and Fig. 1-2). The church was suitable and interesting as study object for the present research because of the following reasons:

- Presence of climate-related damage, especially salt weathering features.
- Presence of efflorescences of a fairly wide variety of salt species.
- Possibility to perform sampling of building materials and salt efflorescences at various locations and to gain an insight into the structures underneath the floor.
- Relative proximity (about 20 km of distance) to a suitable meteorological station lying approximately at the same altitude as the study object (366 m above sea level vs. ca. 300 m) and providing the full suite of meteorological parameters needed for the climatic simulations.
- Lack of permanent heating in the building: significant daily and seasonal fluctuations of the indoor climate are to be expected, potentially having a major impact on the behaviour of the present salts.
- Opportunity to follow the evolution of the indoor climate during a major building intervention (floor removal and archaeological excavation).
- Possibility to install equipment for monitoring indoor climate and to have unrestricted access to the whole building at any time.

The church (or probably a smaller precursor building) is already mentioned in documents from the 13<sup>th</sup> century. The building underwent several modifications and restorations during the centuries; noteworthy is the adaptation to the baroque style during the 17<sup>th</sup> century that still predominates today's appearance of the interior. The last important interventions outside and inside the church were carried out in the early seventies of the last century, when large parts of the plasters were repaired and the walls were repainted with emulsion paint.

Objects of particular interest for their historical value are the painted block altar (15<sup>th</sup> century), discovered during the archaeological excavations in June 2003 (Fig. 1-2, bottom right), as well as the wooden gilded ciborium (Fig. 1-2, left), the wall paintings and stuccoes (16<sup>th</sup> and 17<sup>th</sup> century). Further information on the church can be found in Anderes (1998), Gilardoni (1972) and Schmid (1976), as well as in unpublished reports by the architects Ambrosetti and Martella (1991) and the conservators (CGB, 2000).

The principal materials (Fig. 1-3) and types of damage (Fig. 1-4 and Fig. 1-5) present in the building were assessed, mapped in detail and integrated into a geographic information system (GIS). The damage observed includes flaking of the paint layer, salt efflorescence and, to a minor extent, sanding and crumbling of plaster surfaces. Cracks, mostly of static nature, were observed especially in the upper part of the edifice.





**Fig. 1-1.** The church San Pietro Martire in Gnosca, southern Switzerland. Left: before 1968 (picture from Bianconi and Vicari, 1968). Right: October 2002.



**Fig. 1-2.** Left: View of the interior of the church from the nave, with the chancel and the wooden gilded ciborium in the background. The pews have been removed in the course of renovation works. Top right: view of the nave, the lateral apses on the SE side and the entry door. Bottom right: Front view of the block altar from the 15<sup>th</sup> century, painted in the style of Antonio da Tradate, that was discovered in June 2003 by the cantonal archaeological service in the course of excavations. The altar was buried under the mensa that is visible in the left picture. The dimensions of the altar (WxDxH) are 145 x 120 x 100 cm.



**Fig. 1-3.** Maps of the principal materials present in the church.



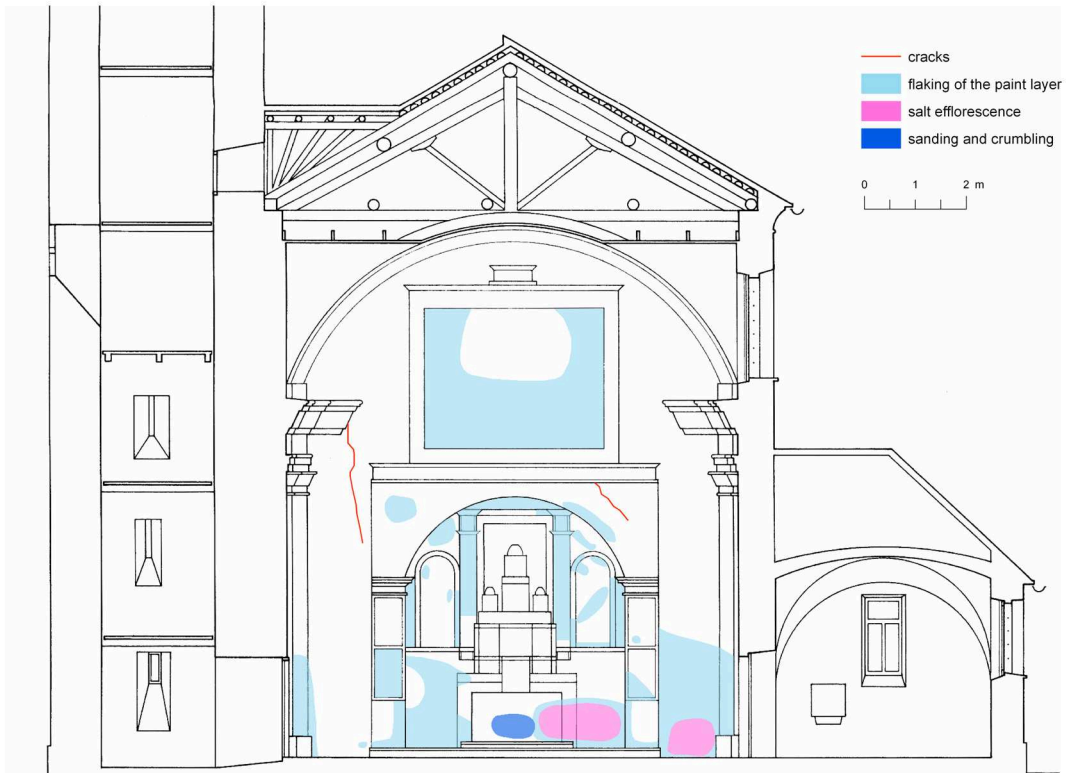


**Fig. 1-4.** Damage maps of the NE side (top) and of the SW side (bottom) showing the principal types of damage present in the church.

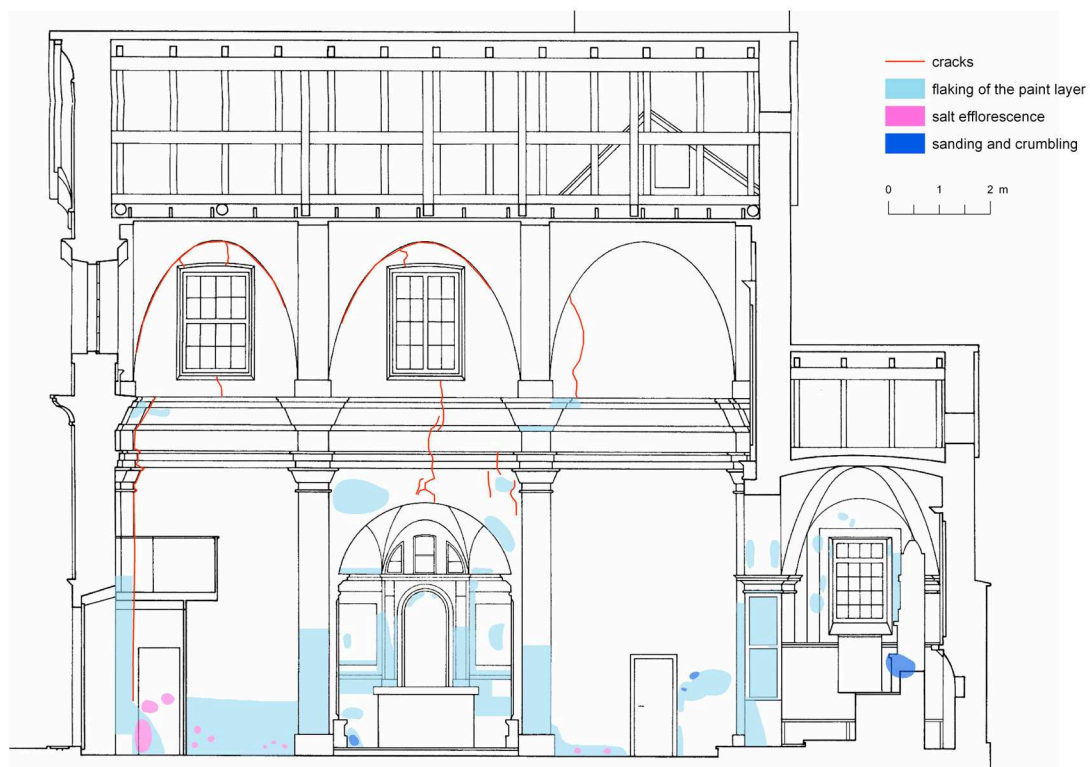


**Fig. 1-5.** Damage maps of the NW side (top) and of the SE side (bottom) showing the principal types of damage present in the church.

## 2 INDOOR CLIMATE

### 2.1 Introduction

The indoor climate in a building depends essentially on four factors: outdoor climate, building construction, usage and HVAC (Heating, Ventilation and Air Conditioning) systems (Fig. 2-1).

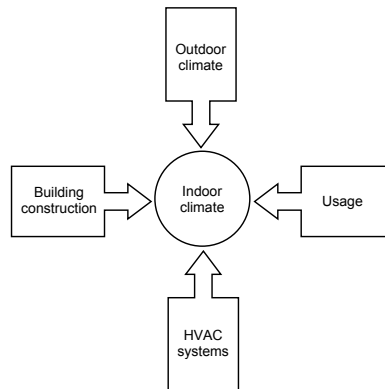


**Fig. 2-1.** Principal factors influencing the indoor climate of buildings.

Indoor climate plays a major role in the deterioration processes that take place inside historical buildings. Finding the best environmental conditions for the preservation of a given object is one of the challenges of conservation sciences. Computer simulation of the indoor climate is an important tool to gain more knowledge about these systems. Its application requires the availability of meteorological data and detailed information about building characteristics, usage and HVAC systems.

Many of the available models are designed and tested for the simulation of the climate in modern edifices and are usually used during the planning phase of new buildings in order to investigate questions pertaining energy consumption, human comfort and health. Their application to historical buildings entails some difficulties bound to the peculiarities of old constructions, in particular to the fact that not all the building characteristics are exactly known. The materials employed can be quite varied and irregularly distributed due to interventions performed and alterations occurred in the course of time. Their composition and hygrothermal properties, which are essential parameters for the modelling, have often to be determined experimentally or approximated. Experimental determination requires destructive sampling, which is in most cases not acceptable. It is therefore of particular interest to know to which extent parameter uncertainties can affect the results of the indoor climate simulations with a given model.

This chapter deals with the parameterisation and application of a thermal and a hygric model for the simulation of the climate inside an old historical building. The aim is to determine their predictive accuracy and suitability in the context of sustainable conservation.

In order to test the applicability of the models and the correctness of their parameterisation, the results were compared with actual measurements of temperature and humidity carried out in the study object. The influence of the variation of the principal building parameters on the results of the simulations was assessed by means of sensitivity tests. Examples of possible applications of the models are presented.

For the simulation of the temperature of indoor air and surfaces, the MS-DOS<sup>®</sup> computer program HELIOS (Frank, 1982; Frank et al., 1982-1992) has been used. HELIOS is an established building energy simulation code, which is well suited for simulations in Switzerland thanks to the availability of the required meteorological data in the proper format for over 70 Swiss localities. The temperatures calculated by HELIOS served as a basis for simulations with the hygric model, so it was particularly important to take care that the parameterisation was as accurate as possible.

The indoor air humidity has been simulated using a novel hygric model based on Simmler et al. (1995; 1996) that has been recently further developed by H. Simmler (EMPA, Laboratory for Applied Physics in Building). Until now, this model has only been tested under the strictly controlled conditions of climate chambers at EMPA. The present work is the first application of the hygric model to a real building and may be considered as a benchmark for its further development and refinement. Testing the specific combination of HELIOS with the abovementioned hygric model was of particular interest in view of EMPA's plans to integrate the two codes into a single computer program.

In addition, a simple thermal model, based on 1-dimensional heat transfer and relying on a reduced set of input parameters and easily available meteorological data, was developed and tested in the course of this study. The model was used to gather information about the heat distribution across wall sections and to test the possibility to simulate indoor temperatures with a minimal amount of climatological and building information.

Monitoring of the temperature and humidity inside the church provided the data for validating the results of the simulations and allowed a characterisation of the indoor climate conditions. It was also essential in order to gather reliable information to establish possible relationships between indoor climate and observed damage, in particular damage caused by salt weathering on building materials (chapter 3).

## 2.2 Methods

### 2.2.1 Monitoring

Temperature and relative humidity were monitored by means of sensors/data loggers beginning from April 2002. The sensors were placed at different locations inside (3 in the nave and 1 in the attic) and outside (1) the building (Fig. 2-2).

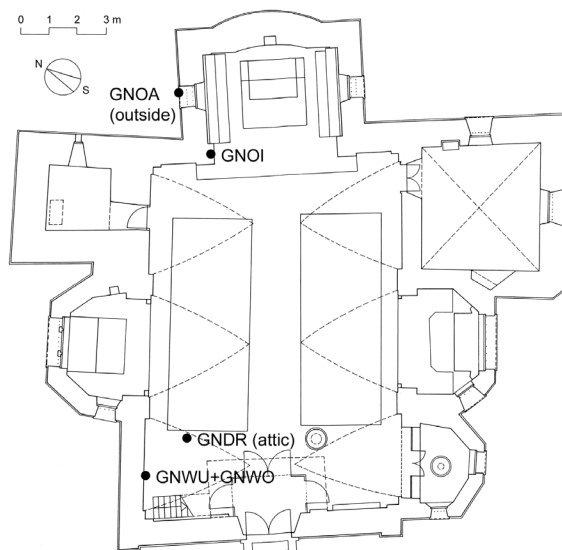


**Fig. 2-2.** Location of the temperature and RH sensors/data loggers. GNOI, GNWU and GNWO are inside the church, GNDR in the attic and GNOA outside.

The sensor GNOI, on the cornice under the arch between nave and chancel, at a height of 7 m above the floor, was aimed at getting a record of the mean air temperature and RH inside the nave and the chancel. Preliminary measurements with a portable precision thermometer proved that the temperature at this position is representative of an average indoor temperature. The sensors GNWU and GNWO, fixed on the NW wall, the first at 2.4 m and the latter at 4.4 m height, recorded the temperature of the wall surface as well as the temperature and the RH of the air at a distance of 5 cm from the wall. The sensor GNDR measured the temperature and the RH of the air in the attic. The sensor GNOA was fixed at the window grating on the NW wall of the chancel outside the church, sheltered from direct sunlight and precipitation, and measured the temperature and the RH of the air. The interval between each measurement was set to 1 hour for every sensor, providing a time resolution that is sufficient to document variations relevant for salt crystallization processes. Monitoring was carried out with the sensors/data loggers Testo testostor 171-2 (accuracy  $\pm 0.4$  °C [-10 to +50 °C],  $\pm 2\%$  RH [2 to 98% RH]), Testo testostor 171-6 (accuracy  $\pm 0.4$  °C [-10 to +50 °C],  $\pm 2\%$  RH [2 to 98% RH]) and Testo 177-H1 (accuracy  $\pm 0.5$  °C [-20 to +70 °C],  $\pm 2\%$  RH [0 to 100% RH]).



The spatial and temporal distribution of the temperature of the indoor building surfaces was determined by infrared thermography using a FLIR Systems ThermaCAM PM 545 IR camera. The thermographs (some examples are in Appendix D) were taken during the different seasons and throughout the day in order to record possible variations.

The attendance during the liturgical services was documented by a person who regularly frequented the worships. Information about the usual heating schedule was provided by the sacristan of the church.

## 2.2.2 Thermal simulation

### 2.2.2.1 HELIOS thermal model

#### 2.2.2.1.1 Model

The HELIOS building energy simulation program (Frank, 1982; Frank et al., 1982-1992) was developed during the period 1982-1992 in the frame of a project supported by the Swiss National Science Foundation and the Swiss Federal Office of Energy. The aim of the project was the determination of the influence of short- and long wave radiation processes on the energy balance of buildings.

HELIOS is a dynamic 1-zone simulation code that can predict the thermal performance of a building by explicitly solving the heat balance equations in 1-hour time steps. Transient heat conduction processes through the building elements are solved with the method of the thermal response factors using Laplace transforms (see e.g. Kusuda, 1969; Mitalas, 1968; Stephenson and Mitalas, 1967). Being, as said, a 1-zone model, HELIOS can simulate the air and surface temperatures of spaces inside a building showing equal climate. A simplified schematic representation of the principal quantities involved is shown in Fig. 2-3.

Of principal interest for this work is the ability of HELIOS to compute the temperature of the indoor air and of the internal building surfaces. These temperatures serve as a basis for the hygric simulation.

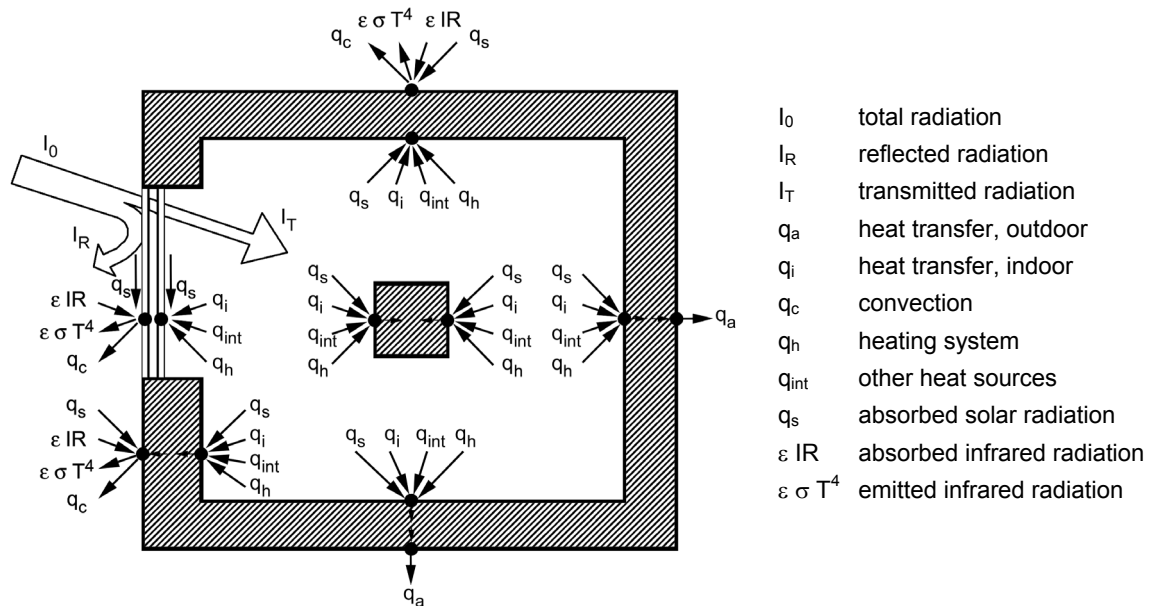
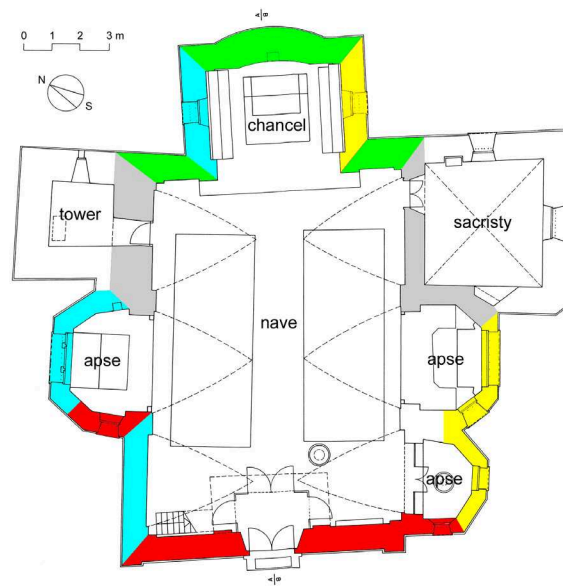


Fig. 2-3. Schematic representation of the heat balance model of HELIOS. Modified after Frank et al. (1999).

The input parameters required by HELIOS were determined on the basis of detailed in situ investigations. The present section deals with those features of the building that need to be described and discussed in more detail. The complete HELIOS input file, compiled according to this section, is attached in Appendix B and will be regarded as reference model.

The zone considered for the simulation comprised the nave, the chancel and the 3 lateral apses. The attic, the tower and the sacristy have a different climate and were treated as buffer zones, acting as thermal resistances between the internal and the external environment. The external walls were considered as having four main orientations (Fig. 2-4). The walls markedly deviating from these four main orientations (e.g. in the apses) correspond to only about 5% of the total external wall surface and were approximated as shown.



**Fig. 2-4.** Plan of the church showing the zone of interest for the simulation (nave, chancel and apses), the buffer zones (sacristy and tower) with the respective walls (grey) and the four main orientations of the external walls (green, yellow, red and cyan).

The internal and external heat transfer coefficients  $AI$  and  $AA$  required by HELIOS were derived from the relations

$$AI = \frac{1}{R_{si}} \quad (\text{W m}^{-2} \text{ K}^{-1}) \quad (2-1)$$

$$AA = \frac{1}{R_{se}} \quad (\text{W m}^{-2} \text{ K}^{-1}) \quad (2-2)$$

where  $R_{si}$  and  $R_{se}$  are the internal and the external surface resistance as given in Table 2-1. For the floor, the ceiling and the walls separating the nave from the tower and the sacristy,  $AA$

cannot be simply determined using (2-2), because these structures are not in direct contact with the outdoor climate. In these cases, a specific external heat transfer coefficient is calculated taking into account the additional resistance of the soil and of the buffer zones between internal and external environment.

**Table 2-1.** Internal ( $R_{si}$ ) and external ( $R_{se}$ ) surface resistances (Standard ISO 6946, 1996).

	Direction of heat flow		
	Upwards	Horizontal	Downwards
$R_{si}$ ( $\text{m}^2 \text{ K W}^{-1}$ )	0.10	0.13	0.17
$R_{se}$ ( $\text{m}^2 \text{ K W}^{-1}$ )	0.04	0.04	0.04

### 2.2.2.1.2 External walls

The external walls of the church are made of masonry consisting mainly of granitic gneiss stones with minor amounts of lime mortar. The internal and the external surfaces are plastered with a cement mortar. The thickness of the plaster was found at a few spots inside and outside the building to be on average about 4 cm. The total thickness of the external walls ranges from 60 cm (apses on the southeast side) to about 90 cm. The thermophysical properties of the materials constituting the external walls were defined on the basis of SIA standards and are summarized in Table 2-2.

On the exterior, the façade is painted with a pink colour, while the rest of the church is white. The absorptivity of the white-painted external plaster was determined analytically<sup>2</sup> because preliminary simulation runs showed an appreciable sensitivity of the model to variations of this parameter (see section 2.3.3). A value of 0.32 was used. For the façade, a value of 0.55, corresponding to orange-coloured plaster (HELIOS database) was used. The emissivity was set to 0.97 (HELIOS database) for all external wall surfaces.

**Table 2-2.** Thermophysical properties of the materials constituting the external walls, as input into HELIOS.

	thickness (m)	thermal conductivity* ( $\text{W m}^{-1} \text{ K}^{-1}$ )	density* ( $\text{kg m}^{-3}$ )	specific heat* ( $\text{W h kg}^{-1} \text{ K}^{-1}$ )
external plaster	0.040	0.870	1800	0.30
masonry	0.520-0.820	1.100	2000	0.26
internal plaster	0.040	0.700	1400	0.26
* (Standard SIA 381/1, 1980)				

<sup>2</sup> The reflectivity of the white-painted external plaster was determined by EMPA to be 0.676. Since  $\rho + \alpha = 1$ , where  $\rho$  is the reflectivity (-) and  $\alpha$  the absorptivity (-), the resulting absorptivity is 0.324.

### 2.2.2.1.3 Floor

The upper part of the floor (Fig. 2-5) consists of 2-cm-thick cement tiles placed over a layer of cement mortar of 2-4 cm thickness. Below that level there are two older floors made of lime mortar, each about 10 cm thick, separated by a ca. 20-cm-thick stone bed. The basal surface of the lowest lime floor is partly in direct contact with the soil and partly rests on the masonry vestiges of a precursor, smaller chapel. The thermophysical properties of the materials constituting the floor were defined on the basis of SIA standards, as summarized in Table 2-3.

The thermal transmittance  $U$  between the internal and the external environment through the floor can be calculated using equations (2-3), (2-4) and (2-5) (Standard EN ISO 13370, 1998)

$$B' = \frac{2A}{P} \quad (2-3)$$

$$d_t = w + \lambda (R_{si} + R_f + R_{se}) \quad (2-4)$$

for uninsulated and moderately insulated floors ( $d_t < B'$ ) without edge insulation

$$U = \frac{2\lambda}{\pi B' + d_t} \ln \left( \frac{\pi B'}{d_t} + 1 \right) \quad (\text{W m}^{-2} \text{ K}^{-1}) \quad (2-5)$$

where  $B'$  is the characteristic dimension of the floor (m),  $A$  is the area of the floor ( $\text{m}^2$ ),  $P$  is the exposed perimeter of the floor (m),  $d_t$  is the total equivalent thickness of the floor (m),  $w$  is the thickness of external walls (m),  $\lambda$  is the thermal conductivity of the unfrozen ground ( $\text{W m}^{-1} \text{ K}^{-1}$ ),  $R_{si}$  is the internal downwards surface resistance ( $\text{m}^2 \text{ K W}^{-1}$ , Table 2-1),  $R_f$  is the thermal resistance of floor construction ( $\text{m}^2 \text{ K W}^{-1}$ ) and  $R_{se}$  is the external downwards surface resistance ( $\text{m}^2 \text{ K W}^{-1}$ , Table 2-1).

The external heat transfer coefficient  $AA$  required by HELIOS was obtained by subtracting the internal surface resistance and the thermal resistance of the floor from the total thermal resistance  $1/U$  between internal and external environment

$$AA = \frac{1}{\frac{1}{U} - R_{si} - R_f} \quad (\text{W m}^{-2} \text{ K}^{-1}) \quad (2-6)$$

By setting the appropriate values in equations (2-3) to (2-6), the resulting  $AA$  of the floor is  $0.46 \text{ W m}^{-2} \text{ K}^{-1}$ .

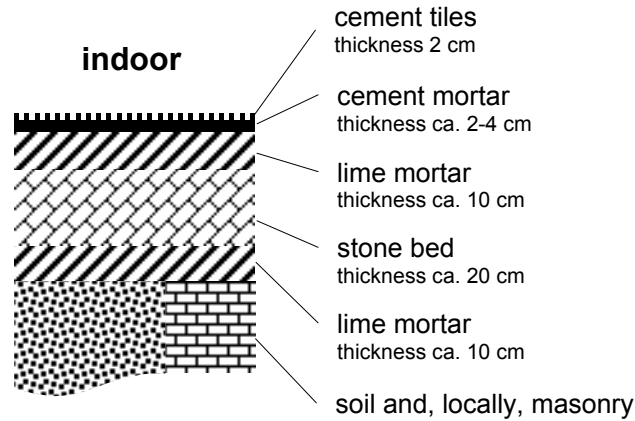


**Fig. 2-5.** Structure of the floor.

**Table 2-3.** Thermophysical properties of the materials constituting the floor, as input into HELIOS.

	thickness (m)	thermal conductivity* (W m <sup>-1</sup> K <sup>-1</sup> )	density* (kg m <sup>-3</sup> )	specific heat* (W h kg <sup>-1</sup> K <sup>-1</sup> )
cement tiles	0.020	1.500	2200	0.30
cement mortar	0.030	1.500	2200	0.30
lime mortar	0.100	1.000	1900	0.30
stone bed	0.200	1.100	2000	0.26
lime mortar	0.100	1.000	1900	0.30

\* (Standard SIA 381/1, 1980)

#### 2.2.2.1.4 Buffer zones

Buffer zones are unheated (attic and tower) or sporadically heated (sacristy) parts of the building, whose climate is significantly different from that in the rest of the church. These zones, together with their external construction components, can be treated as additional thermally homogeneous layers having a specific thermal resistance.

In HELIOS, the construction elements separating the nave from the buffer zones were entered as walls in contact with a constant climate. The internal heat transfer coefficient  $AI$  was derived from (2-1). The external heat transfer coefficient  $AA$ , taking into account the thermal resistance of the buffer zone, was obtained using the expression

$$AA = \frac{1}{R_{bz} + R_{se}} \quad (\text{W m}^{-2} \text{ K}^{-1}) \quad (2-7)$$

where  $R_{bz}$  is the thermal resistance of the buffer zone including its external construction components (m<sup>2</sup> K W<sup>-1</sup>) and  $R_{se}$  is the external surface resistance according to Table 2-1 (m<sup>2</sup> K W<sup>-1</sup>).

The attic is an unheated, moderately ventilated zone between the ceiling of the nave and the pitched roof. It has a rudimentary floor, which is made of wooden planks and which is suspended above the vaulted ceiling. The roof is made of 5 to 6-cm-thick gneiss slates lying on a wooden framework, closed towards the inner side with 3-cm-thick wooden boards waterproofed with a 2-mm-thick asphalt sheet. The vaulted ceiling is made of stucco (lime mortar, partly mixed with straw) on a framework of wood and interlaced branches (Fig. 2-6). The lower side, facing the nave, is plastered with lime mortar. The total thickness of the ceiling is of about 10 cm. The upper side is covered with a 1-cm-thick layer of dust, sand and wood fragments originating from the overhanging structures. The thermophysical properties of the materials constituting the ceiling were defined on the basis of SIA standards, as summarized in Table 2-4. The external heat transfer coefficient  $AA$  required by HELIOS was obtained by setting  $R_{bz} = 0.2 \text{ m}^2 \text{ K W}^{-1}$  (thermal resistance of ventilated roof space with pitched roof construction, Standard ISO 6946, 1996) and  $R_{se} = 0.04 \text{ m}^2 \text{ K W}^{-1}$  (Table 2-1) in equation (2-7) and corresponds to  $4.17 \text{ W m}^{-2} \text{ K}^{-1}$ .

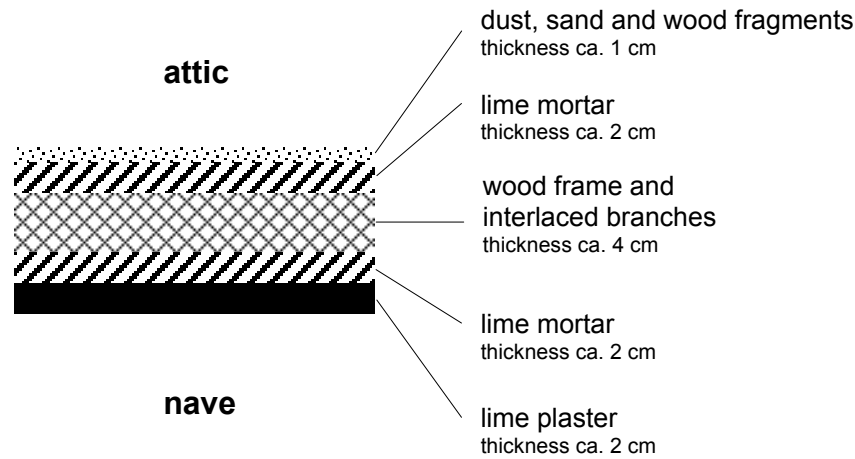


**Fig. 2-6.** Structure of the ceiling.

**Table 2-4.** Thermophysical properties of the materials constituting the ceiling of the nave, as input into HELIOS.

	thickness (m)	thermal conductivity* ( $\text{W m}^{-1} \text{ K}^{-1}$ )	density* ( $\text{kg m}^{-3}$ )	specific heat* ( $\text{W h kg}^{-1} \text{ K}^{-1}$ )
sandy debris	0.010	0.700	1900	0.22
lime mortar	0.020	0.870	1800	0.30
wood	0.040	0.140	470	0.60
lime mortar/plaster	0.040	0.870	1800	0.30

\* (Standard SIA 381/1, 1980)

The structure of the other vaulted ceilings present in the church (i.e. in the chancel and in the apses) was neither visible nor accessible. Therefore, the roof spaces in these zones were included in the calculations together with the attic, under the assumption that they yield a similar thermal resistance.

The walls separating the nave from the tower and the sacristy are made of masonry with minor amounts of lime mortar and are plastered on both sides with a cement mortar. The thickness of the plaster was determined at a few spots in the nave to be of about 4 cm. The total thickness of the walls is 70 cm (nave-sacristy) and 140 cm (nave-tower). The thermophysical properties of the materials constituting these walls were defined on the basis of SIA standards, as summarized in Table 2-5. The thermal resistance of the sacristy and the tower was estimated using the following expression (Standard ISO 6946, 1996)

$$R_{bz} = 0.09 + 0.4 \frac{A_i}{A_{bz}} \quad (\text{m}^2 \text{ K W}^{-1}) \quad (2-8)$$

which is valid for  $R_{bz} \leq 0.5 \text{ m}^2 \text{ K W}^{-1}$ , where  $A_i$  is the total area of all components between internal environment and buffer zone and  $A_{bz}$  is the total area of all components between buffer zone and external environment. The external heat transfer coefficient  $AA$ , obtained by setting  $R_{bz} = 0.19 \text{ m}^2 \text{ K W}^{-1}$  (cubical room,  $A_i/A_{bz} = 1/4$ ) and  $R_{se} = 0.04 \text{ m}^2 \text{ K W}^{-1}$  (Table 2-1) in equation (2-7) corresponds to  $4.35 \text{ W m}^{-2} \text{ K}^{-1}$ .

**Table 2-5.** Thermophysical properties of the materials constituting the wall between nave and sacristy and between nave and tower, as input into HELIOS.

	thickness*	thermal conductivity*	density*	specific heat*
	(m)	(W m <sup>-1</sup> K <sup>-1</sup> )	(kg m <sup>-3</sup> )	(W h kg <sup>-1</sup> K <sup>-1</sup> )
plaster	0.040	0.700	1400	0.26
masonry	0.62 (nave-sacristy) 1.32 (nave-tower)	1.100	2000	0.26
plaster	0.040	0.700	1400	0.26
* (Standard SIA 381/1, 1980)				

#### 2.2.2.1.5 Furniture

Furniture, as every material, can contribute to heat storage according to its volumetric heat capacity (i.e. the product of density and specific heat,  $\rho \cdot c$ ) and should, if present in relevant quantity, be included in the thermal balance. In HELIOS this can be accomplished by considering furniture as an internal wall. Internal walls are structures that separate building sectors that have the same temperature (1-zone model), while still contributing to heat storage.



As furniture were considered all wooden objects, including the door-screen/choir. Other types of furniture such as curtains or carpets were either not present at all or their mass was negligible. The total surface of all the wooden objects was accurately quantified by measurements in situ. According to own investigations, the pews and the door-screen/choir are made of larch wood<sup>3</sup> varnished with shellac<sup>4</sup> and together they represent 80% of the total surface area of the wooden furniture. The wooden furniture was entered into HELIOS as a hypothetical wall made of larch wood, having a surface of 124 m<sup>2</sup> and a width of 4 cm (a rough estimate of the average thickness of most wooden parts). The thermophysical properties of larch wood were taken from the literature and are summarized in Table 2-6.

**Table 2-6.** Thermophysical properties of the wooden furniture, as input into HELIOS.

	estimated avg. thickness (m)	thermal conductivity* (W m <sup>-1</sup> K <sup>-1</sup> )	density* (kg m <sup>-3</sup> )	specific heat** (W h kg <sup>-1</sup> K <sup>-1</sup> )
larch wood	0.040	0.120	580	0.60
* After Sell (1997)				
** Mean value for wood (Standard SIA 381/1, 1980)				

#### 2.2.2.1.6 Windows

All windows present in the building have wooden frames without seals and 2-mm-thick single-glazing. The optical properties of the glazing as used for the simulations are summarized in Table 2-7.

**Table 2-7.** Optical properties of the glazing, as input into HELIOS.

transmissivity (-)*	reflectivity (-)*		emissivity (-)**	
	outside	inside	outside	inside
0.881	0.080	0.080	0.837	0.837
* (Optics5, Lawrence Berkeley National Laboratory)				
** (HELIOS glass database)				

#### 2.2.2.1.7 Air change rate

The experimental determination of the air change rate in a building is a fairly lengthy and expensive undertaking and, thus, not always affordable. Commonly used methods involve the use of tracer gases or a blower door (see e.g. Charlesworth, 1988, for an introduction to the different techniques).

<sup>3</sup> The identity of wood (2 samples) was confirmed analytically by the Institute of Wood Science of the ETHZ.

<sup>4</sup> The composition of the varnish was analysed by EMPA, Chemistry Department (Dr. Axel Ritter), by means of FTIR (Biorad FTS-175 FT-IR Spectrometer).

In this work, an estimate of the air change rate was calculated on the basis of building observations. The church in question has plastered walls and ceiling. Both windows and doors have wooden frames and no seals. Consequently, the windows and the main entrance door represent the principal cause of passive air leakage, while the rest of the building can be considered as comparatively airtight.

The air change rate  $n$  ( $\text{h}^{-1}$ ) resulting from leakage through window and door joints was calculated with the following equations (Zürcher and Frank, 1998, p. 78)

$$\dot{V} = a_F l \Delta p^{2/3} \quad (2-9)$$

$$n = \frac{\dot{V}}{V} \quad (2-10)$$

where  $\dot{V}$  is the air flow rate ( $\text{m}^3 \text{h}^{-1}$ ),  $a_F$  is the joint permeability coefficient ( $\text{m}^3 \text{h}^{-1} \text{m}^{-1} \text{Pa}^{-2/3}$ ),  $l$  is the total joint length (m),  $\Delta p$  is the pressure difference across the openings (Pa) and  $V$  is the indoor air volume ( $\text{m}^3$ ). The following values apply to the given situation:

$$\begin{aligned} a_F &= 0.6 \text{ m}^3 \text{h}^{-1} \text{m}^{-1} \text{Pa}^{-2/3} \quad (\text{Zürcher and Frank, 1998, p. 79: window or door with wooden frame and no seals}) \\ l &= 84 \text{ m} \quad (\text{total length of windows and door perimeters}) \\ \Delta p &= 3 \text{ Pa} \quad (\text{Keller, 2004, building of type 3/4, height 0-10 m, wind class I})^5 \\ V &= 1200 \text{ m}^3 \end{aligned}$$

The resulting air change rate  $n$  corresponds to about  $0.1 \text{ h}^{-1}$ . This estimation lies in the range of the values measured by others with the tracer gas method in churches with plastered walls and vaults. Schellen (2002) performed measurements in twelve churches in the Netherlands and obtained values between 0.08 and 0.12 for churches with airtight vaults (e.g. plastered stone), whereas churches with vaults consisting of wooden boards yield values between 0.5 and 0.75. Baumann (1993) reports values between 0.02 and 0.12 for the church of Ebnat (canton St. Gallen, Switzerland).

For the HELIOS simulation, a constant air change rate of  $0.1 \text{ h}^{-1}$  was used. This value does not take into account the air change induced by building usage but, given the fact that the church is open only during the services one to two times a week, the resulting impact on the whole thermal budget can be considered negligible.

---

<sup>5</sup> The mean wind speed in Gnosca calculated from METEONORM data (METEOTEST, 2003) is  $1.5 \text{ m s}^{-1}$  with a standard deviation of  $1.5 \text{ m s}^{-1}$ . This corresponds to wind class I (speed around  $2 \text{ m s}^{-1}$ ). METEONORM is a comprehensive meteorological database, which can provide interpolated data for any desired location in the world.

#### 2.2.2.1.8 *Indoor heat sources*

The HELIOS program in its original form allows the specification of a daily heating schedule on an hourly basis. This schedule is then used for all the days of the week and can optionally be deactivated for Saturdays and Sundays. This approach is inappropriate for intermittently heated buildings, as for example churches that are heated only during the services. To circumvent this limitation, EMPA provided a modified HELIOS, which allows to freely define the heat amounts for every single hour of the calculation period<sup>6</sup>. These heat amounts were input through the file containing the meteorological data, replacing the unused rightmost column “direct normal radiation”. The heating scheduling support built into HELIOS was bypassed by setting the proper flag (PFLG=2) in the program. The sum of the indoor heat sources is given by

$$q_{indoor} = q_h + q_d + q_p \quad (2-11)$$

where  $q_h$  is the heat produced by the heating system,  $q_d$  is the heat produced by other devices (e.g. lighting system) and  $q_p$  is the heat produced by people present in the building. The church San Pietro Martire has an electrical heating system with radiators in the pews and in the chancel. During the cold season, it is switched on manually ca. two hours before the beginning of the worships and switched off immediately afterwards. The heat gains during the services are thus:

$q_h$	= 15.2 kW	38 electrical radiators of 400 W power each (36 in the pews, below the seats, and 2 in the chancel, above the lateral seats)
$q_d$	= 0.308 kW	2 light bulbs in the nave (100 W each) and 3 neon lamps in the chancel (36 W each)
$q_p$	= 0.8 - 6.6 kW	calculated from the mean number of people attending the services (Appendix C) and a heat production of 100 W per person (Zürcher and Frank, 1998)

#### 2.2.2.1.9 *Meteorological data*

HELIOS needs hourly meteorological data. The required parameters, summarized in Table 2-8, are measured or calculated by the meteorological ANETZ stations (automatic monitoring network) of the Swiss national weather service. Datasets in a format directly readable by HELIOS are available from EMPA.

---

<sup>6</sup> This feature will be included in an upcoming HELIOS version for the Microsoft Windows<sup>®</sup> operating system.

**Table 2-8.** Meteorological parameters required by HELIOS.

Parameter	Unit
global radiation on the horizontal	$\text{W m}^{-2}$
global radiation on the vertical, east component	$\text{W m}^{-2}$
global radiation on the vertical, south component	$\text{W m}^{-2}$
global radiation on the vertical, west component	$\text{W m}^{-2}$
global radiation on the vertical, north component	$\text{W m}^{-2}$
diffuse radiation on the horizontal	$\text{W m}^{-2}$
infrared radiation on the horizontal	$\text{W m}^{-2}$
infrared radiation on the vertical	$\text{W m}^{-2}$
temperature	$^{\circ}\text{C}$
relative humidity	%
wind speed	$\text{m s}^{-1}$
emissivity of the sky	-
emissivity of the surroundings	-
wind frequency from the south	%
wind frequency from the west	%
wind frequency from the north	%
wind frequency from the east	%

In order to check the suitability of data from the available meteorological stations, outdoor temperature and relative humidity were monitored in proximity of the study object. Among the possible regional stations<sup>7</sup>, Locarno-Monti (coordinates 704160/114350 of the Swiss reference system CH 1903) provides the temperature and relative humidity data that best match the values recorded outside of the church (for a comparison, see Fig. 2-7). The station lies at a similar altitude (366 m above sea level vs. ca. 300 m at the study object's site), about 20 km W-SW from Gnosca.

#### **2.2.2.1.10      *Calculation period***

The maximal length of a simulation period allowed by HELIOS is of 9999 hours. For every simulation a possibly realistic initial temperature  $T_{\text{init}}$  must be set. At the beginning of every simulation, the program makes a steady-state heat balance calculation of the first hour. The start time of every simulation was set to at least one month before the period of interest to make sure that the program had enough time to stabilize.

---

<sup>7</sup> The closest meteorological station is in Magadino (coordinates 711160/113540, altitude 197 m above sea level). However, because of its location near a swamp area at the shore of the Lago Maggiore, the recorded data, especially relative humidity, has a very different pattern than in Gnosca. Other meteorological stations were not considered either because they are much far away from the study object's site or because they are located at a much higher altitude.

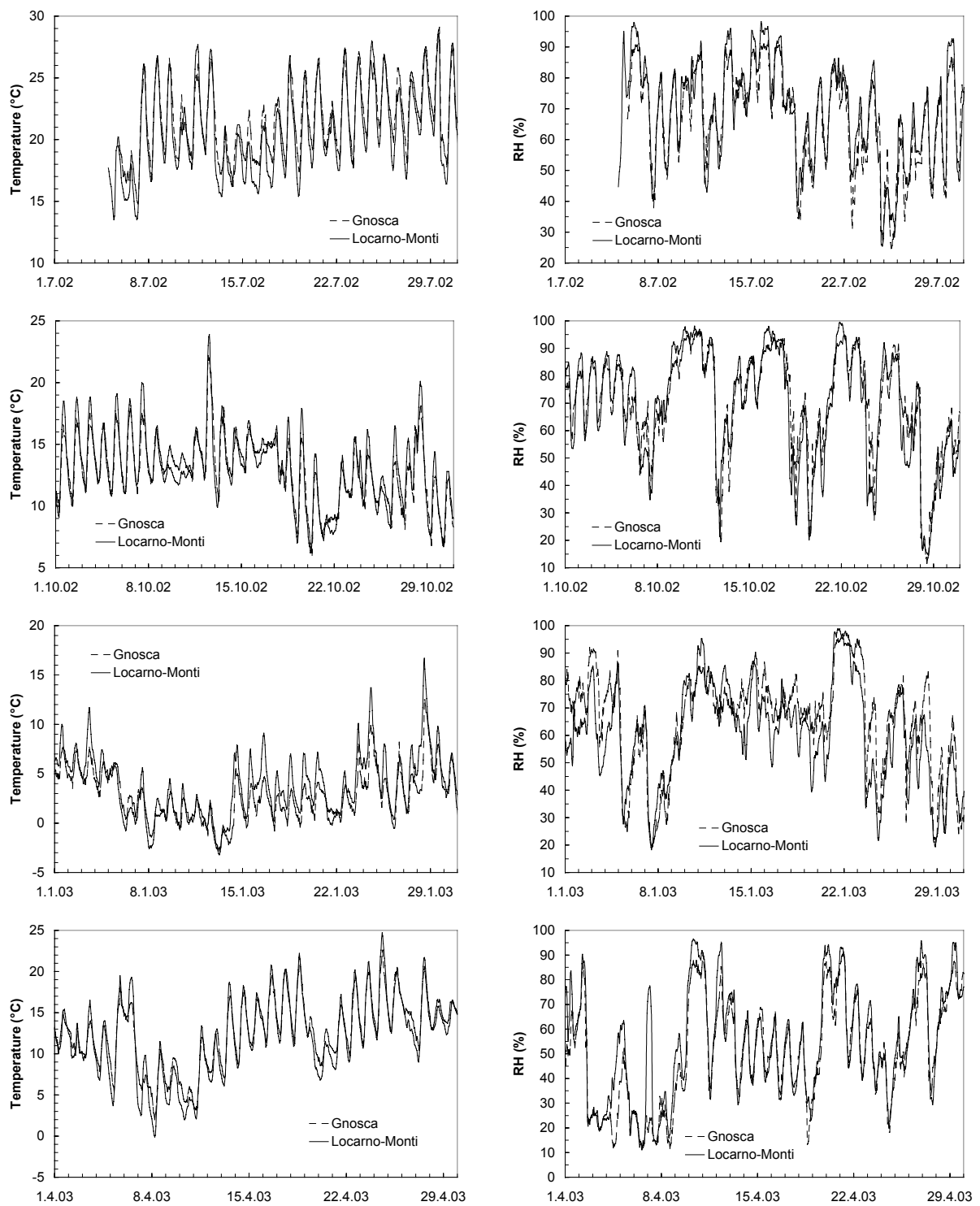


**Fig. 2-7.** Comparison of temperature and RH in Gnosca and in Locarno-Monti during the months July, October, January and April.

### 2.2.2.2 1D thermal model

The free-floating indoor temperature of unheated buildings is mostly determined by outdoor temperature, radiative processes on the building envelope and ventilation. In this section, a simple thermal model developed in the course of this study is presented. The model calculates the indoor temperature of a room by taking into account outdoor temperature, solar (UV to near-IR) and long-wave (IR) radiation on the external surfaces, as well as ventilation inside the room (Fig. 2-8). Transient heat transfer through a multi-layered envelope is computed in one dimension. A well stirred indoor air with uniform temperature is assumed. Because of its 1-dimensional nature, the model also provides information about the temperature distribution across wall sections.

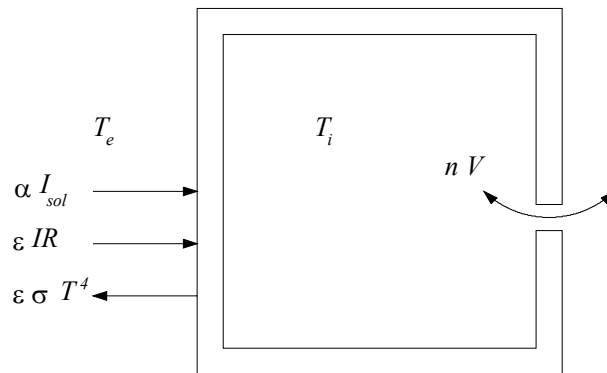


**Fig. 2-8.** Schematic representation of the model. The external surfaces are exposed to convection with air at temperature  $T_e$ , solar radiation  $\alpha I_{sol}$ , as well as long-wave radiation exchange with the sky and the surroundings  $\epsilon IR - \epsilon \sigma T^4$ . The air in the room has temperature  $T_i$  and is ventilated with the air flow rate  $nV$ .

The purpose of the model is to test to what extent and with which accuracy it is possible to estimate the indoor temperature of unheated buildings having a simple geometry, by relying on a minimal amount of easily available meteorological data, i.e. outdoor temperature and radiation. Outdoor temperature is available for many localities from conventional measuring stations (e.g. three measurements per day). The radiation data required is global solar radiation on the horizontal and on the vertical (east, south, west and north components) plus infrared radiation on the horizontal and on the vertical. This data can be readily exported from the METEONORM database (METEOTEST, 2003) for any Swiss location. The model calculates a mean value for both solar and infrared radiation. The heat transfer is computed for a single wall subjected to this mean radiation. In other words, the model assumes that all the walls and the roof are exposed to the same radiation, have equal surface area, thickness and structure, thus providing all the same thermal performance. Solar heat gains through

window glazing and heat transfer to the ground are not considered. Consequently, on the basis of these limitations the model is best applicable to unheated buildings that approach cubic proportions and have small windows.

1-dimensional heat transfer through the building envelope is governed by the parabolic partial differential equation

$$\frac{\partial T}{\partial t} = \frac{\lambda}{\rho c} \frac{\partial^2 T}{\partial x^2} \quad (2-12)$$

where  $T$  is the temperature ( $^{\circ}\text{C}$ ),  $t$  is the time (s),  $\lambda$  is the thermal conductivity ( $\text{W m}^{-1} \text{K}^{-1}$ ),  $\rho$  is the density ( $\text{kg m}^{-3}$ ),  $c$  is the specific heat ( $\text{J kg}^{-1} \text{K}^{-1}$ ) and  $x$  is the distance (m). The present model solves equation (2-12) numerically, with an explicit forward-time centered-space (FTCS) finite difference scheme, as shown in Hagentoft (2001). Since the explicit technique is not unconditionally stable, a stable time step is computed at the beginning of every simulation run to ensure algorithm stability. The solving strategy can be summarized as follows. The wall is divided into a number of nodes (Fig. 2-9); the algorithm iterates over every node and calculates heat in- and outflow using steady-state equations. The heat flux between two adjacent nodes is

$$q_{12} = \frac{T_1 - T_2}{R_{12}} \quad (\text{W m}^{-2}) \quad (2-13)$$

with

$$R_{12} = \frac{d}{\lambda_{12}} \quad (\text{m}^2 \text{K W}^{-1}) \quad (2-14)$$

where  $T_1$  is the temperature of the first node (K),  $T_2$  is the temperature of the second node (K),  $R_{12}$  is the thermal resistance of the material between the two nodes ( $\text{m}^2 \text{K W}^{-1}$ ),  $d$  is the distance (m) and  $\lambda_{12}$  is the thermal conductivity ( $\text{W m}^{-1} \text{K}^{-1}$ ). The net heat flux in every node gives rise to a temperature increase or decrease. For a time interval  $\Delta t$  (s), the temperature variation is given by

$$\Delta T = \Delta t \frac{q}{\rho c d} \quad (\text{K}) \quad (2-15)$$

where  $q$  is the net heat flux to the node ( $\text{W m}^{-2}$ ),  $\rho$  is the density ( $\text{kg m}^{-3}$ ) of the material between two nodes,  $c$  is the specific heat ( $\text{J kg}^{-1} \text{K}^{-1}$ ) and  $d$  is the distance (m).

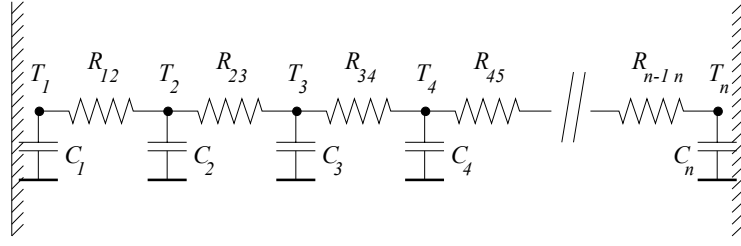


**Fig. 2-9.** Network representation of 1-dimensional heat transfer in the wall.  $T_1..T_n$  are the temperatures of the nodes,  $C_1..C_n$  is the heat capacity of the material at the nodes and  $R_{12}..R_{n-1 n}$  is the thermal resistance of the material between the nodes.

The total heat flux on the external surfaces of the building is determined by air temperature, solar radiation and long wave radiation exchange with sky and surrounding environment

$$q_e = q_{air} + q_{sol} + q_{lw} \quad (\text{W m}^{-2}) \quad (2-16)$$

The heat flux from the air to the surface is

$$q_{air} = \frac{T_e - T_{se}}{R_{se}} \quad (\text{W m}^{-2}) \quad (2-17)$$

where  $T_e$  is the temperature of the air (K),  $T_{se}$  is the temperature of the external surface (K) and  $R_{se}$  is the surface resistance ( $\text{m}^2 \text{ K W}^{-1}$ ). The heat flux from solar radiation is

$$q_{sol} = \alpha I_{sol} \quad (\text{W m}^{-2}) \quad (2-18)$$

where  $\alpha$  is the absorptivity of the external surface (–) and  $I_{sol}$  is the solar radiation ( $\text{W m}^{-2}$ ). The long-wave radiation exchange of the surface with sky and surroundings is given by

$$q_{lw} = q_{sky} - q_{surf} = \varepsilon IR - \varepsilon \sigma T^4 \quad (\text{W m}^{-2}) \quad (2-19)$$

where  $q_{sky}$  is the heat flux from long-wave radiation of the sky ( $\text{W m}^{-2}$ ),  $q_{surf}$  is the radiative heat flux of the surface according to Stefan-Boltzmann law ( $\text{W m}^{-2}$ ),  $IR$  is the infrared radiation of the sky ( $\text{W m}^{-2}$ ),  $\varepsilon$  is the emissivity of the surface (–),  $\sigma$  is the Stefan-Boltzmann constant ( $5.67 \cdot 10^{-8} \text{ W m}^{-2} \text{ K}^{-4}$ ) and  $T$  is the absolute temperature of the surface (K).

The total heat flow into the room is given by the sum of heat flow from the interior wall surfaces and heat flow due to ventilation

$$\dot{Q}_i = \dot{Q}_w + \dot{Q}_v \quad (\text{W}) \quad (2-20)$$



The heat flow from the wall surfaces to the indoor air is

$$\dot{Q}_w = A \frac{(T_{si} - T_i)}{R_{si}} \quad (\text{W}) \quad (2-21)$$

where  $A$  is the total area of the interior wall surfaces ( $\text{m}^2$ ),  $R_{si}$  is the surface resistance ( $\text{m}^2 \text{ K W}^{-1}$ ),  $T_{si}$  is the surface temperature (K) and  $T_i$  is the temperature of the indoor air (K). The ventilation heat flow to the room is

$$\dot{Q}_v = n V \rho c (T_e - T_i) \quad (\text{W}) \quad (2-22)$$

where  $n$  is the air change rate ( $\text{h}^{-1}$ ),  $V$  is the indoor air volume ( $\text{m}^3$ ),  $\rho$  is the density of the air ( $\text{kg m}^{-3}$ ),  $c$  is the specific heat ( $\text{W h kg}^{-1} \text{ K}^{-1}$ ),  $T_e$  is the outdoor temperature (K) and  $T_i$  is the indoor air temperature (K). The rate of temperature variation of the indoor air becomes then

$$\dot{T} = \frac{A}{V \rho c} \frac{(T_{si} - T_i)}{R_{si}} + n (T_e - T_i) \quad (\text{K h}^{-1}) \quad (2-23)$$

## 2.2.3 Hygric simulation

### 2.2.3.1 Model

A detailed description of the theory behind the used hygric model (Simmler et al., 1995; 1996) can be found in Appendix E. The model makes the following assumptions:

- coupling between heat and moisture transport is neglected (that is, processes involving transfer of latent heat; e.g. evaporation of water from a surface doesn't cause cooling of the surface)
- temperature and humidity of the indoor air have a homogeneous spatial distribution
- air change rate, outdoor air moisture content, indoor moisture sources and storage are known time-dependent quantities

The interior air volume is ventilated with external air according to a specific air change rate, while moisture in the indoor air interacts cyclically with the hygroscopic materials in the room. If the humidity of the indoor air is raised abruptly, then a thin superficial *active layer* of the materials in contact with that environment is rapidly loaded with moisture. Saturation is reached according to the sorption isotherm of the material. The moisture content of the active layer is considered constant, while the rest of the material is neglected. The thickness of the active layer, as determined experimentally (Simmler et al., 1995; 1996) for short term exposure (6-12 hours) corresponds to 1.5 mm for timber, 3 mm for sandstone, 7.7 mm for cellular concrete and 8.9 mm for gypsum. The interaction between indoor air and hygroscopic materials can be described in terms of a two-node system having one node in the air and the other in the active layer of the material (Fig. 2-10).

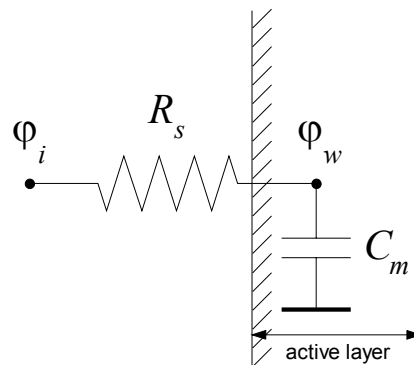


**Fig. 2-10.** Network representation of the two-node hygric model. The nodes in the air and in the material have relative humidity  $\varphi_i$  and  $\varphi_w$ , respectively.  $R_s$  is the surface resistance and  $C_m$  the moisture storage capacitance of the material.

The parameters necessary to describe the hygric behaviour of a given material in such a system could in principle be derived from the diffusion coefficient, the sorption isotherm and an average time constant. However, in practice these parameters are not available for the broad range of composite, inhomogeneous and non-standardized buildings materials that are usually found in historical edifices. Therefore, the hygric response of the principal materials present in the church has been determined experimentally at EMPA by way of isothermal dynamic water vapour sorption tests. The materials investigated were:

- cement plaster samples (area ca. 50 cm<sup>2</sup>, height ca. 2 cm) from the internal wall surfaces, coated with emulsion paint
- floor tile made of cement mortar (area ca. 190 cm<sup>2</sup>, height ca. 2 cm)
- larch wood specimens (area 625 cm<sup>2</sup>, height 2 cm)<sup>8</sup>, natural and varnished with 2 and 4 coats of shellac, respectively. The shellac varnish was prepared according to Elberskirch (1937)<sup>9</sup>

The sorption tests measured the quantity of water absorbed by the material following an abrupt increase of the relative humidity of the air. For that purpose, each sample was placed on a metal plate with the surface through which water vapour exchange with the environment was to be allowed facing upwards (i.e. the painted surface of plaster and wood samples and the upper surface of the floor tile). The sides were sealed with silicone and each unit was put on a precision weighing machine inside a climate chamber. The RH of the environment inside the climate chamber was maintained at a constant low value (37/45%) until the weight of the sample stabilized. Then the RH was raised to a higher value (70/80%), maintained at that level for several days (10/59) and dropped to the starting low value. The temperature was kept constant (20/23 °C) for the whole duration of the experiment. The weight of each sample was recorded at regular intervals (30/60 min) by a digital data acquisition system.

According to the present model, the increase in water content of the test material follows an exponentially damped saturation process (see equation (6-46) Appendix E and its analytical solution)

$$m(t) - m(0) = \Delta m (1 - e^{-t/\tau}) \quad (2-24)$$

with

---

<sup>8</sup> The determination of the hygric response of larch wood was carried out on specimens prepared in the laboratory because, understandably, it was not possible to take samples of an usable size from the pews.

<sup>9</sup> 50 g of dry shellac flakes were dissolved in 200 ml ethanol by gently heating at 50°C. When most shellac was dissolved, the heating was turned off, the mixture was allowed to cool down to room temperature and was finally filtered with a paper filter. The obtained shellac varnish was applied on the wood boards with a cloth.

$$1/\tau = \frac{b p_s}{d s} \quad \text{and} \quad (2-25)$$

$$\Delta m = A d s \Delta \varphi \quad (2-26)$$

where  $m(0)$  is the initial mass of the sample (g),  $m(t)$  is the mass of the sample (g) at time  $t$ ,  $\Delta m$  is the variation of the mass of the sample (g),  $\tau$  is the time constant (h),  $p_s$  is the saturation water vapour pressure (Pa),  $b$  is the moisture transfer coefficient ( $\text{g h}^{-1} \text{m}^{-2} \text{hPa}^{-1}$ ),  $d$  is the thickness of the active material layer (m),  $s$  is the slope of the sorption isotherm ( $\text{g m}^{-3}$ ) and  $A$  is the area of the unsealed sample surface ( $\text{m}^2$ ).

The thickness of the active layer and the slope of the sorption isotherm over the experimental RH range are taken as constant. This last assumption is acceptable for the materials in question (Fig. 2-11).  $\Delta m$  and  $\tau$  were obtained by fitting equation (2-24) to the experimental results using a least squares method. The value of  $b$  and the product  $d \cdot s$  required by the model were calculated using (2-25) and (2-26).

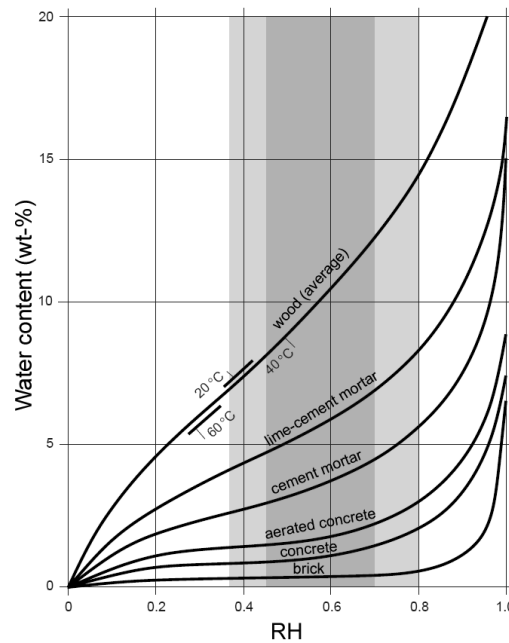


**Fig. 2-11.** Typical water vapour sorption isotherms for different building materials and RH range for the dynamic water vapour sorption tests. The shaded dark area shows the range 45-70% for the sorption tests of plasters and floor tile (both made of cementitious material), the light area the range 37-80% for the tests of larch wood. Within these ranges, the slope of the sorption curves of the materials in question is reasonably constant. Sorption curves after Klopfer (1974).

The input parameters required by the hygric model are summarized in Table 2-9. The simulation was performed using the indoor and surface temperatures generated by the HELIOS model.

**Table 2-9.** Parameters required by the hygric model.

Constant parameters		Unit
Indoor air volume		$\text{m}^3$
Time step for the simulation		h
For every material considered	Surface area	$\text{m}^2$
	Mean slope of the sorption isotherm	$\text{g m}^{-3}$
	Thickness of the active layer	m
	Moisture transport coefficient	$\text{g h}^{-1} \text{m}^{-2} \text{hPa}^{-1}$
Time-dependent parameters (time series)		
Indoor air temperature		$^{\circ}\text{C}$
Outdoor air temperature		$^{\circ}\text{C}$
Air change rate		$\text{h}^{-1}$
Outdoor air RH		%
Total water vapour flow rate from moisture sources		$\text{g h}^{-1}$
Total mass of materials with fast moisture uptake capacity		g
Surface temperatures of the materials considered		$^{\circ}\text{C}$

A simulation of transient heat transfer in the external walls of the church, performed with the 1-dimensional numerical model presented in section 2.2.2.2, shows that, at each time point, the temperature is essentially homogeneous from the inner wall surface till a depth of at least 20-30 cm (Fig. 2-12). Hence, the temperature of the inner surfaces is a good approximation of the temperature of the active layer.

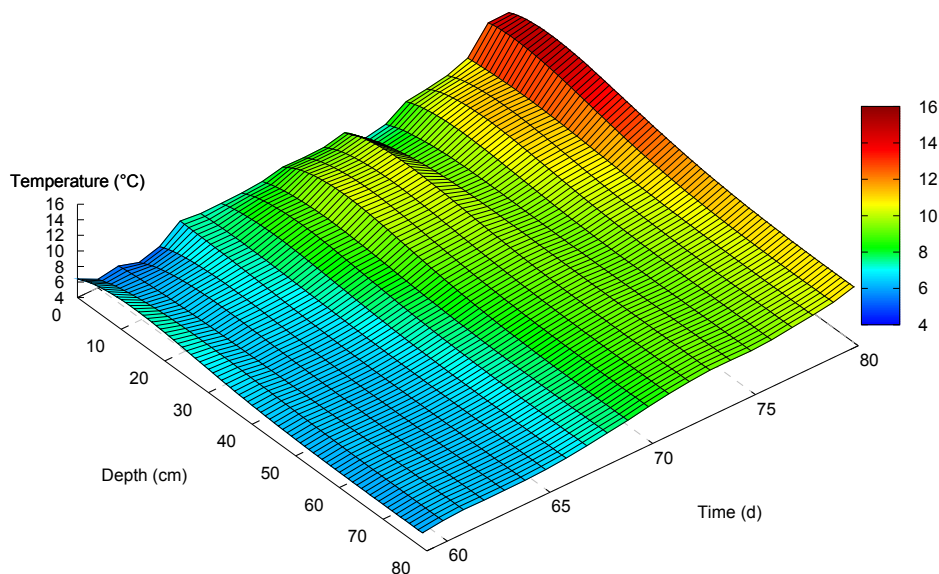


**Fig. 2-12.** Temperature of an external wall of the church San Pietro Martire as a function of time (period 1.3.-22.3.2002) and depth from the external surface, obtained with the 1D thermal model of section 2.2.2.2. The temperature of the wall is, at each time point, essentially homogeneous up to a depth of at least 20-30 cm from the inner surface.

### 2.2.3.2 Hygric properties of the materials

The hygric properties of the materials describe their ability to absorb moisture from the environment and, ultimately, to influence its humidity. The results of the dynamic water vapour sorption tests are shown in Fig. 2-13. The parameters needed by the hygric model, derived according to section 2.2.3.1, are summarized in Table 2-10.

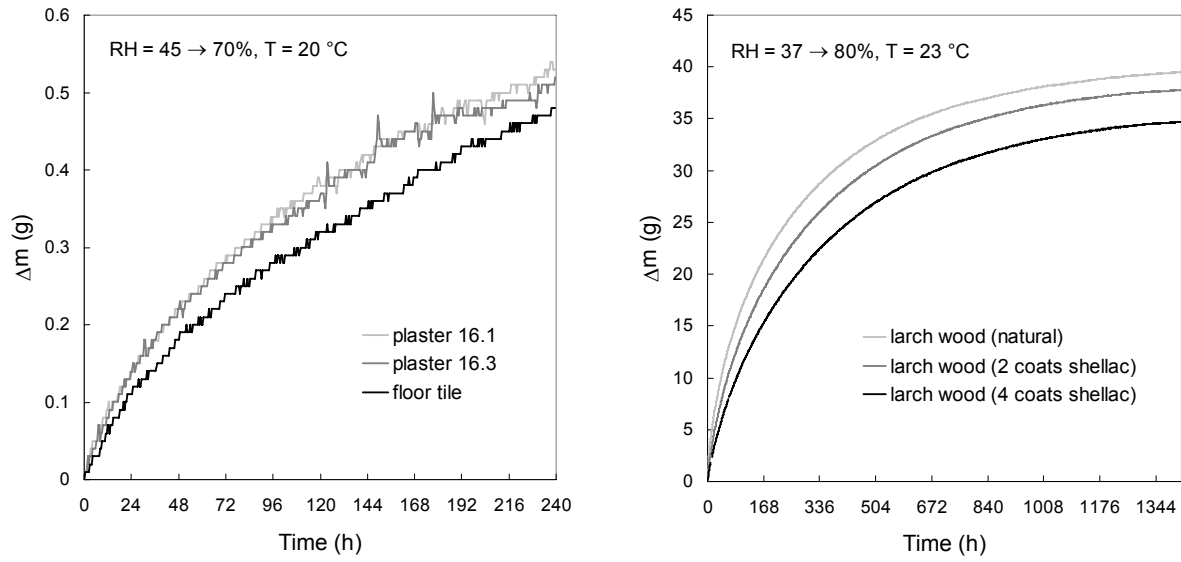


**Fig. 2-13.** Dynamic water vapour sorption test. Left: plaster samples and floor tile; the RH was varied from 45 to 70%, the temperature was kept constant at 20 °C. Right: larch wood, natural and varnished with shellac; the RH was varied from 37 to 80%, the temperature was kept constant at 23 °C.

**Table 2-10.** Dynamic water vapour sorption properties of the investigated materials.

Material		$A$ ( $\text{m}^2$ )	$\Delta m$ (g)	$\tau$ (h)	$d_s$ ( $\text{g m}^{-2}$ )	$b$ ( $\text{g h}^{-1} \text{m}^{-2} \text{hPa}^{-1}$ )
plaster	sample 16.1	0.004569	0.57	103.72	497.51	0.2053
	sample 16.3	0.005306	0.55	102.05	415.89	0.1744
larch wood	natural	0.0625	38.28	225.22	1424.07	0.2252
	varnished (2 coats shellac)	0.0625	37.05	267.50	1378.39	0.1835
	varnished (4 coats shellac)	0.0625	34.42	313.38	1280.37	0.1455
floor tile		0.018633	0.56	136.02	119.58	0.0376

### 2.2.3.3 Indoor moisture sources

The indoor air in the study object has on average a higher moisture content than the outdoor air. The mean difference over the monitoring period was of about  $1 \text{ g m}^{-3}$ . This discrepancy can be explained with the presence of an indoor moisture source, most likely caused by infiltration of ground moisture. The high moisture content of the soil below the floor, observed during archaeological excavations (Fig. 2-27, right), supports this hypothesis. The flow rate  $q$  of water vapour is given by

$$q = n V (AH_i - AH_e) \quad (\text{g h}^{-1}) \quad (2-27)$$

where  $n$  is the air change rate ( $\text{h}^{-1}$ ),  $V$  is the indoor air volume ( $\text{m}^3$ ),  $AH_i$  is the absolute humidity of the indoor air ( $\text{g m}^{-3}$ ) and  $AH_e$  is the absolute humidity of the exterior air ( $\text{g m}^{-3}$ ). The flow rate (Fig. 2-14) was calculated in hourly steps over a period of one year (1.4.2002-31.3.2003) using indoor and outdoor climate data, an air change rate of  $0.1 \text{ h}^{-1}$  and an indoor air volume of  $1200 \text{ m}^3$  (section 2.2.2.1.7). The values obtained were normally distributed; the mean of  $120 \text{ g h}^{-1}$  (standard deviation  $150 \text{ g h}^{-1}$ ) was used for the simulation. This value corresponds to a humidity load of  $1 \text{ g m}^{-3}$  and can be regarded as low (Sagelsdorff and Frank, 1990, page 88).

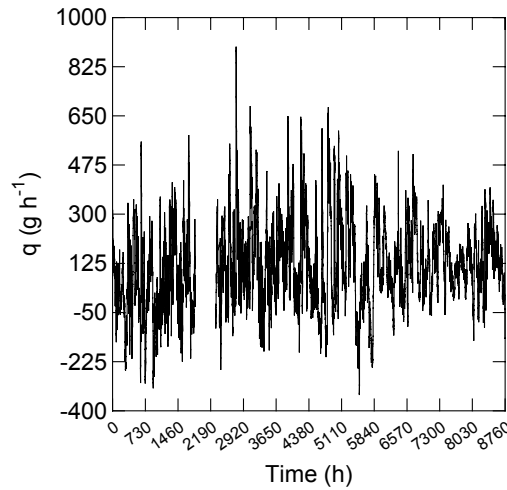


**Fig. 2-14.** Water vapour flow rate over the period 1.4.2002-31.3.2003, calculated using (2-27).

#### **2.2.3.4 Intermittent moisture sources and storage**

During the utilization of the church there is an additional moisture input, which is caused by the transpiration of the persons present in the building. At the same time, churchgoers also contribute to moisture storage by bringing into the room hygroscopic materials with fast moisture uptake capacity (i.e. clothes).

The dimension of these parameters was derived from information concerning building usage and attendance at the services (Appendix C). Assuming an average water vapour production of  $40 \text{ g h}^{-1}$  per person (Zürcher and Frank, 1998), the contribution to the total moisture flow rate during the services was in the range  $320\text{-}2640 \text{ g h}^{-1}$ , depending on the attendance. The moisture storage capacity, given an average mass of textiles of  $2000 \text{ g}$  per person and a mean slope of the sorption isotherm of  $0.15$  (which is representative for materials like cotton) was estimated to be in the range  $2400\text{-}19800 \text{ g}$ .

#### **2.2.3.5 Simulation steering**

HELIOS and the hygric model are implemented as separate computer programs that, in their current versions, cannot directly communicate to each other. Since the hygric model needs as part of its input the temperatures of the air and of the surfaces calculated by HELIOS, the manual preparation of input files can be a very time-consuming task, especially if simulation parameters are to be changed frequently.

In order to obviate to this situation, a software has been developed in the course of the present work. The software allows to interactively change model parameters and, thus, facilitates the simulation of different scenarios. Simulations are steered by issuing predefined commands from a command-line interface. Input files for the hygric model are generated automatically on the basis of the parameters specified and the temperatures previously calculated by HELIOS. The output of the simulations is written to a file and, optionally, displayed graphically by means of the gnuplot (Williams and Kelley, 2004) plotting engine. The software was developed in ANSI Common Lisp using CLISP 2.33.1 (Haible and Steingold, 2004).



## 2.3 Results

### 2.3.1 Thermal simulation

#### 2.3.1.1 HELIOS thermal model

The temperature of the indoor air simulated by HELIOS was compared with in situ measurements for the period from the beginning of climate monitoring in the church until the beginning of the renovation works (April 2002 to January 2003). The results are presented in Fig. 2-15.

The overall trend of the computed air temperature and the amplitude of the daily fluctuations is in good agreement with the recorded values. There is no observable significant seasonal discrepancy. Heating events are not always accurately reproduced. This is due to the fact that 1) the heating schedule of the manually-operated heating system might slightly vary from time to time and 2) in case of missing service attendance data, a mean value has been used.

A cumulative frequency distribution plot of the difference  $D_T$  between measured and computed temperature is shown in Fig. 2-17 left.  $D_T$  has a mean value of  $-0.1\text{ }^{\circ}\text{C}$  with a standard deviation of  $+0.7\text{ }^{\circ}\text{C}$ ; the median value is  $-0.1\text{ }^{\circ}\text{C}$ . Accordingly,  $D_T$  lies during approx. 68% of the time in the range from  $-0.8$  to  $+0.6\text{ }^{\circ}\text{C}$  and during approx. 95% of the time in the range from  $-1.4$  to  $+1.2\text{ }^{\circ}\text{C}$ <sup>10</sup>.

The simulation of the surface temperature of the NW wall was compared with in situ measurements for the period from the beginning of monitoring until the beginning of the renovation works (November 2002 to January 2003). The results are presented in Fig. 2-16. The overall trend of the computed surface temperature and the amplitude of the fluctuations is in good agreement with the recorded values although not as precise as in the case of the air temperature. A cumulative frequency distribution plot of  $D_T$  is shown in Fig. 2-17 right. The difference  $D_T$  between measured and computed temperature has a mean value of  $-0.4\text{ }^{\circ}\text{C}$  with a standard deviation of  $+0.6\text{ }^{\circ}\text{C}$ ; the median value is  $-0.4\text{ }^{\circ}\text{C}$ . Accordingly,  $D_T$  lies during approx. 68% of the time in the range from  $-1.0$  to  $+0.3\text{ }^{\circ}\text{C}$  and during approx. 95% of the time in the range from  $-1.6$  to  $+0.9\text{ }^{\circ}\text{C}$  (see footnote 10).

---

<sup>10</sup> As the data set roughly follows a normal distribution, approximately 68% of all its data points fall within the interval  $(\mu-\sigma, \mu+\sigma)$  and approximately 95% within the interval  $(\mu-2\sigma, \mu+2\sigma)$ , where  $\mu$  is the sample mean and  $\sigma$  the standard deviation.

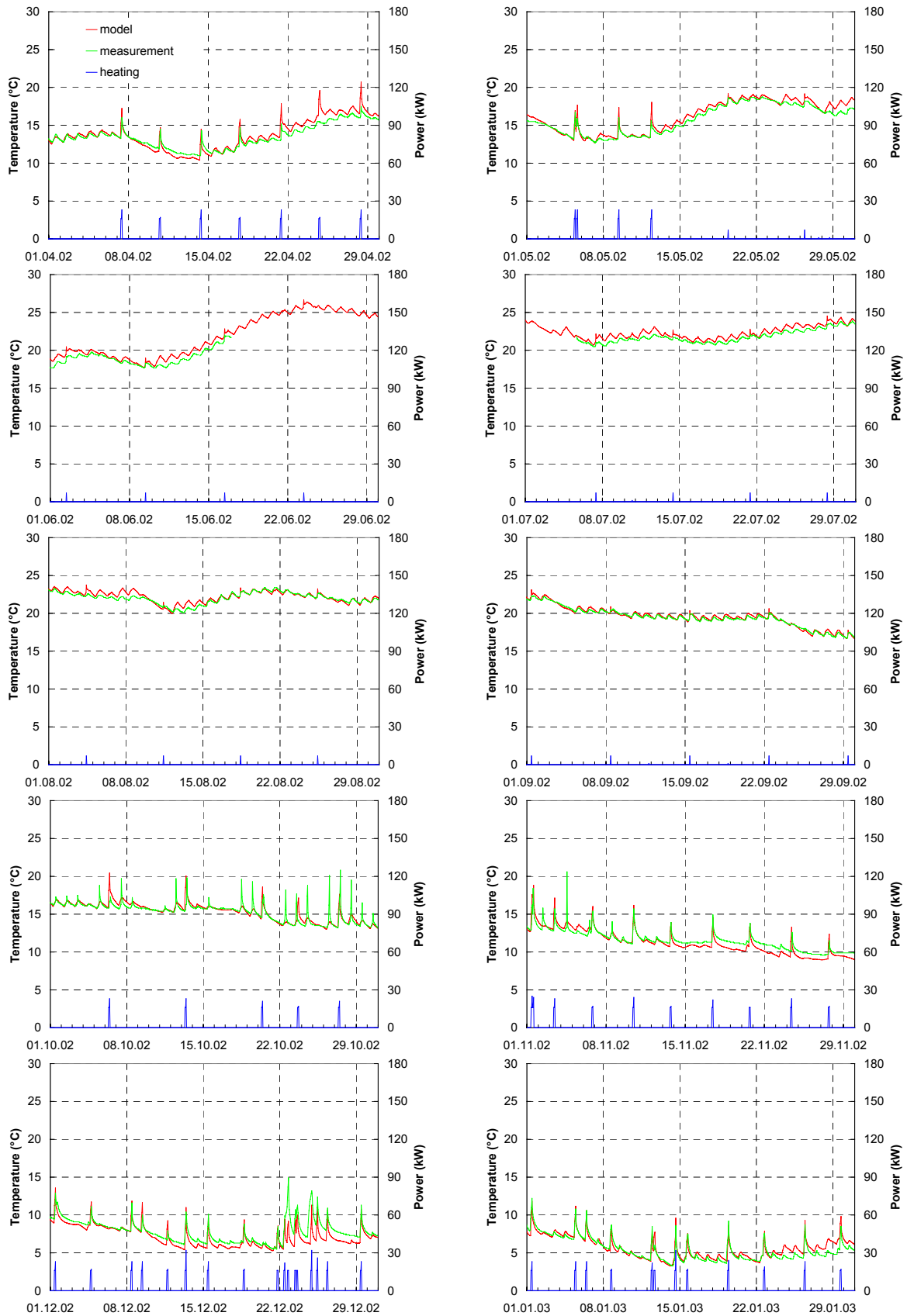


**Fig. 2-15.** Results of the thermal simulation of the indoor air for the period from April 2002 to January 2003 (hourly values). The peaks of the measured temperature that are not associated with any heating and that are observable during October and the beginning of November are due to direct sunshine on the sensor of the logger. Measurements for the period from 17.6.-5.7.2002 are missing due to a failure of the measuring equipment.

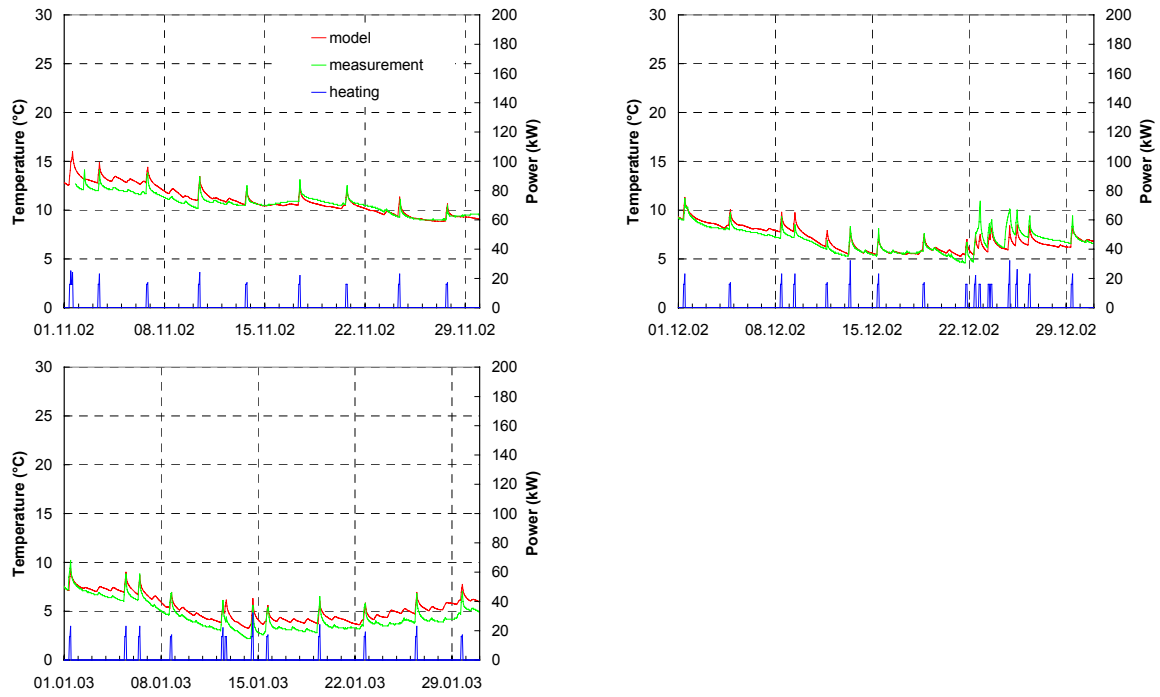


**Fig. 2-16.** Results of the simulation of the temperature of the indoor surface of the NW wall (hourly values) for the period from November 2002 to January 2003 and comparison with the measurements.

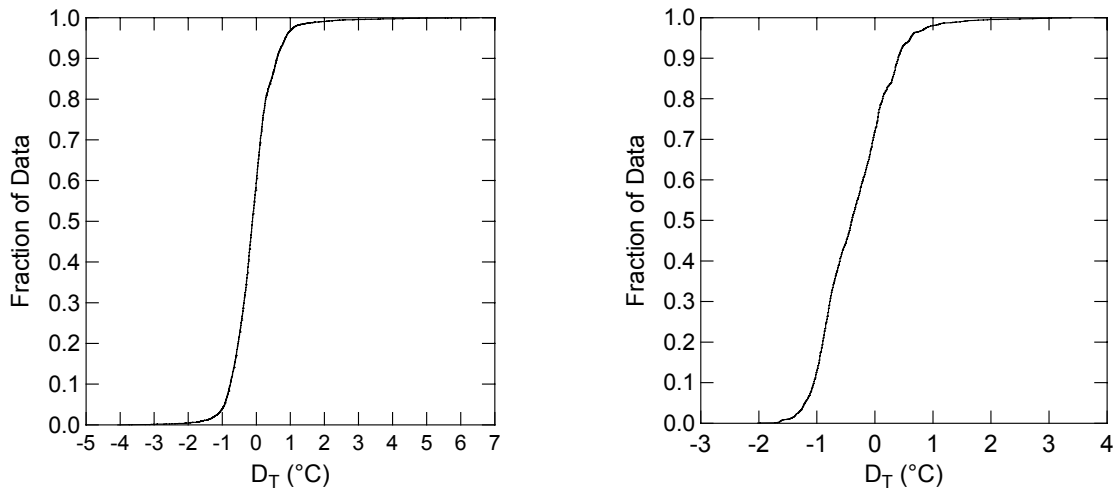


**Fig. 2-17.** Cumulative frequency distribution of the difference  $D_T$  between measurement and model calculations. Left: temperature of the indoor air for the period from April 2002 to January 2003. Right: temperature of the indoor surface of the NW wall for the period from November 2002 to January 2003.

### 2.3.1.2 1D thermal model

Computations with the 1-dimensional thermal model (section 2.2.2.2) were performed for the Holy Cross chapel of St. John's Convent in Müstair (Fig. 2-18) and for the church San Pietro Martire in Gnosca.

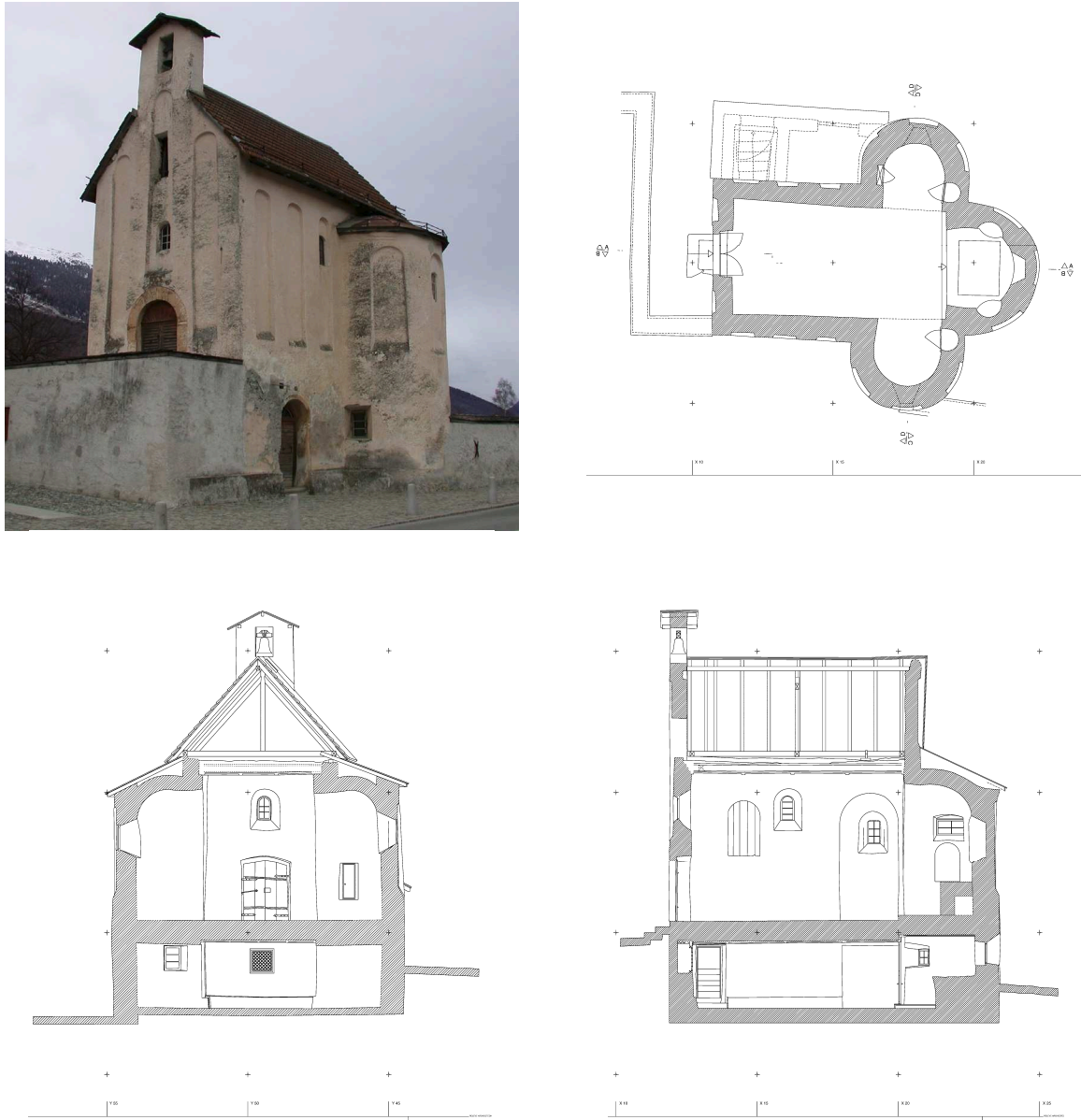


**Fig. 2-18.** The Holy Cross chapel of St. John's Convent in Müstair. The simulation was performed for the upper storey of the chapel where the climate is monitored because of damage on wall paintings. Line drawings are from Archéotech SA; tick marks on the scales are in intervals of 5 m.

The Holy Cross chapel has a simple structure with walls in direct contact with the external environment, no lateral thermal buffer zones and very small windows. The simulation was performed for the upper storey of the chapel, which has a suspended floor and thus is not in

direct contact with the ground. Thanks to these features, the building is an ideal study object for testing the 1D model, which does not consider heat transfer through windows and ground. The parameters used for the simulation of the indoor climate of the Holy Cross chapel were:

- Wall: total thickness 80 cm, plastered on both sides, estimated plaster thickness ca. 4 cm; thermal conductivity, density and specific heat from SIA according to Table 2-2.
- Internal ( $R_{si}$ ) and external ( $R_{se}$ ) horizontal surface resistances according to Table 2-1.
- Absorptivity and emissivity of the external surface estimated at 0.50 and 0.97, respectively.
- Outdoor temperature from the conventional KLIMA meteorological station of S. Maria (Swiss national weather service), 3 measurements per day.
- Radiation data for the locality Münstair from METEONORM, hourly values.
- Air change rate estimated at about  $1 \text{ h}^{-1}$ .
- Total area of the internal surfaces ca.  $200 \text{ m}^2$ , indoor air volume ca.  $230 \text{ m}^3$ .

The results of the simulation were compared with in situ recordings of the indoor temperature in order to check the accuracy of the model. The discrepancy between measured temperature and model prediction, over a period of three years (2001-2002), ranges from  $-1.0$  to  $1.5 \text{ °C}$  for 95% of the computed values. The overall trend of the modelled temperature and the amplitude of the daily fluctuations are in good agreement with the measurements, as shown in Fig. 2-19 for year 2002.

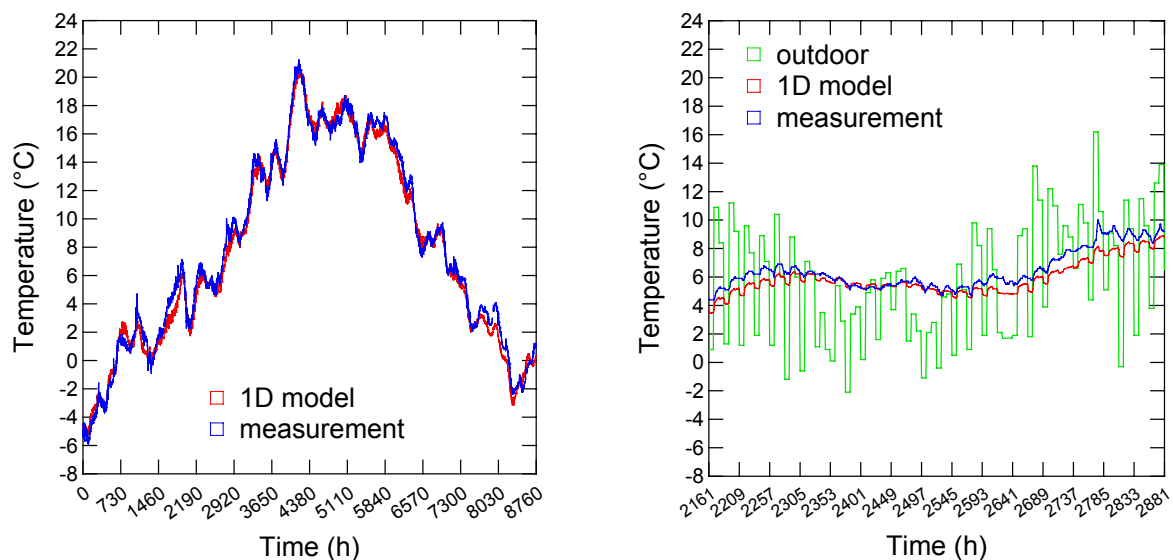


**Fig. 2-19.** Holy Cross chapel in Münstair (upper storey), comparison of simulation (1D model) and measurement. The simulation was run with temperature data from the nearby manually operated KLIMA station in S. Maria (3 measurements per day) and METEONORM radiation data. Left: simulation for year 2002. Right: detailed view of April 2002 with superimposed outdoor temperature.

The church San Pietro Martire is a more complex building than the Holy Cross chapel: it has two lateral buffer zones (tower and sacristy), bigger windows and an uninsulated floor in direct contact with the ground. Due to these characteristics, the church differs significantly from the simple specifications of the 1D model. It is thus an interesting study object for testing the domain of applicability of the model.

The parameters used for the simulation of the indoor climate of the church San Pietro Martire were:

- Wall: total thickness 90 cm, plastered on both sides, estimated plaster thickness ca. 4 cm; thermal conductivity, density and specific heat from SIA according to Table 2-2.
- Internal ( $R_{si}$ ) and external ( $R_{se}$ ) horizontal surface resistances according to Table 2-1.
- Absorptivity and emissivity of the external surfaces of 0.32 and 0.97, respectively.
- Outdoor temperature and radiation data from the ANETZ automatic meteorological station of Locarno Monti (Swiss national weather service), hourly values.
- Air change rate  $0.1 \text{ h}^{-1}$ .
- Total area of the internal surfaces  $600 \text{ m}^2$ , indoor air volume  $1200 \text{ m}^3$ .

These values are the same as used in the HELIOS reference model (section 2.2.2.1).

The results of the simulation with the 1D model for the church San Pietro Martire were compared with the ones of the HELIOS reference model under free-floating conditions (i.e. without indoor heat sources) and with those obtained with the same HELIOS model by setting the total surface of the windows to zero (i.e. no windows). Eliminating the surface of the windows has the effect of excluding the modelling of solar heat gains through glazing, which is also a factor that is not considered by the 1D model.

According to the results in Fig. 2-20, the temperature computed by the 1D model shows the same overall trend as the one obtained with HELIOS but is shifted up to about  $2.5 \text{ }^{\circ}\text{C}$  towards lower values. On the other hand, there is a much better agreement (difference of about  $\pm 1 \text{ }^{\circ}\text{C}$ ) with the temperature calculated by HELIOS for the building without windows. This indicates that the discrepancies between the HELIOS reference model and the 1D model are mainly due to the fact that the 1D model does not consider solar heat gains through windows. The daily fluctuations of the temperature are not reproduced correctly by the 1D model: the amplitude is much smaller if compared with the HELIOS models and the daily fluctuations hardly observable.

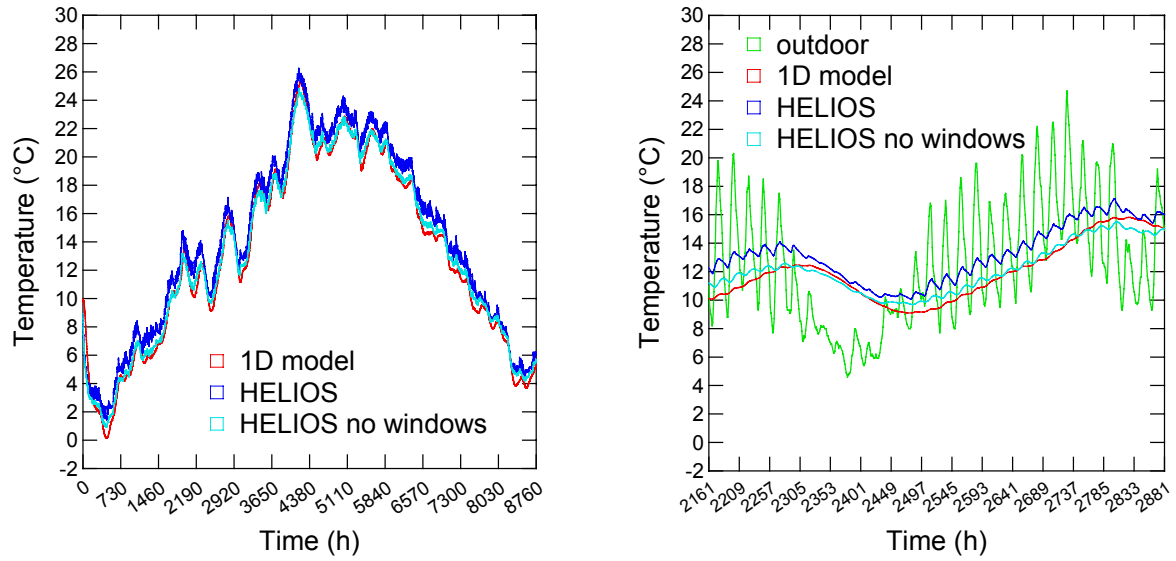


**Fig. 2-20.** Church San Pietro Martire in Gnosca, comparison of simulations with the 1D model and with HELIOS. Both models were run with the same temperature and radiation data (ANETZ station Locarno-Monti). The results of the HELIOS simulation are the same as in section 2.3.1.1. Left: simulation for year 2002. Right: detailed view of April 2002 with superimposed outdoor temperature.

### 2.3.2 Hygric simulation

The indoor air humidity simulated by the hygric model was compared with in situ measurements for the period from the beginning of climate monitoring in the church until the beginning of the renovation works (April 2002 to January 2003). The results are presented in Fig. 2-21.

The overall trend of the simulated absolute and relative humidity follows the measured values. Cumulative frequency distribution plots of the difference  $D_{AH}$  between measured and computed AH and of the difference  $D_{RH}$  between measured and computed RH are shown in Fig. 2-22.  $D_{AH}$  has a mean value of  $+0.1 \text{ g m}^{-3}$  with a standard deviation of  $+0.5 \text{ g m}^{-3}$ ; the median value is  $+0.1 \text{ g m}^{-3}$ . Accordingly,  $D_{AH}$  lies during approx. 68% of the time in the range from  $-0.4$  to  $+0.6 \text{ g m}^{-3}$  and during approx. 95% of the time in the range from  $-0.9$  to  $+1.0 \text{ g m}^{-3}$  (see footnote 10, p 36).  $D_{RH}$  has a mean value of  $+0.6\%$  with a standard deviation of  $+3.5\%$ ; the median value is  $+1.0\%$ . Accordingly,  $D_{RH}$  lies during approx. 68% of the time in the range from  $-2.9$  to  $+4.2\%$  and during approx. 95% of the time in the range from  $-6.5$  to  $+7.7\%$  (see footnote 10, p. 36).

The calculation of RH is based on the absolute humidity and the simulated air temperature (section 2.3.1.1); an error in the temperature affects the resulting RH exponentially. Fig. 2-23 shows that a variation of  $\pm 1 \text{ }^{\circ}\text{C}$  at a temperature of  $15 \text{ }^{\circ}\text{C}$  and an absolute humidity of  $10 \text{ g m}^{-3}$  causes an RH variation of nearly  $\pm 5\%$ .

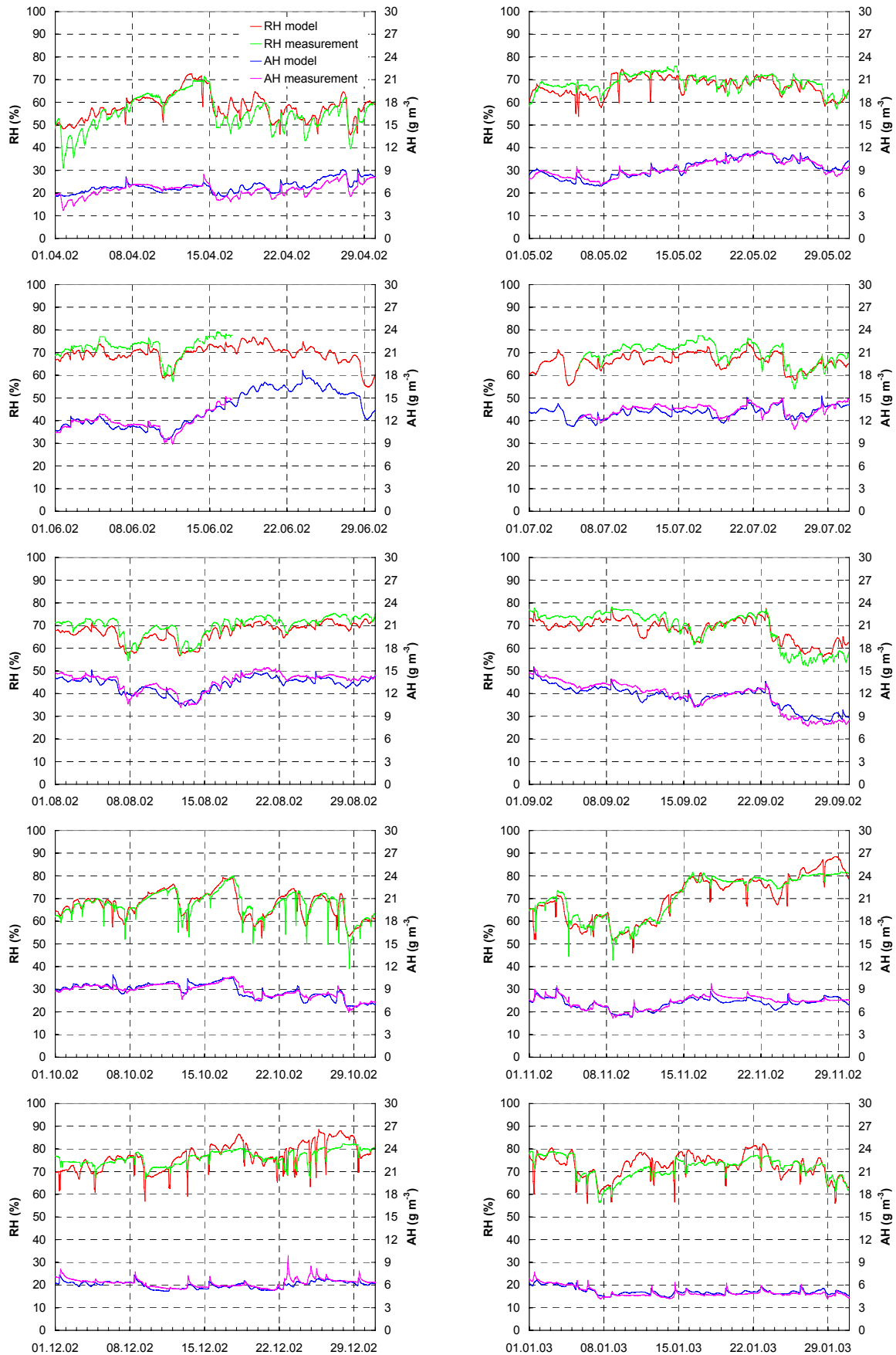


**Fig. 2-21.** Results of the hygric simulation (hourly values) for the period from April 2002 to January 2003. Measurements for the period from 17.6.-5.7.2002 are missing due to a failure of the measuring equipment.



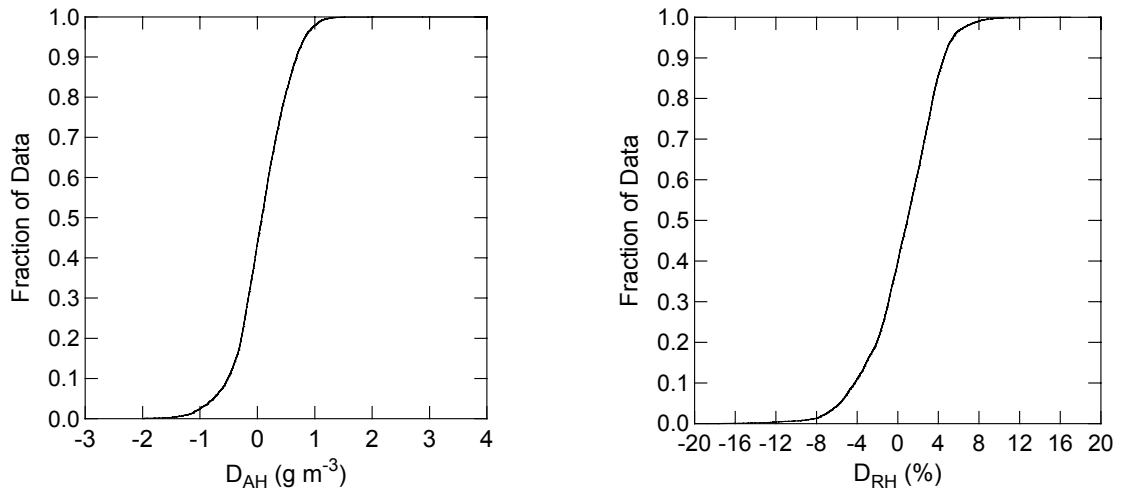


**Fig. 2-22.** Left: cumulative frequency distribution of the difference  $D_{AH}$  between measurement and model for the period from April 2002 to January 2003. Right: cumulative frequency distribution of the difference  $D_{RH}$  between measurement and model for the same period.

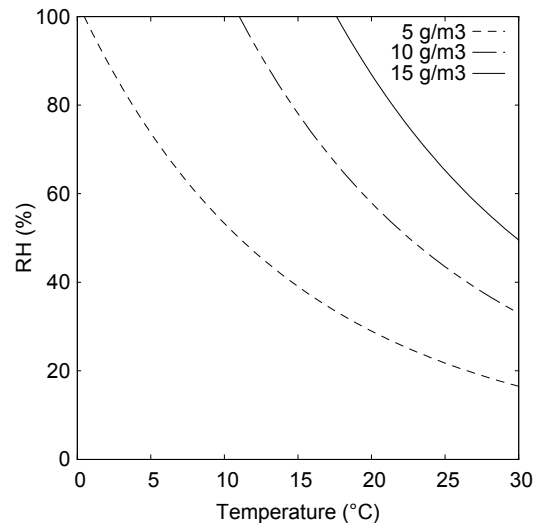


**Fig. 2-23.** Relationship between temperature and relative humidity.

The impact of the moisture buffering capacity of building envelope and furniture on air humidity has been assessed by performing a simulation with the hygric model with the surface of all absorbent materials set to zero (Fig. 2-24). Results show that the materials clearly affect the amplitude of the variations of absolute and relative humidity: according to the simulation, the total absence of absorbent materials leads to much stronger fluctuations.

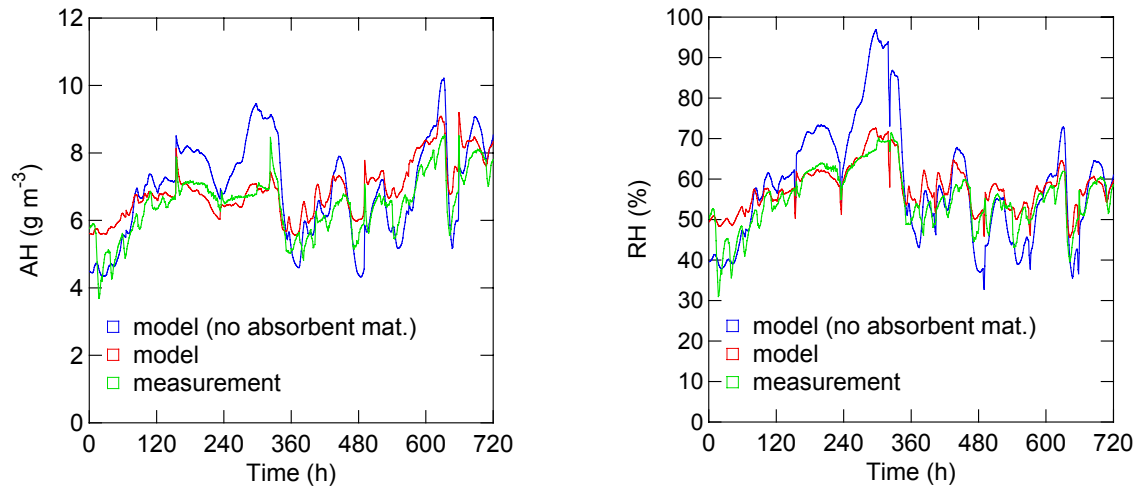


**Fig. 2-24.** Moisture buffering effect of building materials and furniture, computed for April 2002. Left: absolute humidity. Right: relative humidity.

### 2.3.3 Sensitivity tests

The thermal and the hygric model depend on a number of physical input parameters that, particularly in the case of historical buildings, cannot always be known with precision. Sensitivity tests were carried out in order to estimate the effect of individual parameter variations on the results of the simulations. Knowing how sensitive the simulations to these uncertainties are, allows to identify the parameters that must be determined with more care and the parameters for which an accurate specification is not essential. Furthermore, the variation of the input parameters gives precious indications about the reliability of the results, an information that cannot be obtained by just using single, supposedly precise, values.

For each investigated parameter, the simulations were run with two empirically chosen values,  $V_1$  and  $V_2$ . The results of the simulations with  $V_1$  and  $V_2$  were then compared with those obtained with the reference model ( $R$ ), calibrated according to sections 2.2.2.1 and 2.2.3. In the case of air change rate,  $V_1$  corresponds to the lowest value ( $0.02 \text{ h}^{-1}$ ) reported by Baumann (1993) from measurements in a church;  $V_2$  is a hypothetical high value ( $1 \text{ h}^{-1}$ ) which could occur e.g. in case of strong wind or increased opening of windows and doors. For the window glazing, the measured thickness of 2 mm input into the reference model already represents a minimum value among the commonly used glazing types. Therefore,  $V_1$  was chosen as possible overestimation of the thickness (4 mm), while  $V_2$  is meant to represent a more modern double-glazing. The sensitivity of the hygric model to the flow rate of indoor moisture was tested with no moisture sources ( $V_1 = 0 \text{ g h}^{-1}$ ) and with twice the value used in the reference model ( $V_2 = 240 \text{ g h}^{-1}$ ). For the other parameters,  $V_1$  and  $V_2$  were basically meant to cover a span arising from inaccuracies of rough estimates, i.e. a possible severe over- or underestimation. Since the consequences of parameter variations depend on the magnitude of

the values  $V_1$  and  $V_2$ , the results of the sensitivity tests should be regarded qualitatively in relation to the chosen values and not on a strictly quantitative basis.

The parameters investigated and the tested values were:

- *Air change rate* (Fig. 2-25a and Fig. 2-26a)  
 $V_1 = 0.02 \text{ h}^{-1}$ ,  $V_2 = 1 \text{ h}^{-1}$ . Since a modification of the air change rate causes a change of the estimated flow rate of indoor moisture (equation 2-27), the latter was adjusted for the tested values to  $q = 24 \text{ g h}^{-1}$  ( $V_1$ ) and  $q = 1200 \text{ g h}^{-1}$  ( $V_2$ ), respectively.
- *Total area of the external walls* (Fig. 2-25b and Fig. 2-26b)  
 $V_1$  and  $V_2$  varied by  $\pm 50\%$  of  $R$
- *Thickness of the external walls* (Fig. 2-25c and Fig. 2-26c)  
 $V_1 = 0.7 \text{ m}$ ,  $V_2 = 1.0 \text{ m}$
- *Area of the floor* (Fig. 2-25d and Fig. 2-26d)  
 $V_1$  and  $V_2$  varied by  $\pm 50\%$  of  $R$
- *Thickness of the floor* (Fig. 2-25e and Fig. 2-26e)  
 $V_1$  (thin) = cement tile (2 cm) over cement mortar (3 cm)  
 $V_2$  (thick) = cement tile (2 cm) over cement mortar (3 cm) over soil (1.5 m)
- *Area of the ceiling* (Fig. 2-25f and Fig. 2-26f)  
 $V_1$  and  $V_2$  varied by  $\pm 50\%$  of  $R$
- *Thickness of the ceiling* (Fig. 2-25g and Fig. 2-26g)  
 $V_1$  and  $V_2$  varied by  $\pm 50\%$  of  $R$
- *Total area of the window glazing* (Fig. 2-25h and Fig. 2-26h)  
 $V_1$  and  $V_2$  varied by  $\pm 50\%$  of  $R$
- *Thickness of the window glazing* (Fig. 2-25i and Fig. 2-26i)  
 $V_1 = 4 \text{ mm}$ ,  $V_2 = \text{double-glazing consisting of 2 sheets of 4 mm thickness separated by a 12 mm air space}$
- *Absorptivity of the external wall surfaces: façade* (Fig. 2-25j and Fig. 2-26j)  
 $V_1 = 0.40 \text{ mm}$ ,  $V_2 = 0.70$
- *Absorptivity of the external wall surfaces: other walls* (Fig. 2-25k and Fig. 2-26k)  
 $V_1 = 0.20 \text{ mm}$ ,  $V_2 = 0.40$
- *Total surface area of the furniture* (Fig. 2-25l and Fig. 2-26l)  
 $V_1 = \text{no furniture}$ ,  $V_2 = +100\%$  of  $R$
- *Indoor moisture source (flow rate)* (Fig. 2-26m)  
 $V_1 = 0 \text{ g h}^{-1}$ ,  $V_2 = 240 \text{ g h}^{-1}$

The results of the sensitivity tests are presented in Fig. 2-25 (thermal simulation) and Fig. 2-26 (hygric simulation). For each tested parameter, results are represented in two different plots: one giving for every tested value ( $V_1$ ,  $V_2$  and  $R$ ) the cumulative frequency distribution of the differences between measurement and model results; the other showing model results for a sample period of five days. The cumulative frequency distribution plot summarises the spread of the deviation and the shift of model results with respect to the measurements. For instance, in plot Fig. 2-25a left (air change rate), it can be seen that:

- The results obtained with the reference model ( $R$ ) and with an air change rate of  $0.02 \text{ h}^{-1}$  show basically the same distribution of deviations from the measurements. Between the two curves there is a shift reaching a maximum of  $0.1 \text{ }^{\circ}\text{C}$  which, given the accuracy of the temperature measuring equipment employed (ca.  $\pm 0.5 \text{ }^{\circ}\text{C}$ ), can be considered negligible.
- By increasing the air change rate to  $1 \text{ h}^{-1}$ , the difference between measurement and model moves by up to  $1 \text{ }^{\circ}\text{C}$  towards higher values, indicating that the calculated temperatures tend to be generally lower than those produced by the reference model, as can be seen in Fig. 2-25a right.

The results can be summarised as follows. The parameters that have a strong influence on the thermal simulation are air change rate, area of the ceiling and total area of the window glazing. Area and thickness of the external walls, thickness of the floor, thickness of the ceiling and absorptivity have a relatively moderate influence on the simulation results. Area of the floor, thickness of the window glazing and total surface area of the furniture have very little to no influence. For the hygric simulation, the parameters that show a significant influence on the computed RH are air change rate and indoor moisture source. A tenfold increase of air change rate from  $0.1 \text{ h}^{-1}$  to  $1 \text{ h}^{-1}$  (which in the given building could be triggered for example by strong winds or by an increased opening of windows and doors) leads to a deviation from the reference model up to about 15%. Omitting or doubling the indoor moisture source (flow rate of  $120 \text{ g h}^{-1}$  in the reference model) produces an RH variation of about  $\pm 10\%$ . All other parameters have little to no influence.

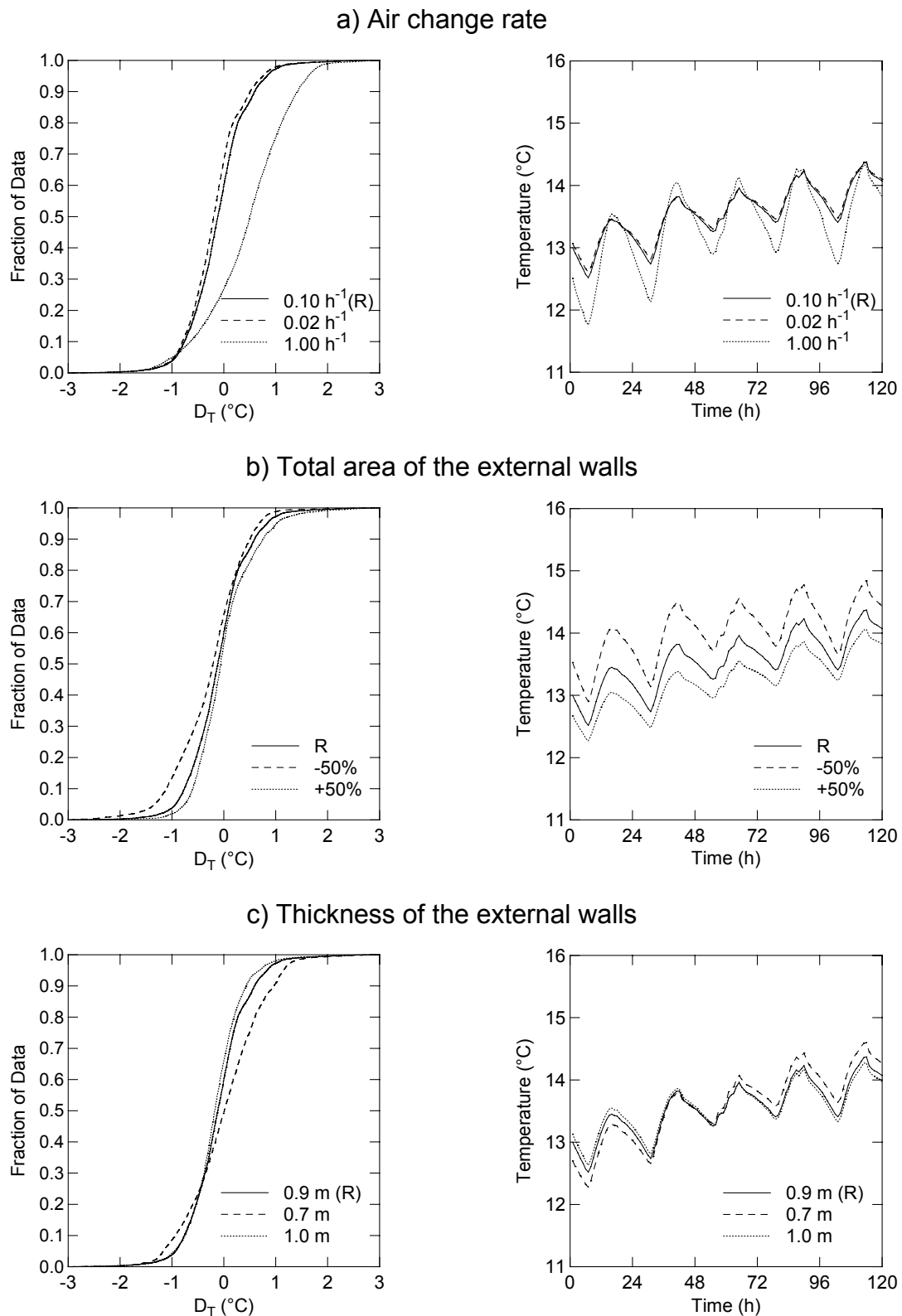
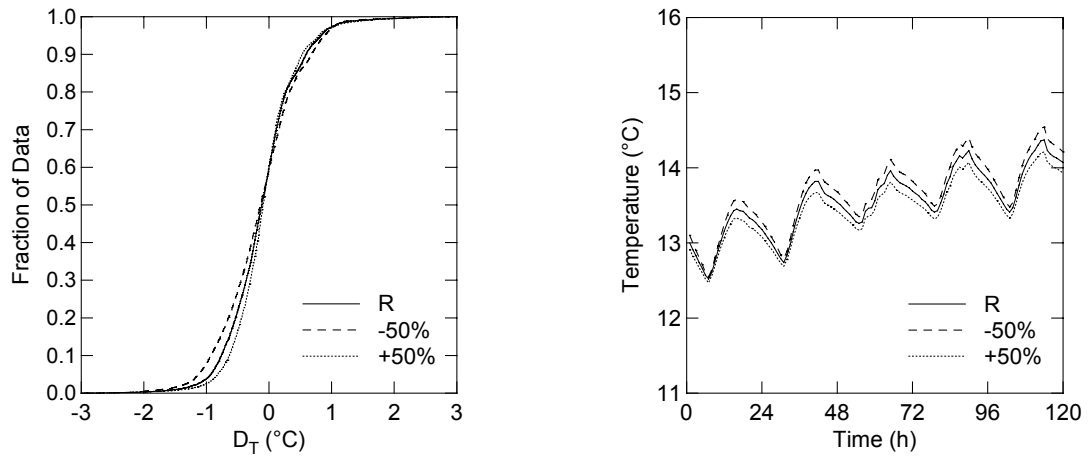
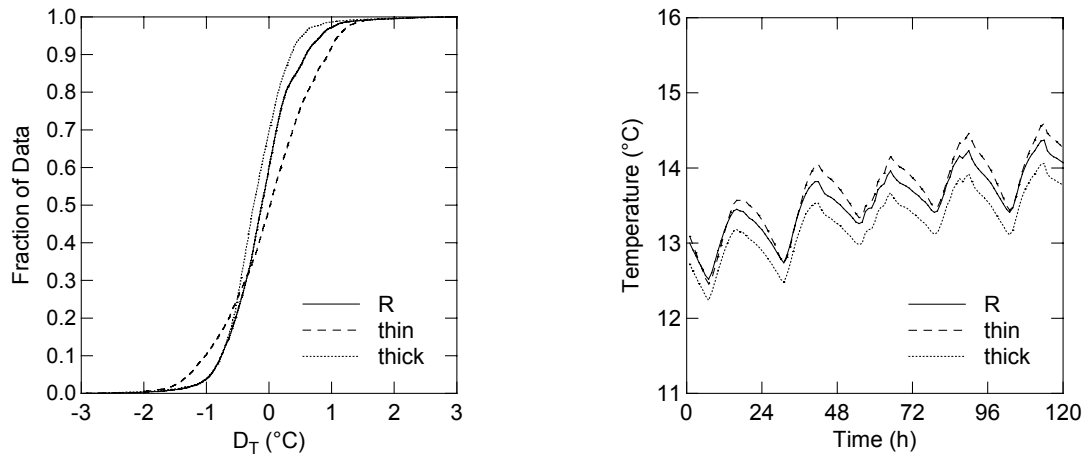


**Fig. 2-25.** Effect of parameter variations on the results of the thermal simulation. Left: cumulative frequency distribution of the differences  $D_T$  between measurement and model for the period from April 2002 to January 2003. Right: calculated temperatures for the period from April 1<sup>st</sup> to April 5<sup>th</sup> 2002.

d) Area of the floor



e) Thickness of the floor



f) Area of the ceiling

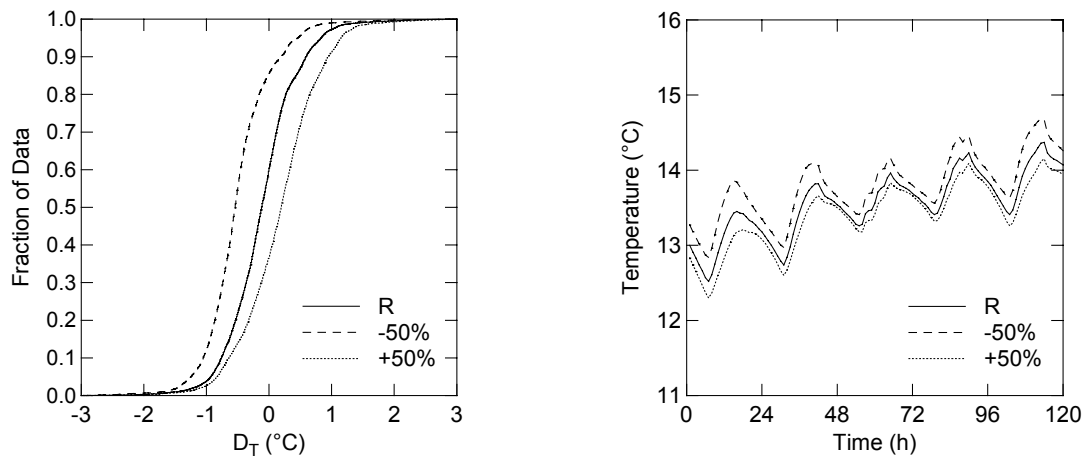
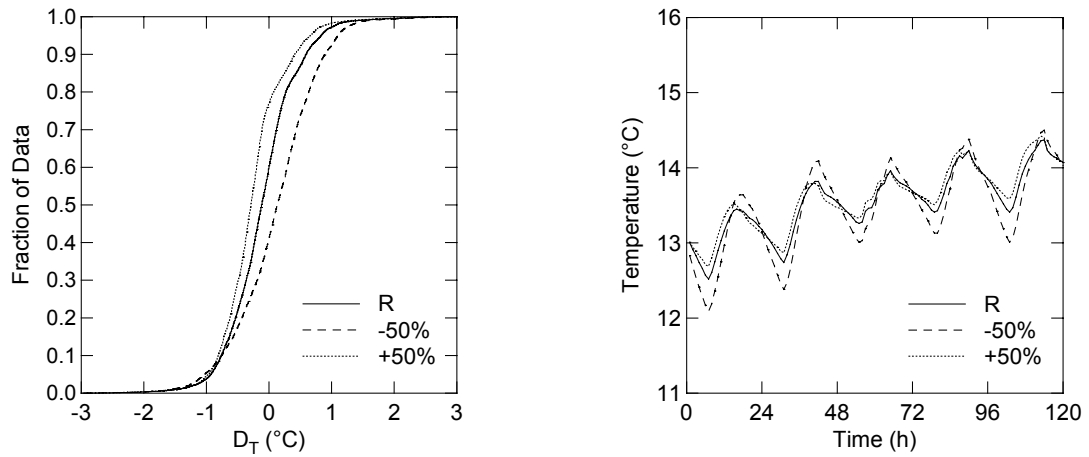
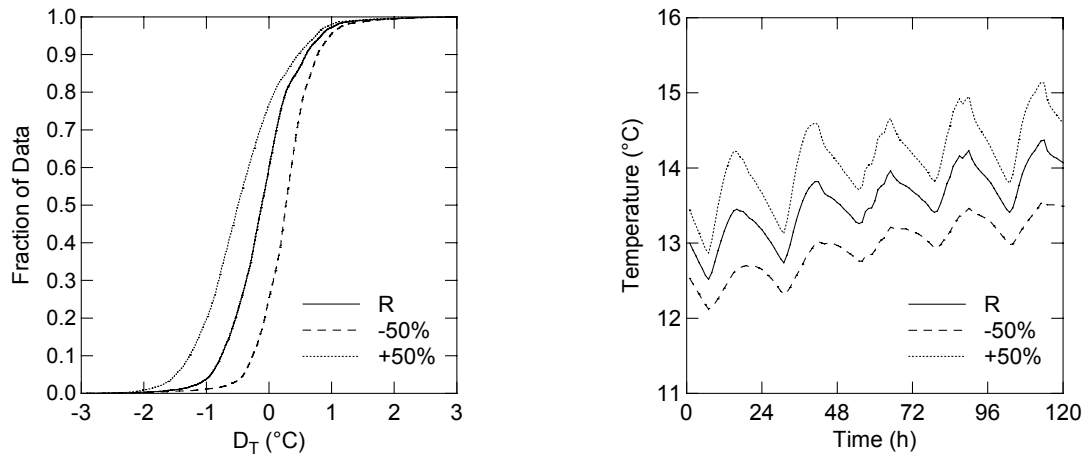


Fig. 2-25. (continued)

g) Thickness of the ceiling



h) Total area of the window glazing



i) Thickness of the window glazing

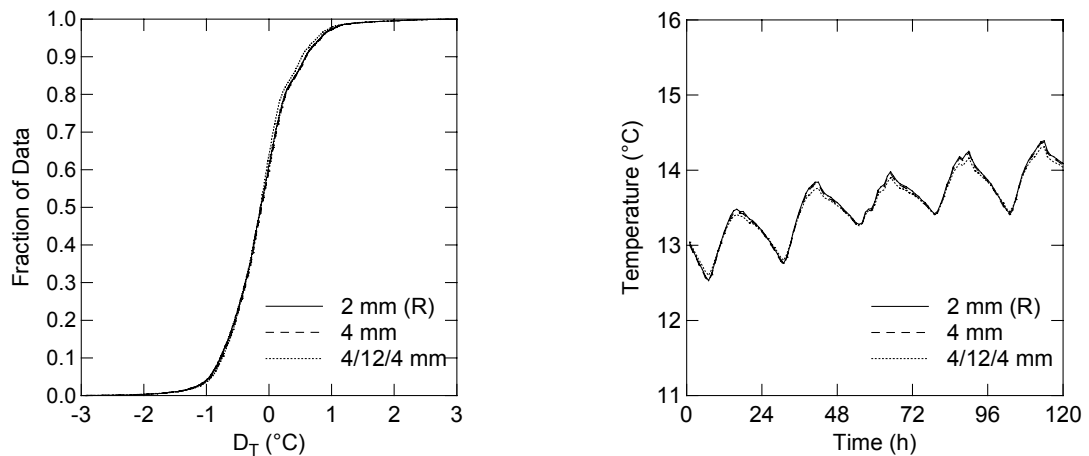
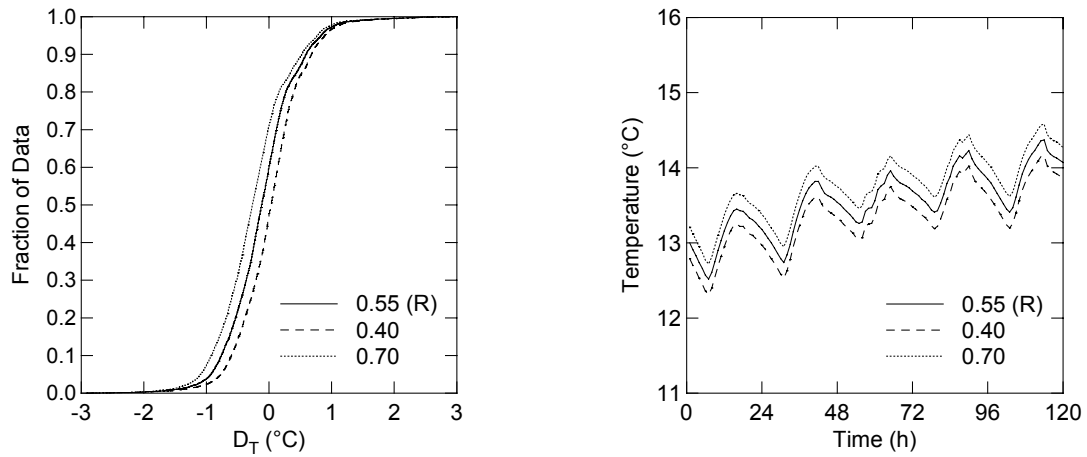
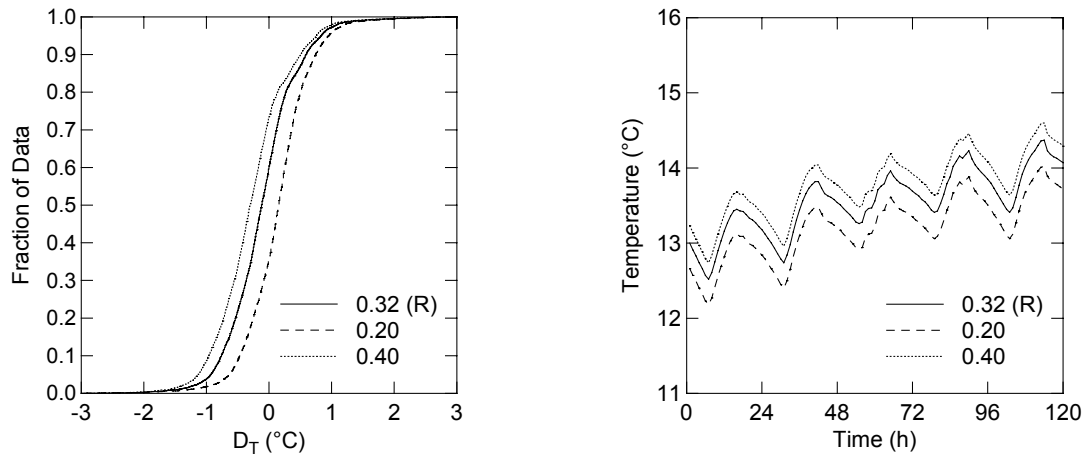


Fig. 2-25. (continued)

j) Absorptivity of the external wall surfaces: *façade*



k) Absorptivity of the external wall surfaces: other walls



l) Total surface area of the furniture

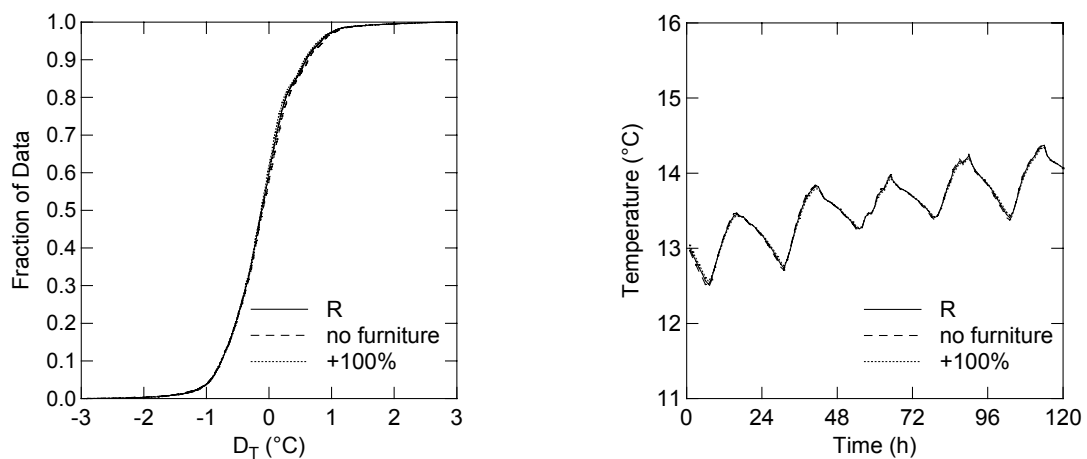
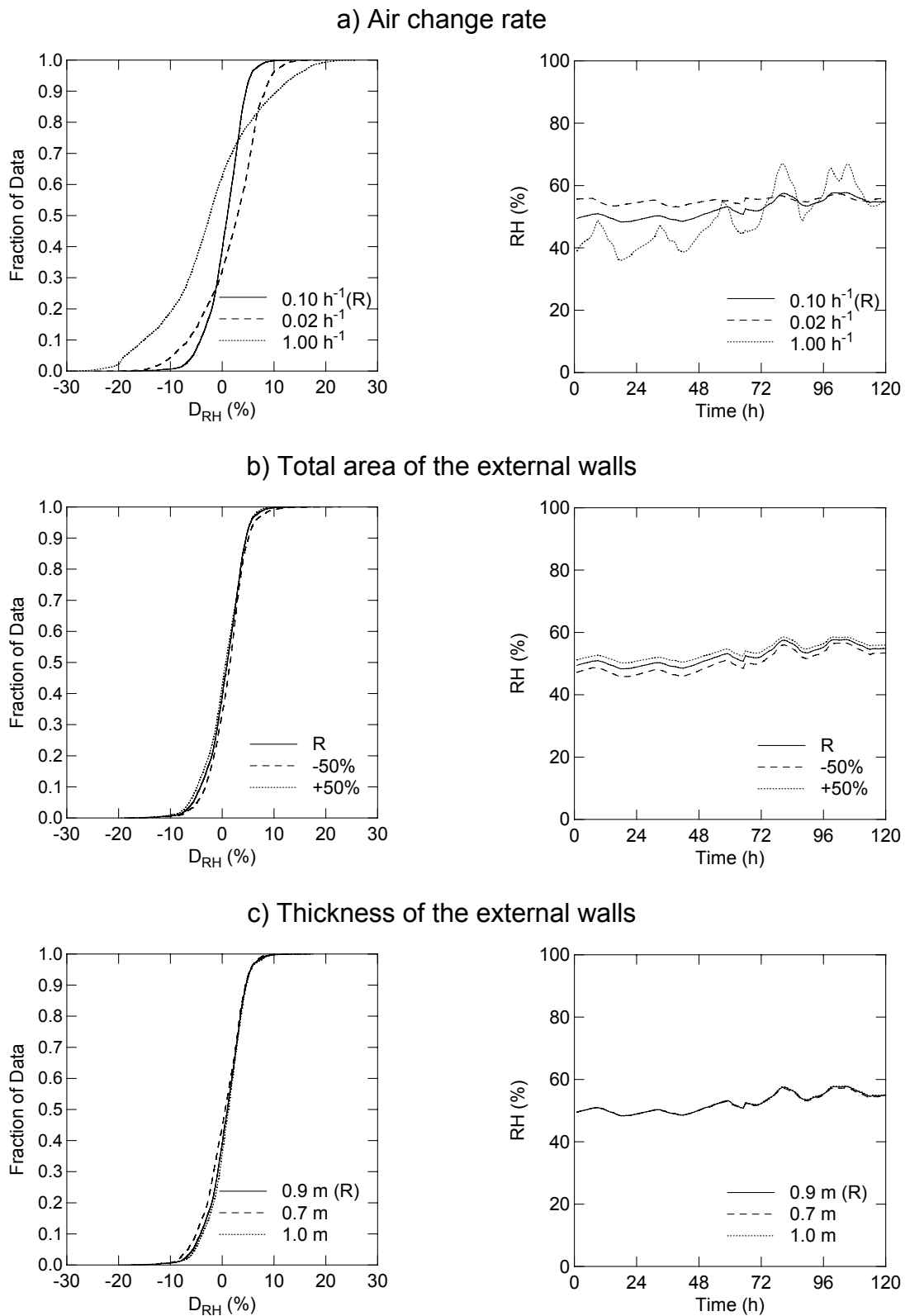


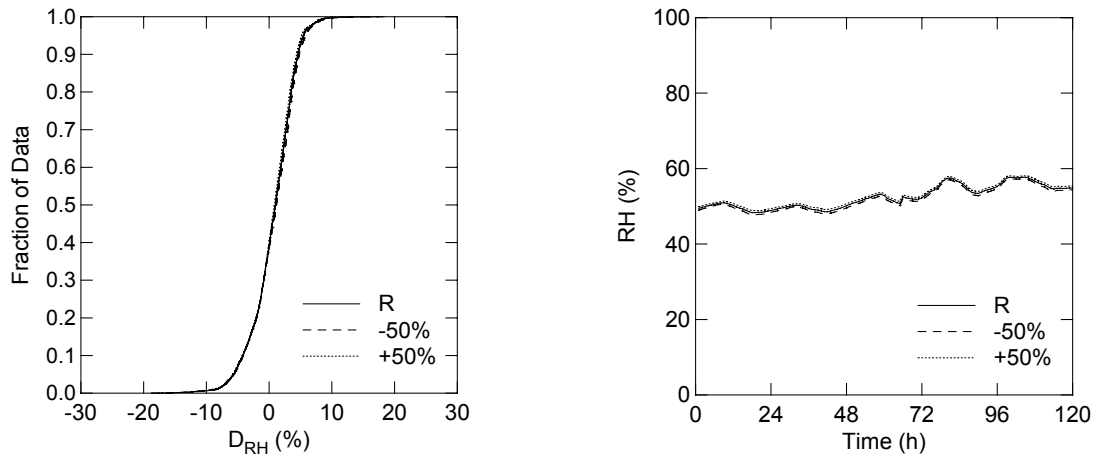
Fig. 2-25. (continued)



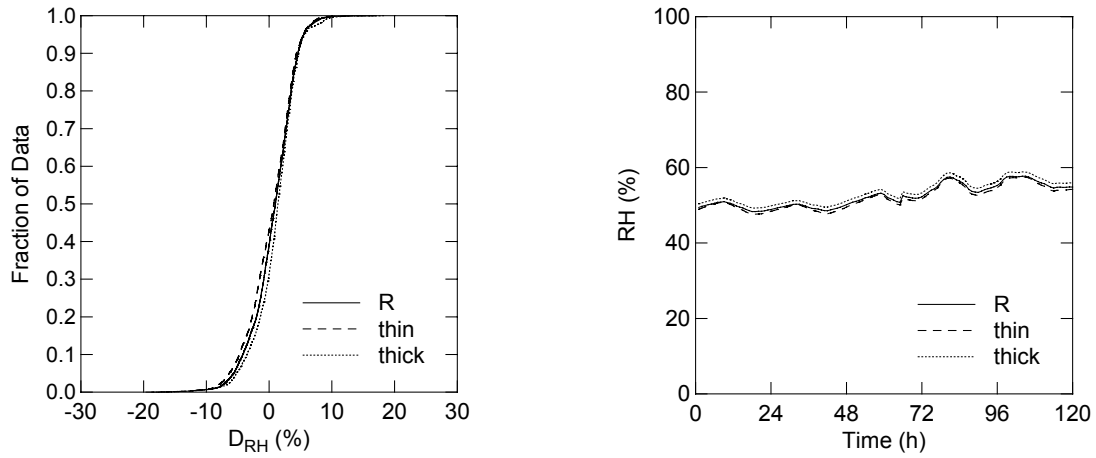


**Fig. 2-26.** Effect of parameter variations on the results of the hygric simulation. Left: cumulative frequency distribution of the differences  $D_{RH}$  between measurement and model for the period from April 2002 to January 2003. Right: calculated RH for the period from April 1<sup>st</sup> to April 5<sup>th</sup> 2002.

d) Area of the floor



e) Thickness of the floor



f) Area of the ceiling

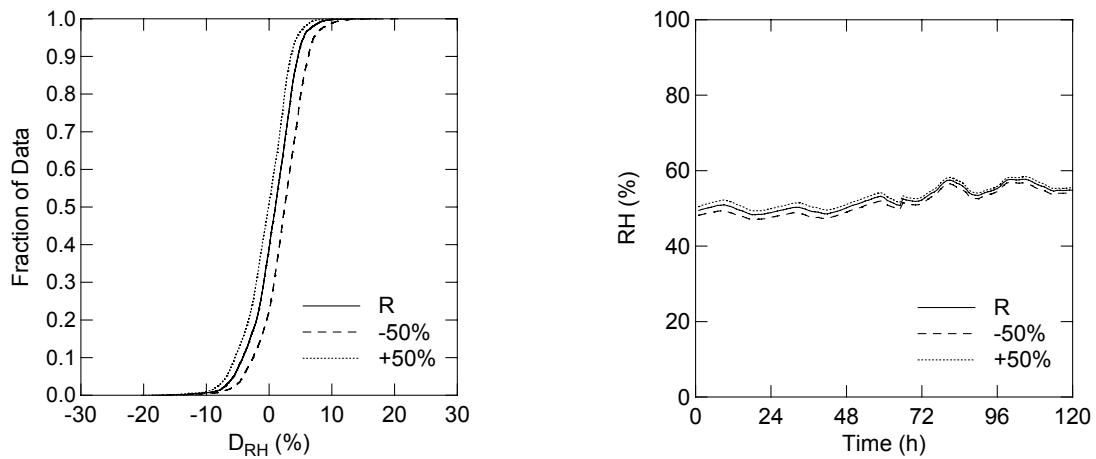
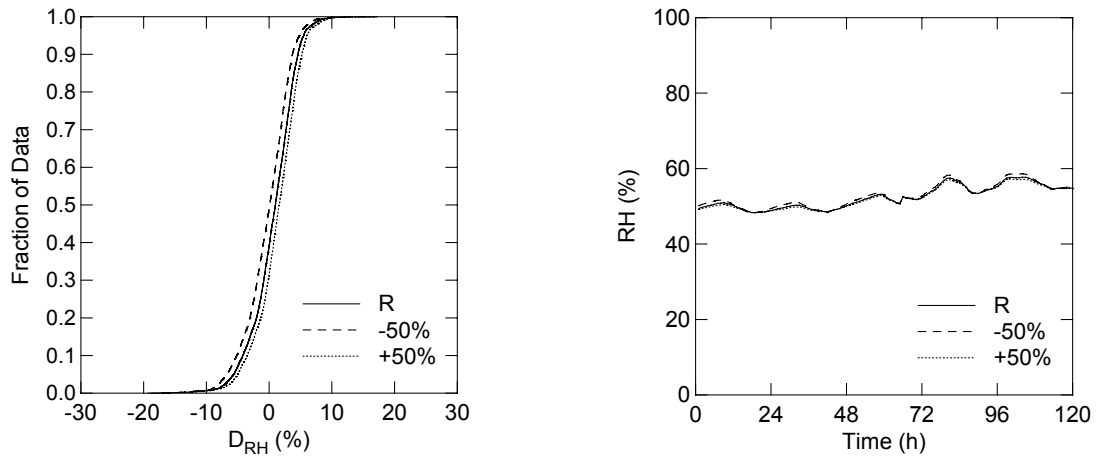
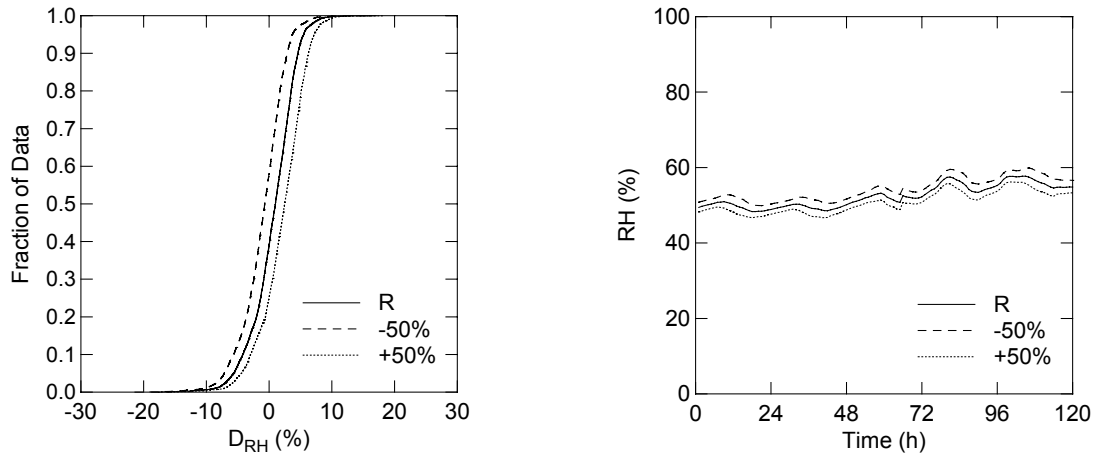


Fig. 2-26. (continued)

g) Thickness of the ceiling



h) Total area of the window glazing



i) Thickness of the window glazing

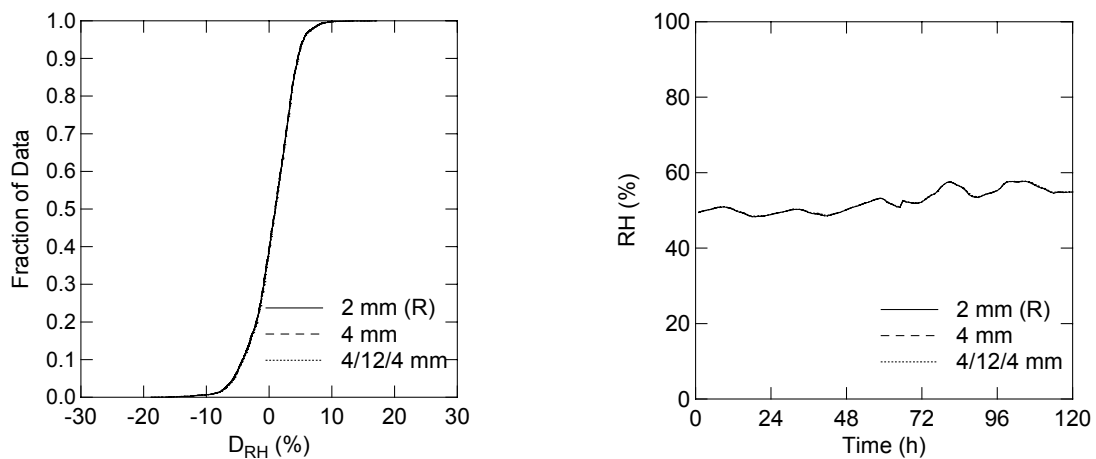
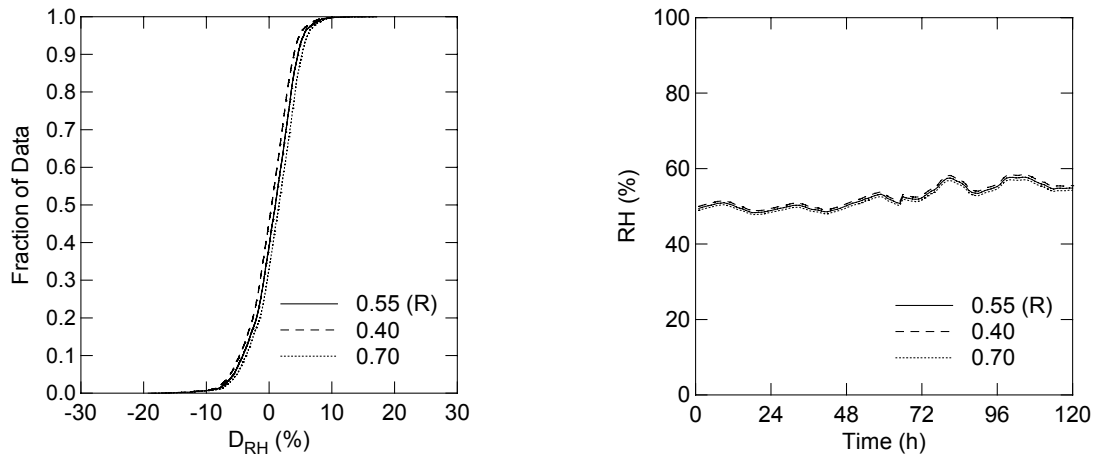
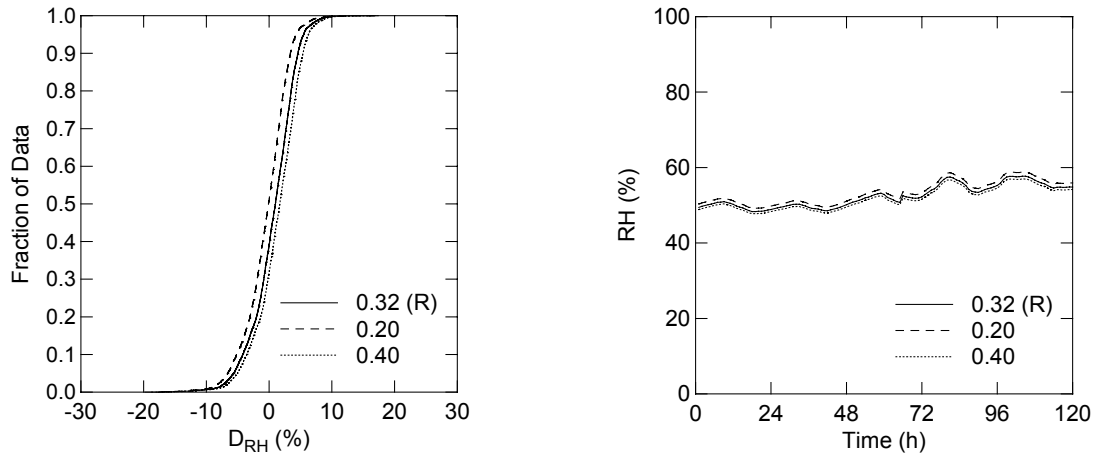


Fig. 2-26. (continued)

j) Absorptivity of the external wall surfaces: façade



k) Absorptivity of the external wall surfaces: other walls



l) Total surface area of the furniture

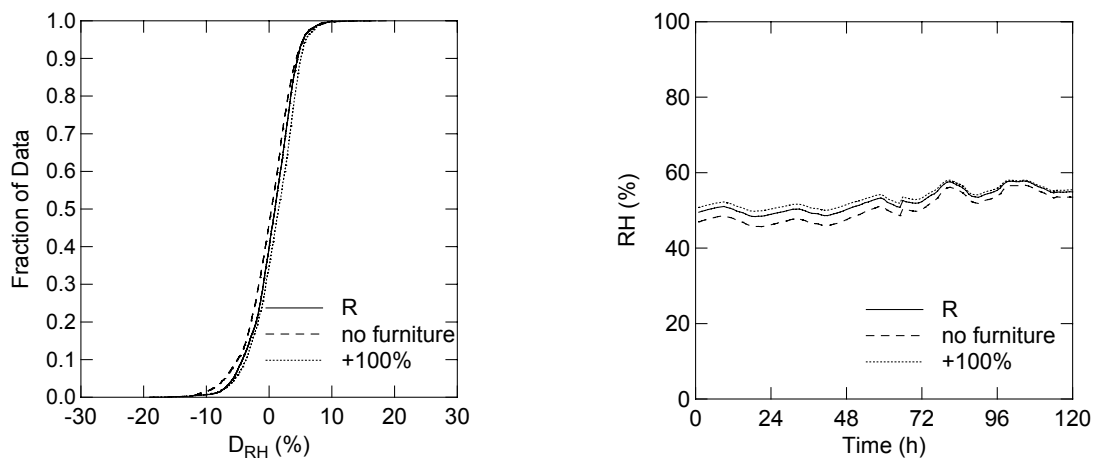


Fig. 2-26. (continued)

m) Indoor moisture source (flow rate)

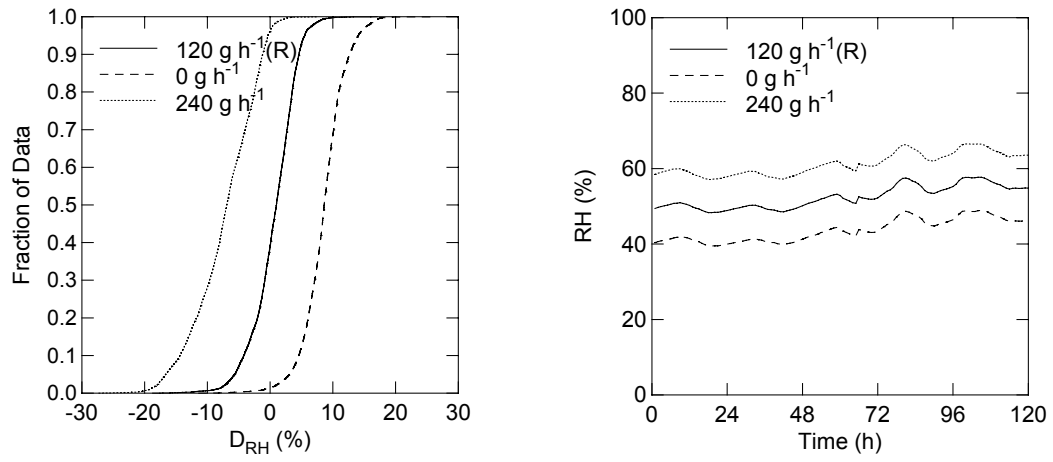


Fig. 2-26. (continued)

### 2.3.4 Building modifications and indoor climate

During year 2003, archaeological excavations were carried out by the cantonal service in the church San Pietro Martire. The works started at the beginning of June with the removal of the tiled floor, the cement layer, the lime mortar floor and the stone bed (Fig. 2-5). The actual archaeological excavations began at the end June and involved an area corresponding to about one half of the total floor surface of the nave. In that area, the lowermost lime mortar floor was also removed, exposing the underlying soil and the vestiges of a smaller precursor building (Fig. 2-27, left). The works lasted until mid November, when the excavated sector was filled with gravel; the floor slab was eventually remade in February-March 2004.

On the 5<sup>th</sup> of November, during in situ investigations, water condensation was noticed on large wall portions. The air temperature was 8.6 °C and the RH was 87%, which corresponds to a dew point temperature of ca. 6.6 °C. The temperature of the coldest wall sectors, measured by means of infrared thermography, was between 6 and 7 °C. The areas affected by condensation were mapped in detail and documented photographically. An additional temperature and RH logger was installed in the chancel, at a place where condensation was particularly marked. The instrument recorded the temperature of the wall plus the temperature and the RH of the air in proximity of the wall. The measurement showed that during the condensation phase the temperature of the wall was either very close or below dew point.

In spite of the anomalously hot and dry summer (see next section), a portion of the soil in the excavated sector was permanently moist throughout the whole period of exposure (Fig. 2-27, right). The surface temperature of this soil portion, assessed by infrared thermography the 5<sup>th</sup> of November, was ca. 9 °C, ruling out water condensation on the surface (dew point of the air was 6.6 °C, see above). This observation substantiated the hypothesis of the existence of a significant underground moisture source. By removing the floors (especially the less permeable cementitious upper layers) that acted as a resistance hindering water vapour diffusion, the vapour flux from the ground to the building's interior increased dramatically. This increased and steady moisture contribution from the ground, together with a rapid cooling of the building envelope due to an abrupt drop of the outdoor temperature that started in the second half of October, are considered as the causes of the observed condensation.

The expected evolution of the relative humidity in the unchanged building (i.e. no floor removal) was simulated for year 2003 on the basis of the thermal and the hygric reference models (sections 2.2.2.1 and 2.2.3) and compared with measurements recorded during that period. The simulation shows that the evolutions of measured and computed indoor relative humidity start to diverge markedly at the time when the floor was removed, with the measured RH growing up to 20% higher than the theoretical RH of the unchanged building (Fig. 2-28). These results confirm the hypothesis of an increased moisture flux caused by floor removal.



**Fig. 2-27.** Left: overview of the archaeological excavation with the vestiges of the precursor building. Right: detail showing the moist soil. The pictures were taken at the 5<sup>th</sup> of November 2003, approximately 4 months after removal of the lowermost lime floor.

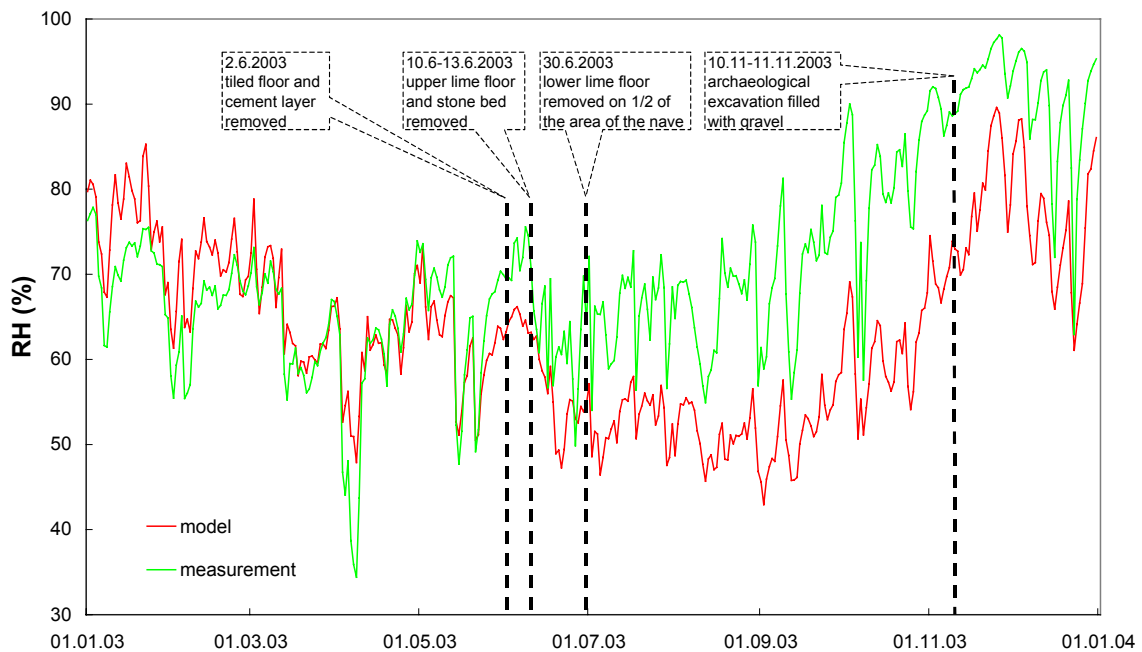


**Fig. 2-28.** Comparison of measured and simulated indoor relative humidity (daily mean values) for year 2003. Note the divergence of the two curves after the gradual removal of the floor.

### 2.3.5 Reconstruction of past indoor climate

The condensation event discussed in the previous section offered the opportunity to observe the development of damage on two sectors of the NE wall in the chancel, behind the altar. The damage manifested itself in the form of flaking of the paint layer, after drying of the surfaces at the end of January 2004 (Fig. 2-29 and Fig. 2-30 left). Fortunately, the damaged paint layers were not considered to be of particular artistic or historical value and their replacement was already foreseen by the restoration plans.

Condensation of water on surfaces can cause damage either on the surfaces on which it is occurring or on underlying surfaces if the water is allowed to flow downwards, as for example in the case of condensation on windowpanes (Fig. 2-30 right). The latter is a known issue (see e.g. Arendt, 1993, p. 68) which is frequently addressed by installing a gutter at the base of the windows in order to collect and, possibly, carry away the water.



**Fig. 2-29.** Sector on the NE wall behind the altar. Top: at the 6<sup>th</sup> of November 2003, during the condensation period. Bottom: at the 25<sup>th</sup> of January 2004, after drying of the surface, flaking of the paint layer has developed. Field of view is about 1 m.



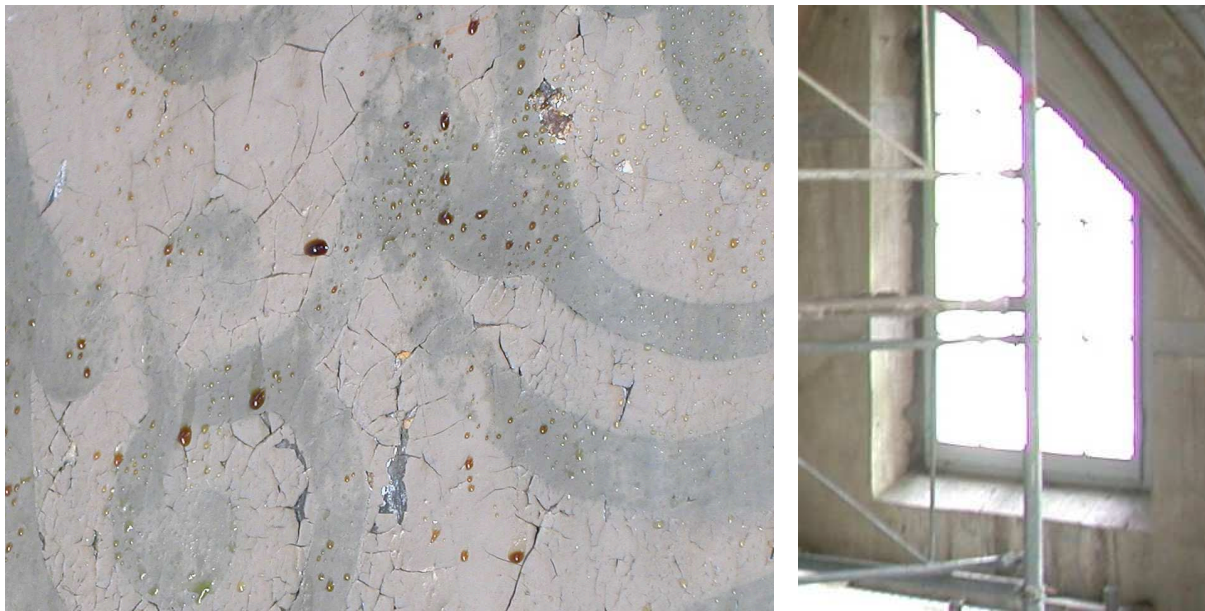


**Fig. 2-30.** Different forms of condensation damage observed in the church San Pietro Martire. Left: detail of the wall sector shown in Fig. 2-29 (6<sup>th</sup> of November 2003), displaying an initial cracking of the paint layer that later degenerated into flaking when the surface completely dried. In this picture it is also visible how condensation drops are dissolving water-soluble components of the paint layer, thus aggravating damage. Field of view is about 15 cm. Right: dark vertical marks below a window, probably caused by water condensating on the glazing and flowing downwards. In this case, however, infiltration of water through window joints during rainstorms might also have contributed to damage.

The frequency of condensation episodes in the church San Pietro Martire during the 20-years-period 1983-2002 was assessed on the basis of the thermal and the hygric reference models (sections 2.2.2.1 and 2.2.3). This provided an estimation of the risk of condensation on walls and windowpanes. HELIOS was used to calculate the temperature of the indoor air and of the interior building surfaces, while the hygric model was used to calculate the humidity of the air. The results are shown in Fig. 2-31 (condensation on walls) and Fig. 2-32 (condensation on windowpanes).

Condensation on walls was calculated to have been possible for a total time of 32 (wall SE) to 55 hours (wall NW) during the whole 20-years period (175'200 hours), which corresponds to ca. 0.02 to 0.03% of the time. This shows that condensation on walls, although not impossible in that church, is a rather extraordinary phenomenon. Condensation on windowpanes was calculated to have been possible for a total time of 3469 (windows on the SE side) to 3486 hours (windows on the NW side) during the whole period, which amounts to 145 days on average, i.e. about 2% of the time. Occurrence of condensation on windowpanes is, therefore, not so uncommon, being up to two orders of magnitude more frequent than condensation on walls.

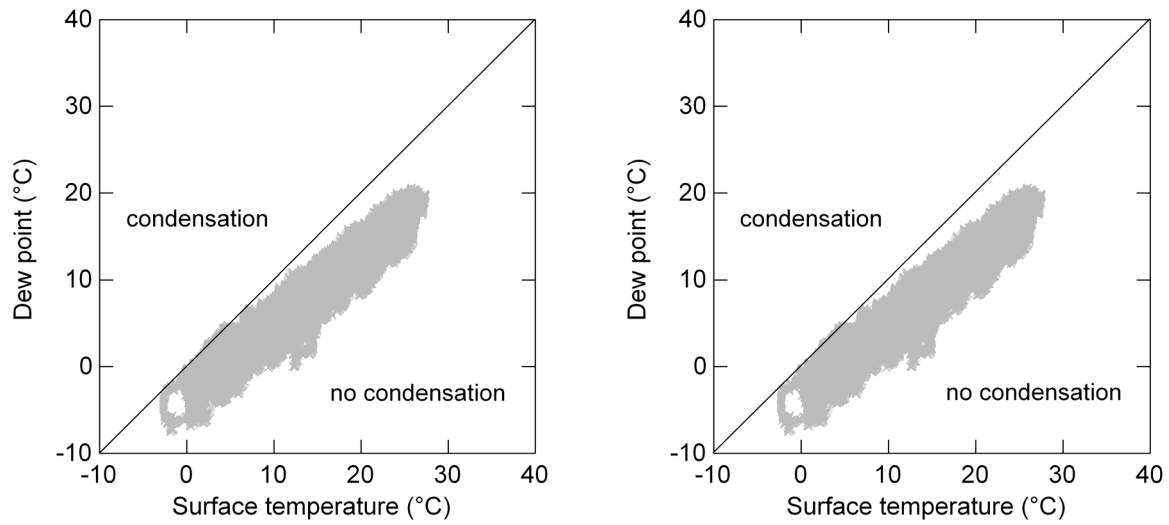


**Fig. 2-31.** Risk of condensation on walls calculated for the period 1983-2002 (hourly values, i.e. 175'200 data points). Left: wall NW; 55 data points are in the condensation region, which corresponds to about 0.03% of the total time. Right: wall SE; 32 data points are in the condensation region, which corresponds to about 0.02% of the total time.

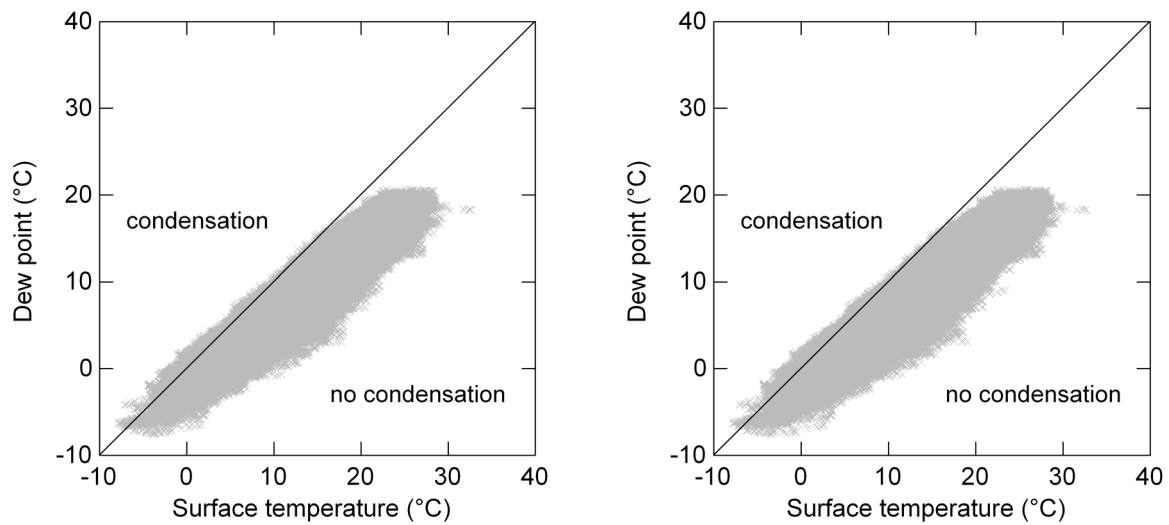


**Fig. 2-32.** Risk of condensation on windowpanes calculated for the period 1983-2002 (hourly values, i.e. 175'200 data points). Left: windows on the NW side; 3486 data points are in the condensation region. Right: windows on the SE side; 3469 data points are in the condensation region. On average, the estimated total condensation time during the 20-years-period corresponds to about 145 days, i.e. about 2% of the time.

In many European regions, summer 2003 was probably the hottest since year 1500 (Luterbacher et al., 2004). In a large area of central Europe, the mean summer temperatures (calculated from the June, July and August months) exceeded the 1961-1990 mean by about 3 °C, which corresponds to an excess of up to 5 standard deviations (Schär et al., 2004). Climatologically anomalous years like 2003 can have a noticeable effect on the indoor climate of buildings.

The impact of the summer 2003 heat-wave on the indoor climate of the church San Pietro Martire in Gnosca was simulated using the thermal and the hygric reference models (sections 2.2.2.1 and 2.2.3). The results of the simulation for the period 1983-2003 are shown in Fig. 2-33 in the form of cumulative frequency distribution plots. When compared with the simulated indoor climate of the previous 20 years, temperature and RH distribution of year 2003 stand out as clear outliers.

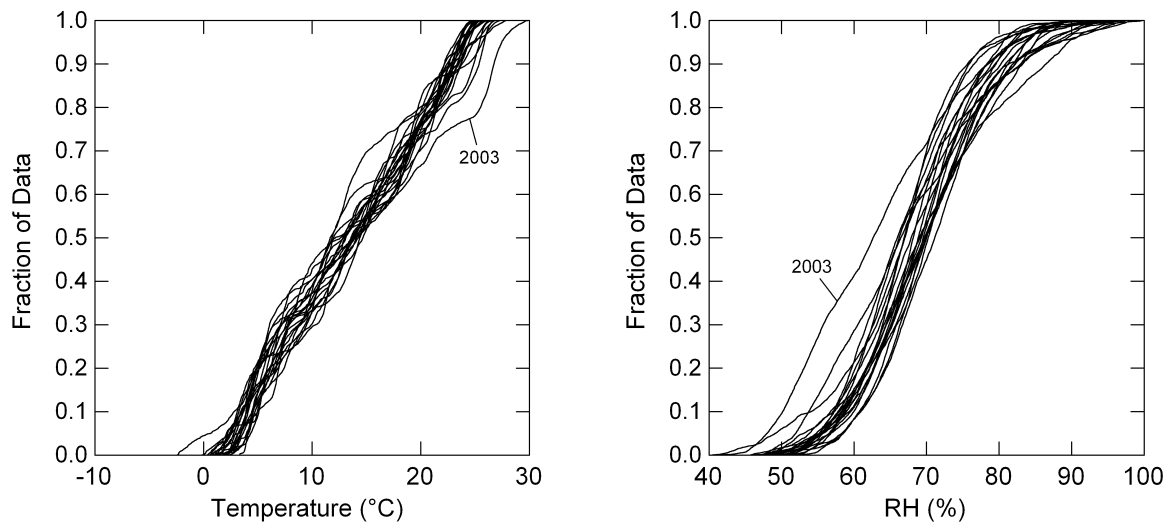


**Fig. 2-33.** Cumulative frequency distribution plots showing the cumulative frequency distribution of the simulated temperature (left) and RH (right) for the period 1983-2003. Every curve corresponds to one year; year 2003 is a clear outlier. See text for explanation.

## 2.4 Discussion

With the building energy simulation program HELIOS it has been possible to obtain a long-term estimation of the temperature in the building that is very close to the real values recorded in situ. For the indoor air, the difference between measurement and model ranged from  $-1.4$  to  $+1.2$  °C for almost the totality (95%) of the values, computed in 1-hour steps over a period of ten months. For the surface temperature of the NW wall, the discrepancy ranged from  $-1.6$  to  $+0.9$  °C over a period of three months. Considering that 1) the temperatures computed by the simulations are mean values, thus assuming thermal homogeneity of indoor air and wall surfaces, and that 2) the accuracy of the measuring equipment employed is about  $\pm 0.5$  °C, the accuracy attained by the thermal simulations can be considered as satisfactory.

The humidity of the indoor air was computed with the hygric model (Simmler et al., 1995; 1996) on the basis of the temperatures generated by HELIOS. Over a period of ten months, the discrepancy between measurement and model varied from  $-0.9$  to  $+1.0$  g m<sup>-3</sup> (absolute humidity) and  $-6.5$  to  $+7.7\%$  (relative humidity) for almost the totality (95%) of the computed hourly values. The accuracy of the measuring equipment employed is  $\pm 2\%$  RH.

The calculation of RH is based on the absolute humidity and the simulated air temperature. An error in the temperature affects the resulting RH exponentially; as shown in Fig. 2-23, a variation of  $\pm 1$  °C at a temperature of 15 °C and an absolute humidity of 10 g m<sup>-3</sup> causes an RH variation of nearly  $\pm 5\%$ . This can partly explain the observed difference between measured and simulated RH. If a hygric model is to be combined with a thermal model, it is therefore essential that the computed temperatures are as accurate as possible. Such accuracy implies the availability of meteorological data representative of the object's site, as well as a thorough calibration of the model, especially of those parameters that have a strong impact on the simulation.

The meteorological parameters required by HELIOS are the hourly values of global, diffuse and infrared radiation, temperature, RH, wind speed and frequency, emissivity of the sky and of the surroundings (Table 2-8). Depending on the distance of the meteorological station providing the data, it might be advisable to perform a preliminary check of their suitability. This might be achieved by comparing METEONORM data for the meteorological station site with that for the object's site. As alternative, temperature and RH from the meteorological station can be directly compared with measurements at the object's site. In the present study, hourly temperature and RH from the meteorological dataset used for the simulations (station Locarno-Monti) followed the same trend and were overall in good agreement with own measurements outside the building in Gnosca (Fig. 2-7).

The input parameters required by the models were determined on the basis of detailed in situ investigations (e.g. surface area and thickness of the different structures, material types), derived from the literature (e.g. thermophysical properties of the materials) or determined

experimentally in the laboratory (e.g. hygric properties of the materials). Thanks to renovation works and to the archaeological excavation taking place in the building, it has been possible to gather information that would otherwise not be available without a destructive intervention. This was the case for the determination of the structure of the floor, of the walls and of the ceiling, as well as for the sampling of building materials like plasters and floor tiles. In situations where such invasive sampling is not possible, these features are to be approximated. It is therefore important to identify those parameters for which estimation errors made during the calibration of the model can have a significant impact on the results of the simulations.

Sensitivity tests show that for the air change rate, the area of the ceiling and for the total area of the window glazing, variations covering possible estimation errors generated temperature deviations from the reference model up to 0.5-1 °C. For the other parameters tested, the deviations were less relevant or negligible, that is below the accuracy of the employed temperature logger. In the case of the hygric simulation, the parameters that showed the greatest impact on the computation of RH are air change rate and indoor moisture source. A tenfold air change rate increase from 0.1 h<sup>-1</sup> to 1 h<sup>-1</sup> (which in the given building could be triggered for example by strong winds or by an increased opening of windows and doors) led to a deviation from the reference model up to about 15%. Omitting or doubling the indoor moisture source (flow rate of 120 g h<sup>-1</sup> in the reference model) produces an RH variation of about ±10%. From these results it is evident that those elements through which a significant heat or humidity transfer can occur, are also those that mostly affect the results of the simulations and that consequently have to be assessed with much care. How difficult this can be, depends on the peculiarities of the building.

In the present study, it has been possible to assume a constant air change rate, which was estimated by calculating air infiltration through windows and door joints. In the case of buildings with a very irregular ventilation however, a proper assessment of the air change rate may require an experimental determination under different ventilation regimes (e.g. by means of the tracer gas method).

The water vapour flux from indoor sources is of paramount importance for modelling indoor air humidity but, as in the case of ground moisture, is generally difficult to quantify with accuracy. In the present study, a flow rate was calculated in hourly intervals over a period of one year from the difference in water content between indoor and outdoor air, the air change rate and the indoor air volume (equation 2-27). Simulations carried out with a mean flow rate of 120 g h<sup>-1</sup> showed a better fit with the measurements than simulations with the hourly flow rates. The fact that, despite the large fluctuations in the hourly vapour flow rates, the simulation with the mean value provided the best results, indicates that the dynamics of the hygric behaviour of the building cannot be reproduced in all its complexity by a simple equation like (2-27). This suggests a certain hygric inertia of the building towards humidity fluctuations, explainable by the buffering capacity of the hygroscopic building materials,

which was also depicted by model calculations (Fig. 2-24). The mean vapour flow rate calculated as above appears to represent a reasonable approximation of the actual indoor moisture sources.

Most advanced building energy codes like for example HELIOS require as input a fairly large set of building and meteorological parameters. All these parameters are not always available or might not fit well the situation, as is often the case with meteorological data when the measuring station is far away from the building's site. In addition, the use of the models can be demanding both in terms of time investment and required building physics knowledge. There might be however a whole category of (historical) buildings, whose thermal behaviour can be described with much simpler models.

In section 2.3.1.2 it was shown that, with a very simple building specification and on the basis of only few meteorological parameters, i.e. local temperature (3 measurements per day), as well as solar and long-wave radiation data from the METEONORM database, it is already possible to obtain a reasonable estimate of free-floating indoor temperatures. Computations were performed with an own model developed in the course of this study (section 2.2.2.2) for the Holy Cross chapel in Müstair and for the church San Pietro Martire in Gnosca. For the Holy Cross chapel, the difference between measured temperature and model prediction, over a period of three years (2001-2002), ranged from  $-1.0$  to  $1.5$  °C for 95% of the computed values. A comparison of the simulation for the church San Pietro Martire with results obtained with HELIOS shows that discrepancies are mainly due to the simple design of the own model, in particular the neglected solar heat gains through windows. Nevertheless, such a simple modelling approach can constitute a practical way to obtain a first approximation of the indoor temperature in situations where the application of more complete models is not possible or not necessary.

## 3 SALTS

### 3.1 Introduction

In the study object, observed damage on walls is mainly due to salt weathering. Salt weathering is a very important cause of decay for porous materials in historical buildings, see e.g. Goudie and Viles (1997) and the reviews on the subject by Charola (2000), Doehne (2002) and Evans (1970). The salts commonly found in buildings are listed in Table 3-1. Prerequisites for salt weathering are a sufficient supply of salts and the presence of moisture, which allows salt transport and accumulation in the pore system and facilitates chemical reactions. Moisture can be supplied either as liquid water (e.g. capillary rise in walls) or as water vapour from the atmosphere. Deterioration is caused chiefly by repeated crystallization-dissolution cycles and additionally, for salts that can exist in more than one hydration state, by hydration-dehydration cycles. These processes are strongly controlled by water activity and temperature.

At equilibrium, the chemical potential of liquid water  $\mu_{w,l}$  is equal to that of water vapour  $\mu_{w,v}$ . Assuming ideal gas behaviour for water vapour, we have (Steiger and Zeunert, 1996)

$$\mu_{w,l} = \mu_{w,l}^0 + RT \ln(a_w) = \mu_{w,v} = \mu_{w,v}^0 + RT \ln(p_w/p_w^0) \quad (3-28)$$

where  $R$  is the gas constant,  $T$  is the absolute temperature,  $a_w$  is the water activity,  $p_w$  is the water vapour partial pressure and  $p_w^0$  is the saturated water vapour pressure at temperature  $T$ . Since the standard chemical potentials  $\mu_{w,l}^0$  and  $\mu_{w,v}^0$  for water in the liquid and vapour phases are equal, we obtain

$$a_w = p_w/p_w^0 = RH \quad (3-29)$$

where  $RH$  is the relative humidity. Equation (3-29) depicts the relationship between the water activity in a salt solution and the surrounding environment. If the  $RH$  of the air in equilibrium with a salt solution is raised, the solution will pick up water ( $a_w$  increases). If the  $RH$  of the air is lowered, water will evaporate from the solution ( $a_w$  decreases) and the concentration of the salt will increase until saturation is reached. The  $RH$  of the air at that point is called the equilibrium relative humidity ( $RH_{eq}$ ). A further reduction of the  $RH$  will ultimately lead to supersaturation and precipitation of the salt. Every soluble salt has a specific equilibrium  $RH$ . Thus, if the ambient  $RH$  is lower than  $RH_{eq}$ , it is the solid salt that exists in equilibrium. If the ambient  $RH$  is higher than  $RH_{eq}$ , the salt will absorb water vapour. Very soluble salts may

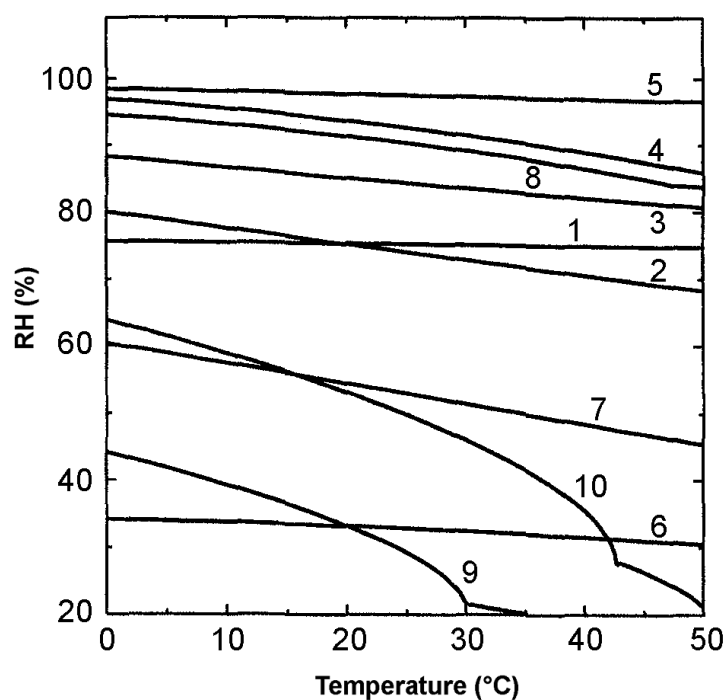
absorb enough water vapour under normal environmental conditions to form a saturated solution, a process which is termed deliquescence.

**Table 3-1.** Principal salts found in building walls (Arnold and Zehnder, 1991).

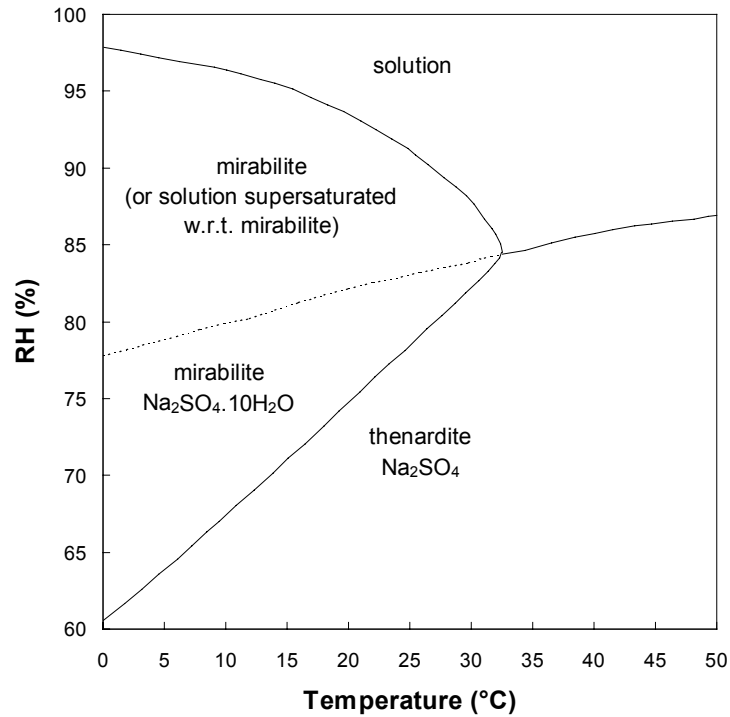
	Name	Chemical formula
<i>carbonates</i>	calcite	$\text{CaCO}_3$
	dolomite	$\text{CaMg}(\text{CO}_3)_2$
	magnesite	$\text{MgCO}_3$
	nesquehonite	$\text{MgCO}_3 \cdot 3\text{H}_2\text{O}$
	lansfordite	$\text{MgCO}_3 \cdot 5\text{H}_2\text{O}$
	hydromagnesite	$\text{Mg}_5(\text{OH}(\text{CO}_3)_2)_2 \cdot 4\text{H}_2\text{O}$
	natron	$\text{Na}_2\text{CO}_3 \cdot 10\text{H}_2\text{O}$
	thermonatrite	$\text{Na}_2\text{CO}_3 \cdot \text{H}_2\text{O}$
	nahcolite	$\text{NaHCO}_3$
	trona	$\text{Na}_3\text{H}(\text{CO}_3)_2 \cdot 2\text{H}_2\text{O}$
	kalicinite	$\text{KHCO}_3$
<i>sulphates</i>	gypsum	$\text{CaSO}_4 \cdot 2\text{H}_2\text{O}$
	bassanite	$\text{CaSO}_4 \cdot 1/2\text{H}_2\text{O}$
	epsomite	$\text{MgSO}_4 \cdot 7\text{H}_2\text{O}$
	hexahydrate	$\text{MgSO}_4 \cdot 6\text{H}_2\text{O}$
	kieserite	$\text{MgSO}_4 \cdot \text{H}_2\text{O}$
	darapskite	$\text{Na}_3(\text{SO}_4)(\text{NO}_3) \cdot \text{H}_2\text{O}$
	mirabilite	$\text{Na}_2\text{SO}_4 \cdot 10\text{H}_2\text{O}$
	thenardite	$\text{Na}_2\text{SO}_4$
	arcanite	$\text{K}_2\text{SO}_4$
	bloedite (astracanite)	$\text{Na}_2\text{Mg}(\text{SO}_4)_2 \cdot 4\text{H}_2\text{O}$
	picromerite (schoenite)	$\text{K}_2\text{Mg}(\text{SO}_4)_2 \cdot 6\text{H}_2\text{O}$
	boussingaultite	$(\text{NH}_4)_2\text{Mg}(\text{SO}_4)_2 \cdot 6\text{H}_2\text{O}$
	syngenite	$\text{K}_2\text{Ca}(\text{SO}_4)_2 \cdot \text{H}_2\text{O}$
	gorgeyite	$\text{K}_2\text{Ca}_5(\text{SO}_4)_6 \cdot \text{H}_2\text{O}$
	aphthitalite (glaserite)	$\text{K}_3\text{Na}(\text{SO}_4)_2$
	ettringite	$\text{Ca}_6\text{Al}_2(\text{SO}_4)_3(\text{OH})_{12} \cdot 26\text{H}_2\text{O}$
	thaumasite	$\text{Ca}_3\text{Si}(\text{OH})_6(\text{CO}_3)(\text{SO}_4) \cdot 12\text{H}_2\text{O}$
<i>chlorides</i>	bischofite	$\text{MgCl}_2 \cdot 6\text{H}_2\text{O}$
	antarcticite	$\text{CaCl}_2 \cdot 6\text{H}_2\text{O}$
	tachyhydrite	$\text{CaMg}_2\text{Cl}_6 \cdot 12\text{H}_2\text{O}$
	halite	$\text{NaCl}$
	sylvite	$\text{KCl}$
<i>nitrates</i>	nitrocalcite	$\text{Ca}(\text{NO}_3)_2 \cdot 4\text{H}_2\text{O}$
	nitromagnesite	$\text{Mg}(\text{NO}_3)_2 \cdot 6\text{H}_2\text{O}$
	nitratine	$\text{NaNO}_3$
	niter	$\text{KNO}_3$
	ammonium nitrate	$\text{NH}_4\text{NO}_3$
<i>oxalates</i>	whewellite	$\text{Ca}(\text{C}_2\text{O}_4) \cdot \text{H}_2\text{O}$
	weddellite	$\text{Ca}(\text{C}_2\text{O}_4) \cdot 2\text{H}_2\text{O}$



Fig. 3-1 shows the equilibrium RH of some common salts in relation to temperature. Phase diagrams for  $\text{Na}_2\text{SO}_4$  and  $\text{MgSO}_4$ , two common salts that can exist in different hydration states, are shown in Fig. 3-2 and Fig. 3-3. The phase transitions from one hydration state to the other can occur at temperature and relative humidity conditions found inside buildings. Historical monuments are rarely contaminated by a single salt species, but more commonly by complex mixtures for which the equilibrium RH of pure salts no longer apply; the salts generally start to deliquesce at lower values (e.g. Price and Brimblecombe, 1994; Steiger and Dannecker, 1995). As an example, Arnold and Zehnder (1991) observed crystallization and dissolution of sodium nitrate ( $\text{RH}_{\text{eq}} \approx 75.4$  at  $20^\circ\text{C}$ ) around the threshold value of 60% RH and magnesium nitrate ( $\text{RH}_{\text{eq}} \approx 54.4$  at  $20^\circ\text{C}$ ) at 50% RH. In contrast to pure salts, a salt mixture will not have a single equilibrium RH at a given temperature but a range of such humidities across which phase transitions will take place (Price and Brimblecombe, 1994). Thermodynamic models have been developed that allow the prediction of the phase behaviour of 4-component (Steiger and Zeunert, 1996) and 7-component (Price, 2000) salt mixtures as a function of RH and temperature.



**Fig. 3-1.** Equilibrium RH of some salts commonly found in buildings and temperature dependence. (1)  $\text{NaCl}$ , (2)  $\text{NaNO}_3$ , (3)  $\text{KCl}$ , (4)  $\text{KNO}_3$ , (5)  $\text{K}_2\text{SO}_4$ , (6)  $\text{MgCl}_2$ , (7)  $\text{Mg}(\text{NO}_3)_2$ , (8)  $\text{MgSO}_4$ , (9)  $\text{CaCl}_2$ , (10)  $\text{Ca}(\text{NO}_3)_2$ . From Steiger (2003).



**Fig. 3-2.** Phase diagram of the system  $\text{Na}_2\text{SO}_4\text{-H}_2\text{O}$  (Flatt, 2002). The solid lines indicate the boundaries of the stable phases. The dotted line corresponds to a solution in metastable equilibrium with respect to thenardite and supersaturated with respect to mirabilite.

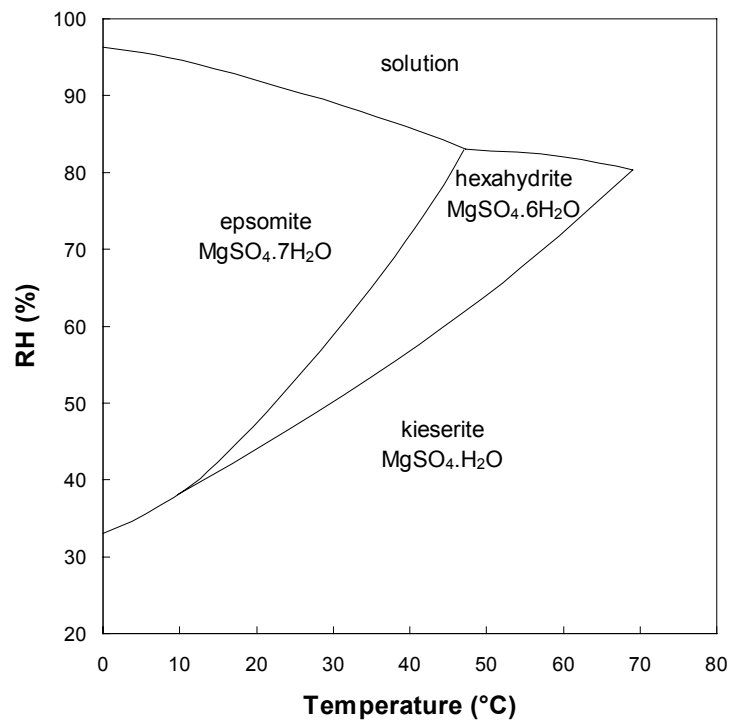


**Fig. 3-3.** Phase diagram of the system  $\text{MgSO}_4\text{-H}_2\text{O}$ , compiled after Chou and Seal (2003). These authors provide accurate constraints on the epsomite-hexahydrate transition.

## 3.2 Methods

### 3.2.1 Salt identification

Salt minerals were identified both optically with a petrographic polarizing light microscope and microchemically, according to Arnold (1984) and Bläuer Böhm (1994). This combination of optical and microchemical methods offered a very good visual control on the material that was being characterized while requiring only a minimal amount of substance. Salts that were not unambiguously identifiable with these methods (e.g. trona,  $\text{Na}_3\text{H}(\text{CO}_3)_2 \cdot 2\text{H}_2\text{O}$ , which has optical properties and chemical composition similar to thermonatrite,  $\text{Na}_2\text{CO}_3 \cdot \text{H}_2\text{O}$ ) were additionally analysed by means of X-ray diffraction with a Gandolfi camera.

### 3.2.2 Salt content of building materials

Plaster samples of the upper 2 cm including, when present, the overlying salt efflorescence, were taken from the principal salt-affected areas inside the building, crushed to grain size  $< 1$  mm with an agate mortar and pestle (soft samples) or with an electric laboratory mill (hard samples) and dried at  $40^\circ\text{C}$  until the weight was constant. Soluble salts were brought into solution by adding 100 ml deionised water to 1 g of the sample and by shaking vigorously for 2 minutes, according to the procedure described in Bläuer Böhm (1996). The obtained solutions were filtered through a membrane ( $0.45\ \mu\text{m}$  pore diameter) with the aid of a vacuum pump. The pH and the electrical conductivity of the filtrates were measured immediately afterwards. The portions of the solutions intended for cation analysis were acidified to  $\text{pH} \approx 3$  in order to avoid precipitation or adsorption of cations. The ionic composition of the solutions was analysed either with a Metrohm 690 or with a Dionex ICS-90 ion chromatograph. The analysed ions were  $\text{Na}^+$ ,  $\text{NH}_4^+$ ,  $\text{K}^+$ ,  $\text{Mg}^{2+}$ ,  $\text{Ca}^{2+}$ ,  $\text{F}^-$ ,  $\text{Cl}^-$ ,  $\text{NO}_2^-$  (Metrohm),  $\text{NO}_3^-$ ,  $\text{PO}_4^{3-}$  (Dionex) and  $\text{SO}_4^{2-}$ . These ions generally account for almost the totality of the soluble salts found in building materials. Soluble salt extraction and ion analysis were performed in duplicate for every sample.

### 3.2.3 Critical relative humidities

The equations describing the relevant phase boundaries in the  $\text{Na}_2\text{SO}_4\text{-H}_2\text{O}$  and  $\text{MgSO}_4\text{-H}_2\text{O}$  systems were obtained by fitting the corresponding curves in Fig. 3-2 and Fig. 3-3 with polynomial functions. These equations allowed the calculation of the critical RH for a specific phase transition as a function of temperature with a good accuracy in the temperature ranges of interest.

*mirabilite – thenardite*

$$RH_{mir-thn} = 0.736 T + 60.138 \quad (R^2 = 0.9995) \quad (3-30)$$

*mirabilite – solution*

$$RH_{mir-sol} = -0.0004 T^3 + 0.0076 T^2 - 0.2018 T + 97.962 \quad (R^2 = 0.9984) \quad (3-31)$$

*epsomite – hexahydrite/kieserite*

$$RH_{eps-hex} = 0.0117 T^2 + 0.518 T + 32.467 \quad (R^2 = 0.9998) \quad (3-32)$$

*epsomite – solution*

$$RH_{eps-sol} = -0.0027 T^2 - 0.1456 T + 96.056 \quad (R^2 = 0.9998) \quad (3-33)$$

Where  $T$  is the temperature (°C) and  $RH_{a-b}$  the critical RH for the phase transition  $a-b$  (%).

### 3.2.4 ECOS simulations

#### 3.2.4.1 Model

The behaviour of salt mixtures under changing climate conditions has been modelled with the ECOS code (Environmental Control of Salts, Price, 2000). ECOS is a thermodynamic model based on the Pitzer ion interaction theory for electrolyte solutions (Pitzer, 1973; 1991). Given the ionic composition of a salt mixture ( $\text{Na}^+$ ,  $\text{K}^+$ ,  $\text{Mg}^{2+}$ ,  $\text{Ca}^{2+}$ ,  $\text{Cl}^-$ ,  $\text{NO}_3^-$  and  $\text{SO}_4^{2-}$  ions), ECOS can predict the salt species and their respective amount coexisting under equilibrium conditions at any temperature and relative humidity.

The ECOS package consists of two computer programs that run under the Microsoft Windows® operating system: PHAS4, which is the user interface for inputting data into the model and for visualizing the results, and SALT, which is the application actually implementing the thermodynamic model. Because of a number of serious flaws<sup>11</sup> in PHAS4, impeding the use of ECOS in a reliable and efficient way, it was necessary to write a new front end program to the thermodynamic model. The program RUNSALT (Bionda, 2002-2005) was developed as part of this thesis as a substitute to PHAS4 and was used for all the simulations with ECOS<sup>12</sup>. The interaction of RUNSALT and SALT is illustrated in Fig. 3-4. More information on the RUNSALT program is provided in Appendix I.

---

<sup>11</sup> The experience made with PHAS4 in the course of this study was that of a general unreliability and unpredictable faulty behaviour of the program, resulting for example in program crashes and incorrect ion balance operations.

<sup>12</sup> Hereafter the designation ECOS implies the combined use of the SALT and the RUNSALT programs.

Published results from the application of ECOS are still rare; some examples can be found in Bionda and Storemyr (2002), Franzen (2002), Sawdy (2001), Sawdy and Price (2005) and Storemyr (2002).

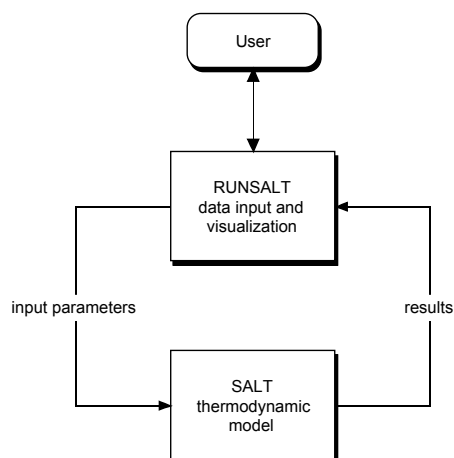


**Fig. 3-4.** Schematic representation of the software setup used for running the ECOS model.

### 3.2.4.2 Input data

ECOS requires that the ionic mixture entered be electrically neutral, i.e. the sum of positive and negative charges, taken over the cations  $\text{Na}^+$ ,  $\text{K}^+$ ,  $\text{Mg}^{2+}$ ,  $\text{Ca}^{2+}$  and the anions  $\text{Cl}^-$ ,  $\text{NO}_3^-$  and  $\text{SO}_4^{2-}$ , should be equal. Carbonate species are not considered and are thus excluded from the charge balance. Moreover, the model cannot handle simultaneously  $\text{Ca}^{2+}$  and  $\text{SO}_4^{2-}$ .

Due to the restrictions imposed by ECOS on the input data, it is generally not possible to directly enter ionic compositions as obtained from laboratory analyses. In fact, aqueous extracts from porous building materials like mortars and natural stones usually contain a significant amount of carbonate ( $\text{CO}_3^{2-}$ ) and bicarbonate ( $\text{HCO}_3^-$ ), in relative amounts depending on the pH of the solution. A charge balance performed solely on the basis of the abovementioned ions will usually result in an excess of cations. Because of the sparing solubility of gypsum, the solutions will also typically contain both calcium and sulphate ions. Calcium and magnesium carbonates, as well as gypsum, have such a low solubility compared with the other salt minerals of interest that they actually constitute a chemical divide (Hardie and Eugster, 1970). The evaporation of water from solutions containing  $\text{Ca}^{2+}$ ,  $\text{Mg}^{2+}$ ,  $\text{SO}_4^{2-}$  and carbonate leads invariably to the crystallization of carbonate minerals like calcite and nesquehonite, followed by gypsum if  $\text{Ca}^{2+}$  has not been completely consumed.

The ionic analyses carried out according to section 3.2.2 provided the data for the calculations with ECOS. In view of the abovementioned low solubility of gypsum, calcium and magnesium carbonates, and because they cannot be handled by ECOS, these species were effectively removed from the system by the following procedure:

- 1) Calculation of the charge imbalance *diff*. This imbalance was assumed to be mostly attributable to carbonate species (Steiger et al., 1998).
- 2) Removal of calcium carbonate (elimination of equal mole amounts of  $\text{Ca}^{2+}$  and *diff*): the ion of lesser concentration was set to zero, while the ion of higher concentration was set to the difference in the two concentrations.
- 3) Removal of magnesium carbonate (elimination of equal mole amounts of  $\text{Mg}^{2+}$  and *diff*) as in 2) if there was still some *diff* left.
- 4) Removal of gypsum<sup>13</sup> (elimination of equal mole amounts of  $\text{Ca}^{2+}$  and  $\text{SO}_4^{2-}$ ) as in 2) if there was still some  $\text{Ca}^{2+}$  left.

### 3.2.5 Mineral saturation indexes

The saturation index *SI* is defined as

$$SI = \log\left(\frac{IAP}{K}\right)$$

where *IAP* is the ion activity product and *K* is the solubility product constant. The saturation index indicates the thermodynamic tendency of a particular mineral to precipitate or dissolve in a given solution. For *SI*=0 (*IAP*=*K*) there is equilibrium between mineral and solution, *SI*<0 (*IAP*<*K*) indicates undersaturation (i.e. the mineral is likely to dissolve) and *SI*>0 (*IAP*>*K*) supersaturation (i.e. the mineral is likely to precipitate).

Mineral saturation indexes in the pore system of building materials were computed using the PHREEQC 2.12 hydrogeochemical code (Parkhurst and Appelo, 1999). The calculations were carried out using the thermodynamic databases *wateq4f.dat* (solutions of low ionic strength) and *pitzer.dat* (solutions of high ionic strength). *wateq4f.dat* is consistent with the aqueous model WATEQ4F (Ball and Nordstrom, 1991). When using this database, PHREEQC applies a ion association model and Debye Hückel expressions to calculate activity coefficients. This approach is supposed to be adequate for electrolyte solutions with ionic strength up to seawater (i.e. about 0.7, see e.g. Appelo and Postma, 2005) but might yield inaccurate results at higher ionic strengths (Parkhurst and Appelo, 1999). An implementation of the Pitzer ion interaction formulation (Pitzer, 1973; 1991) based on the PHRQPITZ code (Plummer et al., 1988) is available since PHREEQC version 2.12. The model is invoked by using the *pitzer.dat* thermodynamic database, which is less complete than *wateq4f.dat* (e.g. thenardite and parameter values for  $\text{NO}_3^-$ , are missing).

---

<sup>13</sup> Gypsum removal is also implemented in RUNSALT and can thus alternatively be performed after data input.

### 3.3 Results

#### 3.3.1 Salt species and distribution on surfaces

The salt-affected areas and their distribution were identified and mapped in detail along with the different types of damage encountered (Fig. 1-4 and Fig. 1-5). The majority of the salt-affected areas was concentrated on the lower part of the walls, from a few centimetres above the floor to about 1 meter height, in the zone of rising damp. At higher levels, salts were restricted to a few isolated spots. On the basis of the observations made, wall paintings and stuccoes, which are placed at an height of ca. 1 m and above (Fig. 1-3), didn't seem to be affected by salt deterioration.

Salts were sampled periodically from all the principal efflorescence zones and analysed in the laboratory. Sampling locations and identified salts are indicated in Fig. 3-6 to Fig. 3-9 and Table 3-2. The predominant salt species identified were mirabilite ( $\text{Na}_2\text{SO}_4 \cdot 10\text{H}_2\text{O}$ ), thenardite ( $\text{Na}_2\text{SO}_4$ ), epsomite ( $\text{MgSO}_4 \cdot 7\text{H}_2\text{O}$ ), trona ( $\text{Na}_3\text{H}(\text{CO}_3)_2 \cdot 2\text{H}_2\text{O}$ ) and, to a lesser extent, niter ( $\text{KNO}_3$ ). Mirabilite, thenardite, epsomite and trona were recognized as being responsible for most of the observable damage (Fig. 3-5). Other salts identified include natron ( $\text{Na}_2\text{CO}_3 \cdot 10\text{H}_2\text{O}$ , one location), aphthitalite ( $\text{K}_3\text{Na}(\text{SO}_4)_2$ , one location) and gypsum ( $\text{CaSO}_4 \cdot 2\text{H}_2\text{O}$ ), which was present as accessory in many samples.

The sodium salts mirabilite, thenardite and trona were associated with the youngest cement plasters from the early seventies of the last century, which are coated with emulsion paint. Alkali carbonate and sulphate salts are known to commonly originate from alkaline building materials, in particular from mortars containing Portland cement (see e.g. Arnold and Zehnder, 1991). Mirabilite/thenardite salts were mostly localized in the lowest part of the walls, up to a height of about 50 cm from the floor. On the whole, this area was also the most deteriorated. Trona efflorescence was particularly concentrated in the NW wall, near the corner with the SW wall. In several instances, both mirabilite/thenardite and trona grew within the mortar, below paint layer and plaster surface, occasionally leading to the complete detachment of the plaster surface. In the case of mirabilite/thenardite, the detachment extended deeper into the plaster (Fig. 3-5a-b), up to ca. 1-2 cm, whereas in the case of trona it was mainly limited to the upper 0.5 cm (Fig. 3-5e-f).

Epsomite was present on both cement plasters (main walls) and lime plasters (chancel, two central apses and upper part of the church above the cornice). The locations in the upper part of the church (81, 82, 84 and 88), about 7-9 m from floor level, are assumed to be out of reach of rising damp. Physical evidence collected in situ points to water infiltration from the roof as the main cause of salt mobilization and transport. Epsomite formed crusts or efflorescences on the surface of the plaster immediately below the paint layer (Fig. 3-5c-d). The deterioration process lead partly to flaking and loss of the paint layer. In few cases, a moderate flaking of

the plaster surface was observed. Compared to sodium sulphate, the generated damage was less important and more superficial.

Niter efflorescence was localized in two zones on the NW and SW walls, at a higher level (up to about 170 cm above the floor) than sulphates in the zone of rising damp. The higher crystallization height is most likely the consequence of the slightly better solubility of niter; according to the model of salt transport and selective precipitation in the zone of rising damp (Arnold and Zehnder, 1984), the salt can reach higher wall levels by capillary rising in solution. Niter was present in form of fluffy efflorescence growing on the surface of the plaster, in places where the paint layer was missing. There was no observable evidence of damage caused by efflorescence of this salt.

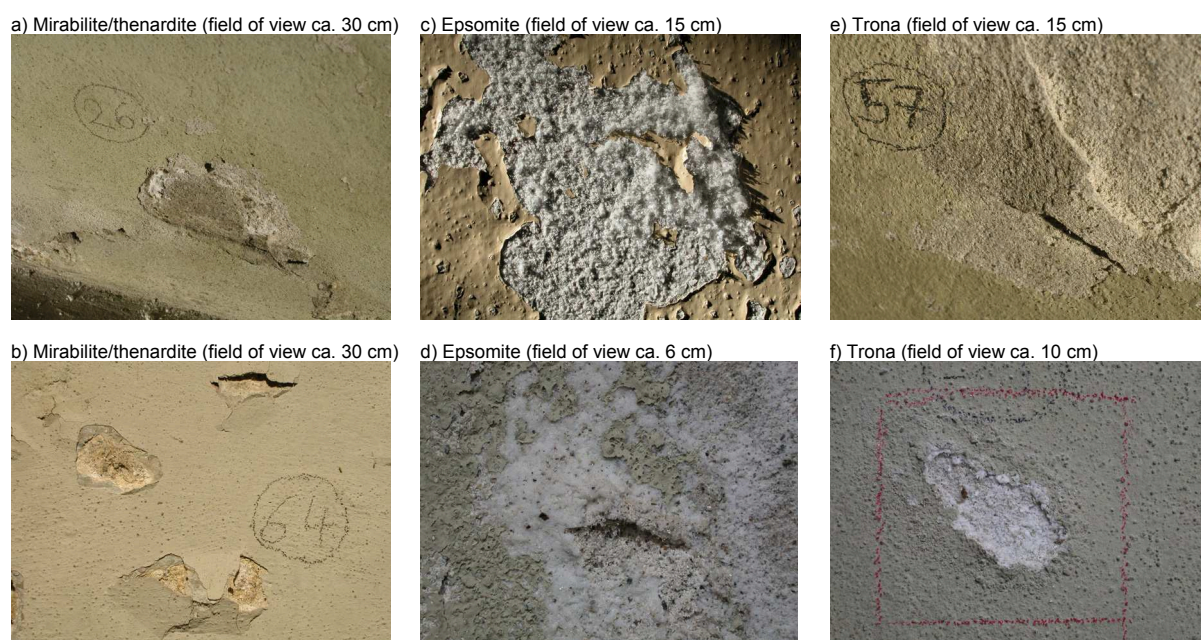


**Fig. 3-5.** Principal salts and examples of weathering features observed. a) Location 26, mirabilite/thenardite crystallisation: sanding and crumbling of plaster. b) Location 64, mirabilite/thenardite crystallisation and accumulation at shallow depth: blistering of plaster. c) Location 2 (sacristy), epsomite whiskers: flaking of the paint layer. d) Location 5, epsomite crust: flaking of paint layer and plaster surface. e) Location 57, trona crystallisation and accumulation at shallow depth: blistering of plaster. f) Location 31, trona bristly efflorescence: loss of plaster surface.



**Table 3-2.** Sampling locations and observed major X and accessory (X) salt species.

side	location	mirabilite	thenardite	epsomite	trona	niter	natron	aphthitalite	gypsum	calcite
NE (Fig. 3-6)	1			X		(X)				
	2 (sacristy)			X						
	27			X					(X)	
	28			X					(X)	
	62				X					
	66			(X)					X	
	71		X		X					
SW (Fig. 3-7)	14								X	
	20			X		X				
	21			X					(X)	
	22					X			(X)	
	32					X				
	59			X						
	60								(X)	X
	65			X						
NW (Fig. 3-8)	3	X	X			X	X			
	4	(X)		X	(X)	(X)			(X)	
	13					X				
	23	X								
	29				X			X		
	30	X	X		X					
	31				X					
	34				X					
	38									X
	53									X
	56				X					
	57				X					
	58				X					
	81			X						
	82			X						
	88			X						
SE (Fig. 3-9)	5			X						
	6		X		X	(X)				
	15	X	X			(X)				
	24			X					(X)	
	25	X	X						(X)	
	26	X	X							
	33	X			X					
	35								X	
	37			X					(X)	
	61		X							
	63			X						
	64		X							
	84			X						



**Fig. 3-6.** Sampling locations on the NE side and identified salt species.



**Fig. 3-7.** Sampling locations on the SW side and identified salt species.

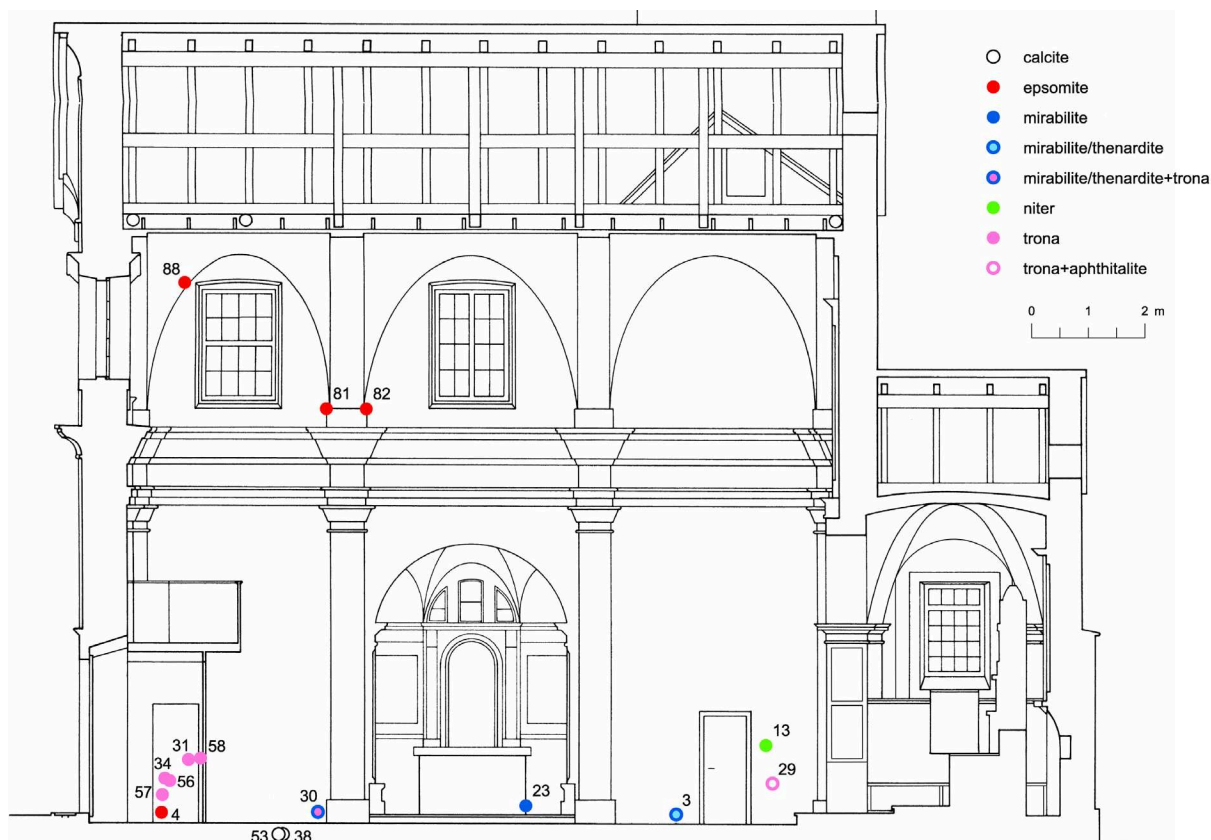


**Fig. 3-8.** Sampling locations on the NW side and identified salt species.

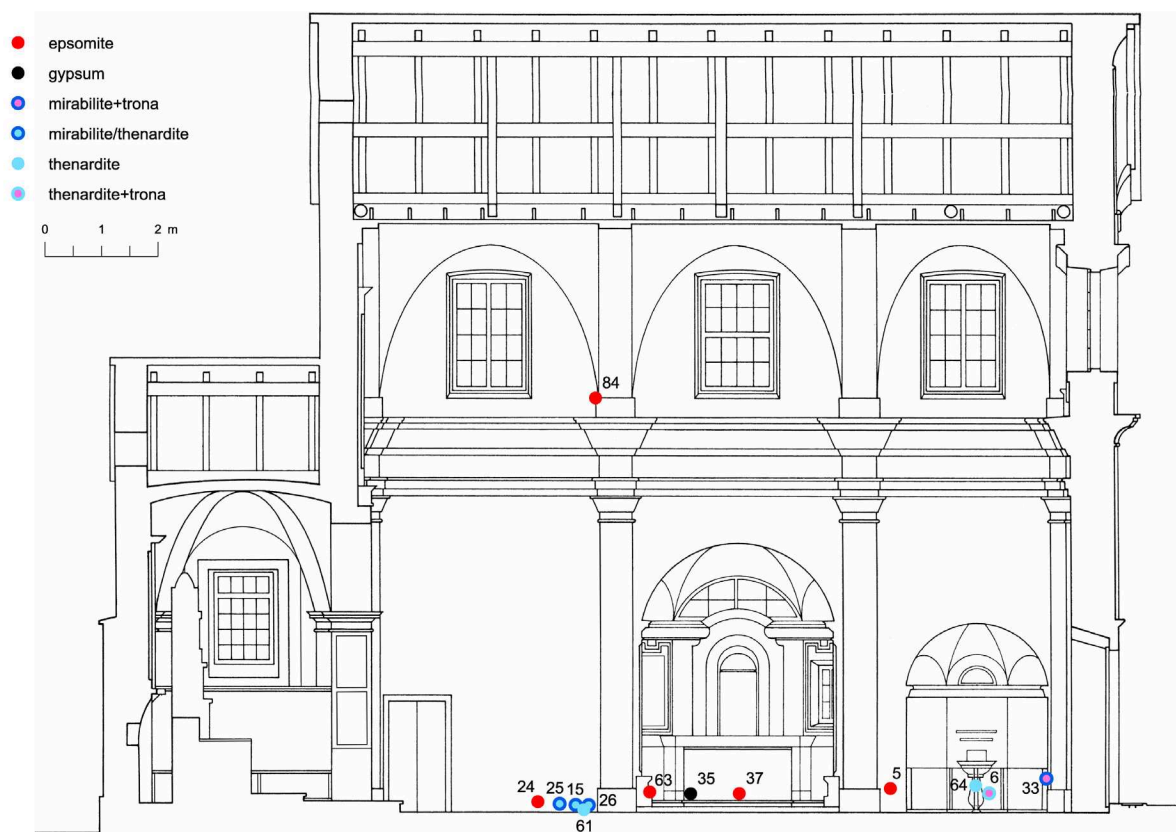


**Fig. 3-9.** Sampling locations on the SE side and identified salt species.

### 3.3.2 Salt behaviour in relation to indoor climate

Salt-affected areas were periodically surveyed, documented and sampled over a period of two years as shown in Fig. 3-10. The only salt activity observed was the phase transition between mirabilite and thenardite in efflorescences. Epsomite, trona and niter were stable throughout the whole monitoring period.

The observed salt behaviour was compared with the critical relative humidities, which define the theoretical phase transitions for a pure salt. These were calculated on the basis of the recorded temperature for all the observed salts (see equations in section 3.2.3) with exception of trona, which is known to be stable under most environmental conditions (see e.g. Gmelin, 1939). In the present case  $RH_{mir-thn}$  lies approximately within the range 60-80% and  $RH_{eps-hex}$  within 35-55%, while the relative humidity for the deliquescence of mirabilite, epsomite and niter lies above 90%.

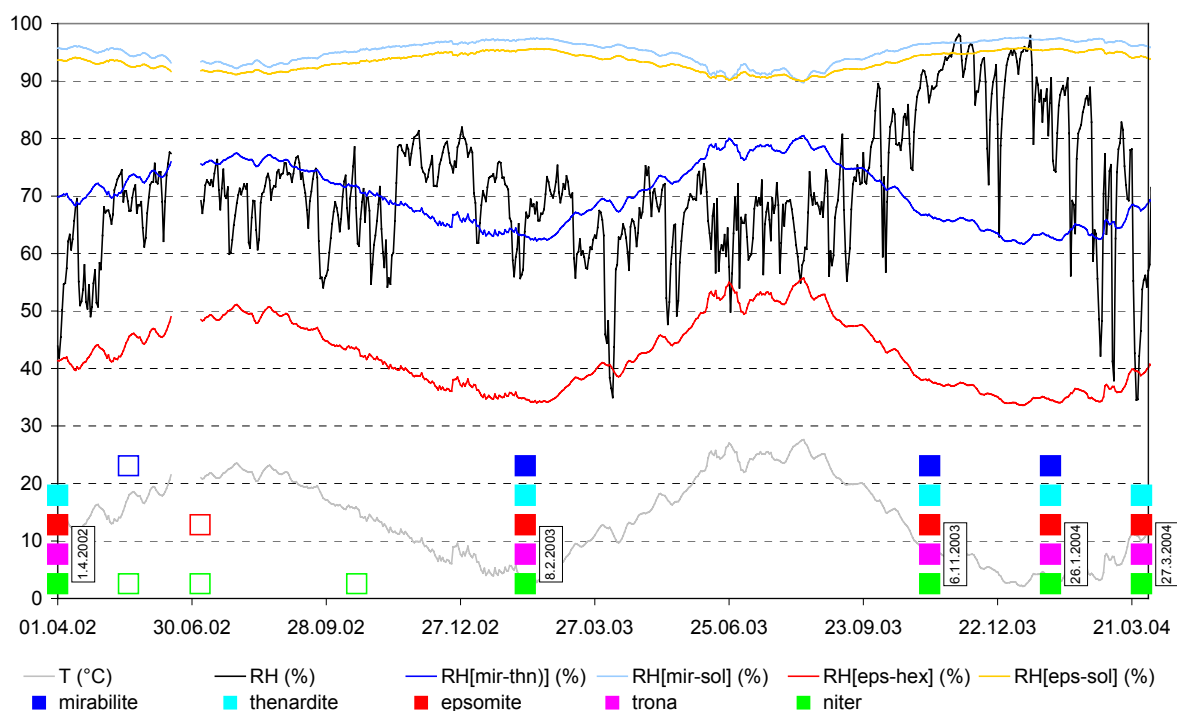


**Fig. 3-10.** Principal salt species observed during in situ investigation (coloured squares; open squares indicate incomplete sampling, i.e. not all monitored locations were sampled), recorded indoor climate (T and RH, daily mean values) and calculated critical RH for the relevant phase transitions in the  $\text{Na}_2\text{SO}_4\text{-H}_2\text{O}$  and  $\text{MgSO}_4\text{-H}_2\text{O}$  systems (see equations in section 3.2.3). Niter has a deliquescence RH approximately in the same range as mirabilite and epsomite; trona is known to be stable under most environmental conditions (see e.g. Gmelin, 1939). Climate measurements for the period 17.6.-5.7.2002 are missing due to a failure of the measuring equipment.

The observed salt behaviour generally correlates well with the calculated critical relative humidities. The climate in the church was almost permanently within a range where epsomite and niter are supposed to be stable and where phase transitions between mirabilite and thenardite are to be expected.

The observed behaviour of mirabilite and thenardite for  $RH \approx RH_{mir-thn}$  (8.2.2003),  $RH > RH_{mir-thn}$  (26.1.2004) and  $RH < RH_{mir-thn}$  (27.3.2004) is summarized in Table 3-3. When the RH of the air was clearly below  $RH_{mir-thn}$ , no mirabilite could be found (1.4.2002 and 27.3.2004). In all other situations, both mirabilite and thenardite were present. Thenardite was found even in the case of persistence of indoor air RH well above  $RH_{mir-thn}$  (up to 3-4 months, see salt sampling of 26.1.2004) where, according to the phase diagram of the  $Na_2SO_4-H_2O$  system (Fig. 3-2), mirabilite would be the stable phase.

**Table 3-3.** Typical salt behaviour and dynamics of the sodium sulphate salts, as observed in the church San Pietro Martire. Indicated are salt species, as determined in the laboratory and, in square brackets, the type of efflorescence observed in situ.

location	8.2.2003 (RH = ~65%, T = ~5 °C)	26.1.2004 (RH = ~85%, T = ~5 °C)	27.3.2004 (RH = ~45%, T = ~10 °C)
3	mirabilite and thenardite [friable crust]	mirabilite [friable crust]	thenardite [powder]
15	mirabilite [whiskers]	mirabilite [whiskers]	thenardite [powder]
25	mirabilite and minor thenardite [whiskers] (Fig. 3-11)	mirabilite [whiskers]	thenardite [powder]
26	thenardite [powder] (Fig. 3-12)	mirabilite and thenardite [friable crust]	thenardite [powder]
30	mirabilite and trona [whiskers]	mirabilite and trona [whiskers]	thenardite and trona [powder]

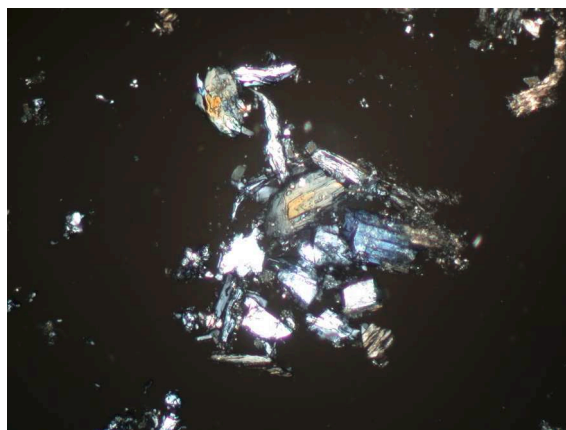
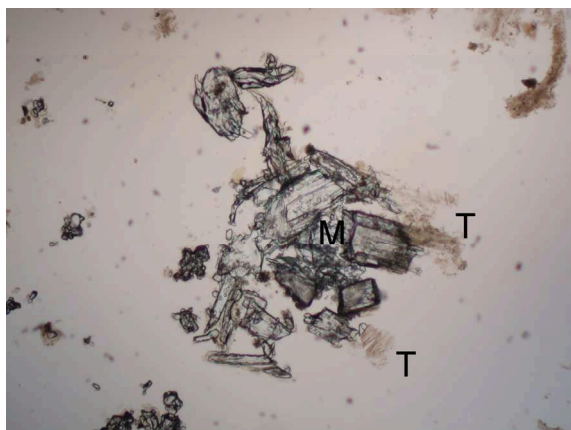


**Fig. 3-11.** Photomicrograph of mirabilite (M, crystals with high negative relief) showing an initial dehydration to thenardite (T, submicroscopical crystals with low negative relief that pseudomorphically replace mirabilite). Sample collected on the 8.2.2003 from location 25. Left: plane polarized light. Right: cross polarized light. Field of view is 2.5 mm

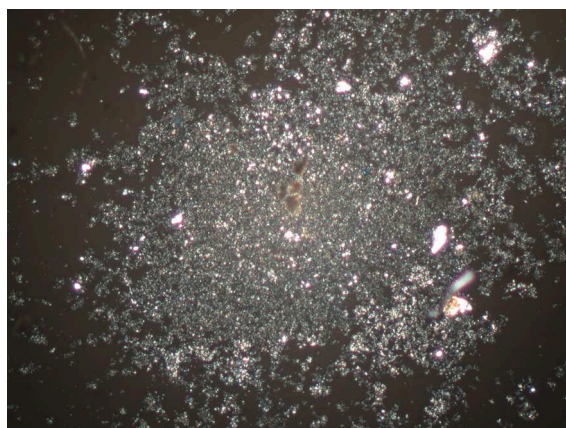
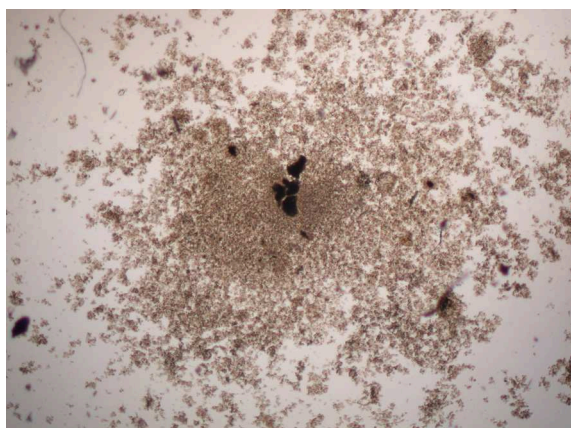


**Fig. 3-12.** Photomicrograph of thenardite. Crystal morphology and dimension are similar to crystals precipitated directly from solution as reported by Rodriguez-Navarro et al. (2000). This seems to suggest that the crystals formed either by direct precipitation at low RH or by recrystallization (due to exposure to increasing humidity) of thenardite that was originally produced by mirabilite dehydration (phase T in Fig. 3-11). Sample collected on the 8.2.2003 from location 26. Left: plane polarized light. Right: cross polarized light. Field of view is 2 mm.



### 3.3.3 Soluble salts in building materials

Plaster samples were collected twice (25.4.2003 and 26.1.2004) from the locations 1, 3, 4, 5, 15, 24, 25, 26, 27, 30 and once from locations 66 (26.1.2004) and 81 (26.3.2004), see Fig. 3-6 to Fig. 3-9. On all these plasters salt efflorescence as described in section 3.3.1 was observed. The average mineralogical compositions (XRD) of samples 1, 3, 4, 5, 15, 24, 25, 26, 27, 30 is 39% quartz, 30% calcite, 22% feldspar, 8% mica and less than 1% dolomite (diffractograms and results of the quantitative determination of the detectable phases are in Appendix F). The unhydrated cement minerals alite ( $C_3S$ ) and belite ( $C_2S$ ), were detected by optical microscopy in most samples.

The ionic composition of the aqueous extracts of the plasters is given in Table 3-4. Results are additionally displayed in a modified Piper diagram (Piper, 1944), which depicts the ionic composition of the soluble salts in the plasters and its relationship to the efflorescence observed on the surface (Fig. 3-13). The variation of the ionic composition between the samples collected on the 25.4.2003 and the samples collected 26.1.2004 is evidenced in Fig. 3-14.

**Table 3-4.** Ionic composition of aqueous extracts ( $\text{meq kg}^{-1}$  dry sample). Sample X-1 means location X, sampling day 25.4.2003; sample X-2 means location X, sampling day 26.1.2004. Sample 66 was collected on the 26.1.2004, sample 81 on the 26.3.2004.

sample	$\text{Na}^+$	$\text{K}^+$	$\text{Mg}^{2+}$	$\text{Ca}^{2+}$	$\text{Cl}^-$	$\text{NO}_3^-$	$\text{SO}_4^{2-}$
1-1	42.4	19.5	43.6	212.9	46.7	126.1	126.0
1-2	19.8	12.3	57.6	89.3	16.4	43.0	82.4
3-1	148.0	45.1	17.9	33.7	17.8	81.8	71.6
3-2	51.1	38.7	26.5	50.7	13.9	47.2	49.8
4-1	22.8	5.4	40.2	34.1	0.0	22.7	44.3
4-2	14.1	2.4	1.3	267.0	41.4	107.1	42.2
5-1	48.2	39.8	78.5	63.5	8.8	26.1	174.9
5-2	43.7	23.9	125.1	108.4	6.2	21.1	237.4
15-1	166.3	74.1	52.3	26.7	79.3	60.5	115.1
15-2	37.1	18.1	59.4	30.5	19.9	8.3	23.9
24-1	58.8	25.5	187.9	111.1	123.7	92.6	161.1
24-2	68.9	28.1	188.5	142.6	119.0	103.1	151.1
25-1	76.3	39.9	31.6	21.9	47.4	20.5	42.6
25-2	97.2	97.2	82.3	32.6	31.7	17.7	147.4
26-1	124.6	76.2	14.8	165.3	40.3	38.2	284.3
26-2	411.4	244.1	17.6	175.5	97.0	66.7	606.3
27-1	22.7	10.4	30.6	61.7	16.6	45.8	51.4
27-2	13.1	7.2	104.8	150.5	20.0	49.6	149.7
30-1	41.1	15.8	2.8	60.8	1.1	18.4	26.2
30-2	25.7	12.4	5.1	71.8	3.6	23.2	33.6
66	24.5	14.2	217.5	480.0	32.2	189.7	411.1
81	14.4	12.7	231.7	1211.4	11.4	107.1	1295.5

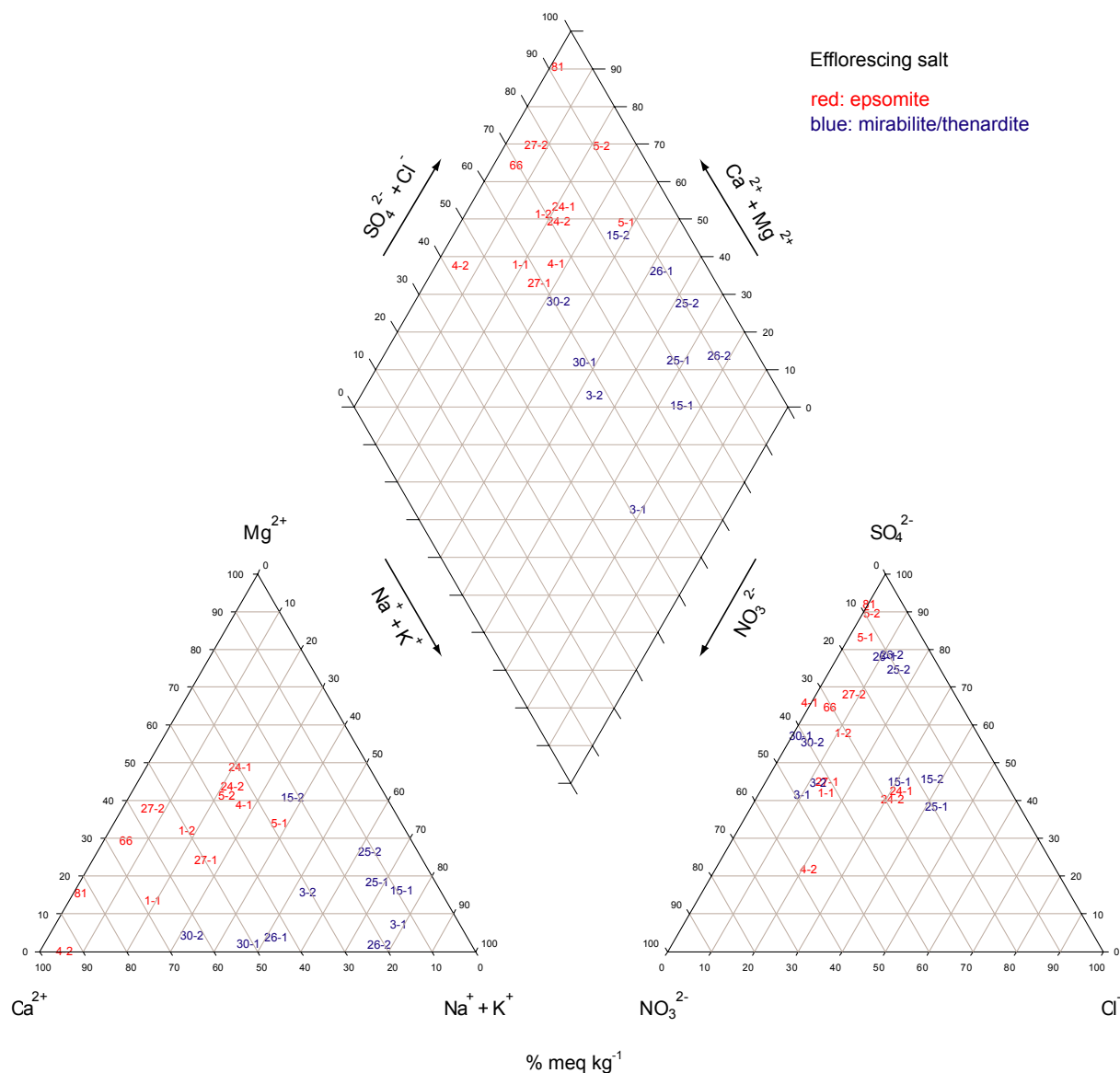


**Fig. 3-13.** Modified Piper diagram (Piper, 1944) showing the relationship between ionic composition of the soluble salts in the mortars (% meq kg<sup>-1</sup> dry sample) and mineralogy of the observed salt efflorescence. Cations are plotted in the left ternary diagram, anions in the right ternary diagram. The diamond-shaped plotting field represents a projection of the two ternary diagrams into a common area, where the ionic composition of a given sample can be represented by a single point. Sample X-1 means location X, sampling day 25.4.2003; sample X-2 means location X, sampling day 26.1.2004.

From Fig. 3-13 it is possible to recognize that aqueous extracts from mortars with efflorescence of epsomite and mirabilite/thenardite form distinct compositional clusters. Mirabilite and/or thenardite are efflorescing on plasters having a soluble salt content with a molar equivalent ratio Na/Mg > ~1 and epsomite for Na/Mg < ~1 (compare Fig. 3-14).



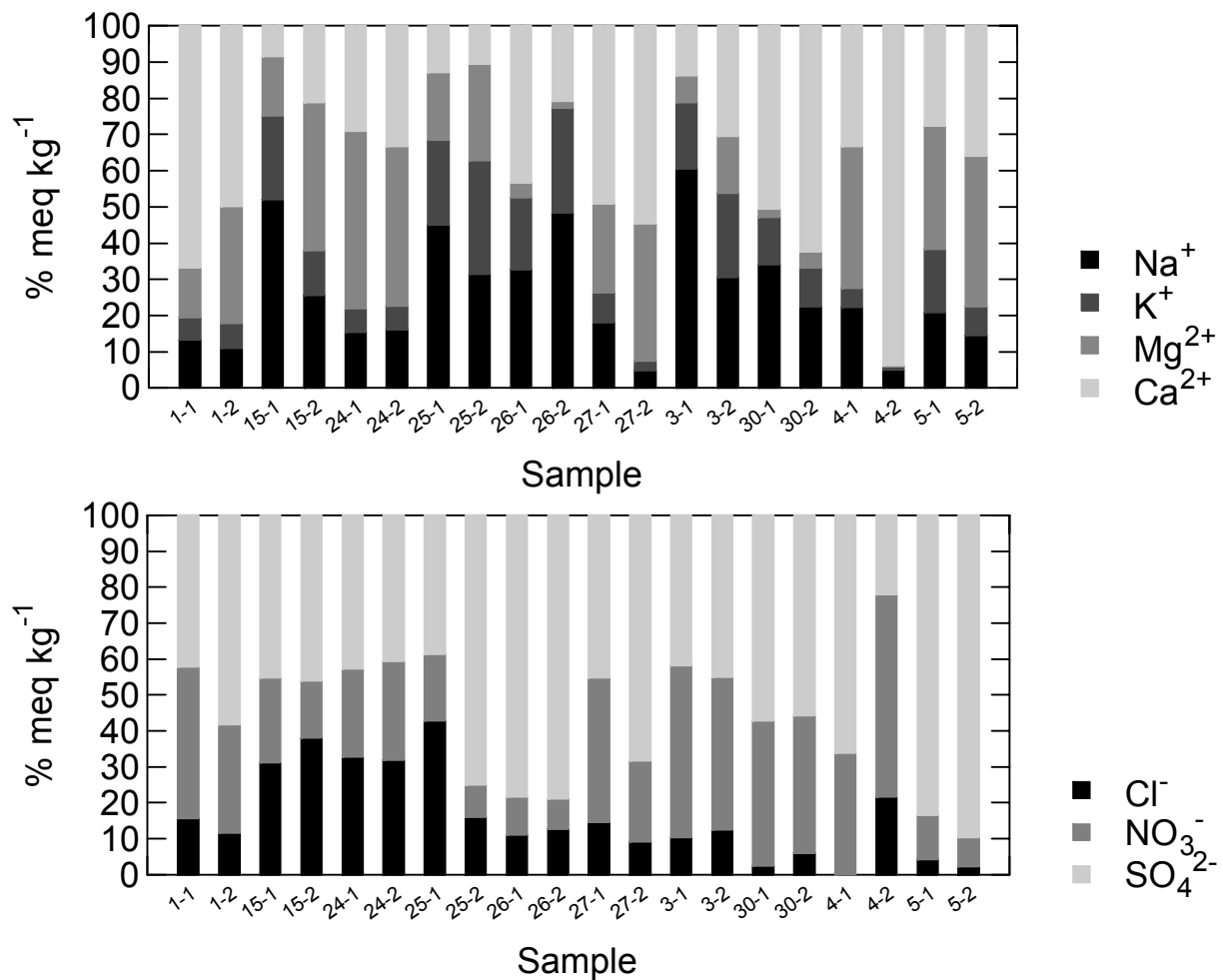


**Fig. 3-14.** Comparison of the ionic composition (% meq kg<sup>-1</sup> dry sample) of aqueous extracts from plasters sampled in two different periods. Sample X-1 means location X, sampling day 25.4.2003; sample X-2 means location X, sampling day 26.1.2004.

Plaster samples collected in two different periods from the same location show partly large variations in the composition especially in the case of extractable cations. These differences are less pronounced for the anions. There is however no recognisable pattern, i.e. it is not possible to discriminate between a temporal variation in the composition and the variation due to the heterogeneous distribution of the salts within the plaster.

### 3.3.4 ECOS simulations

Simulations with ECOS were performed for plasters showing salt efflorescence, a prerequisite for verifying the results of modelling. Modelling was carried out for plasters on which the major efflorescing salts were mirabilite/thenardite (locations 3, 15, 25, 26, 30) or epsomite (location 27). Simulations for trona efflorescence were not possible because carbonates are not handled by ECOS. Plasters with niter as principal efflorescence could not be considered because of the lack of analytical data (sampling not allowed at those locations).

The ionic composition ( $\text{Na}^+$ ,  $\text{K}^+$ ,  $\text{Mg}^{2+}$ ,  $\text{Ca}^{2+}$ ,  $\text{Cl}^-$ ,  $\text{NO}_3^-$  and  $\text{SO}_4^{2-}$  ions, see section 3.3.3) of the aqueous extracts of plasters samples collected on the 26.1.2004 was used as input data. The corresponding analytical data as input into the model is presented in Table 3-5.

**Table 3-5.** Ionic compositions as input into ECOS ( $\text{mmol kg}^{-1}$  dry sample) and observed efflorescing salts.  $\text{Mg}^{2+}$ ,  $\text{Ca}^{2+}$  and  $\text{SO}_4^{2-}$  have been corrected by removing  $\text{CaCO}_3$ ,  $\text{MgCO}_3$  and  $\text{CaSO}_4$  from the system as explained in section 3.2.4.2.

Sample	$\text{Na}^+$	$\text{K}^+$	$\text{Mg}^{2+}$ (corrected)	$\text{Ca}^{2+}$ (corrected)	$\text{Cl}^-$	$\text{NO}_3^-$	$\text{SO}_4^{2-}$ (corrected)	Charge imbalance	Observed efflorescing salt
3-2	51.1	38.7	10.7	0.0	13.9	47.2	24.9	0.3	mirabilite/thenardite
15-2	37.1	18.1	0.0	0.0	19.9	8.3	12.0	3.0	mirabilite/thenardite
25-2	97.2	97.2	1.3	0.0	31.7	17.7	73.7	0.2	mirabilite/thenardite
26-2	411.4	244.1	8.8	0.0	97.0	66.7	254.6	0.2	mirabilite/thenardite
30-2	25.7	12.4	2.5	0.0	3.6	23.2	7.9	0.5	mirabilite/thenardite
27-2	13.1	7.2	52.4	0.0	20.0	49.6	27.3	0.9	epsomite

The results of the simulations for  $T=5\text{ }^\circ\text{C}$ ,  $\text{RH}=85\%$  and for  $T=10\text{ }^\circ\text{C}$ ,  $\text{RH}=45\%$ , which correspond to the climatic conditions (mean daily values) of the 26.1.2004 and 27.3.2004, were compared with the salt efflorescences observed on the same days. During the period between the 26.1.2004 and the 27.3.2004, a marked change in the indoor climate was recorded. A drop in the relative humidity of about 40% allowed to reach the critical relative humidity for the transition mirabilite/thenardite as calculated for a pure salt system. As noted in section 3.3.2, this climatic change triggered a phase transition from mirabilite to thenardite in the monitored efflorescences (Table 3-3). It was therefore of particular interest to compare the predictions of ECOS with this observation. Simulations performed for plasters collected on the 25.4.2003 provided comparable results (see Appendix H).

The results of the simulations are presented in form of cumulative plots (Fig. 3-15 to Fig. 3-20). The lines indicate the cumulative volume of solid salt minerals in the mixture against the RH and at the given temperature. The exact volume of a particular salt at a specific RH is indicated by the distance between the corresponding line and the line beneath. For example, in Fig. 3-16 at  $T=5\text{ }^\circ\text{C}$  and  $\text{RH}=80\%$ , mirabilite and apththalite are present in a volume ratio of

4:1; mirabilite exists in the solid state between 68% and 95% RH; above 95% RH all salts are solution. The results given in Fig. 3-15 to Fig. 3-20 are summarised in Table 3-6.

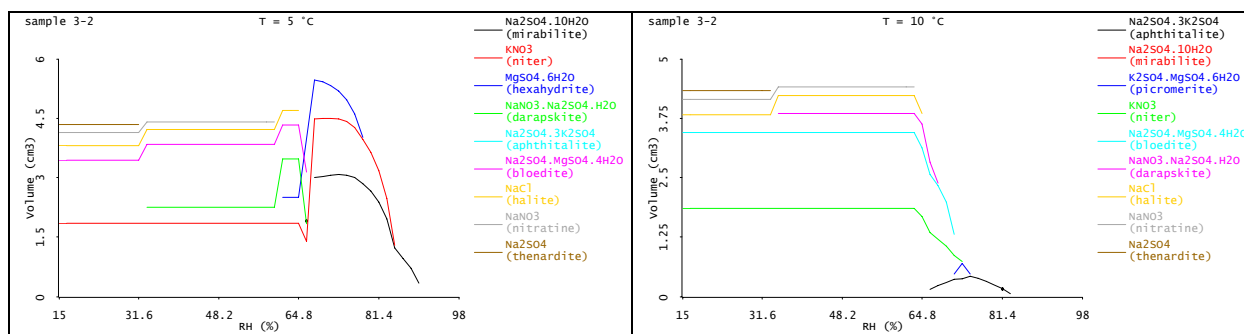


**Fig. 3-15.** ECOS crystallisation sequences at 5 and 10 °C for soluble salts extracted from plaster at location 3.

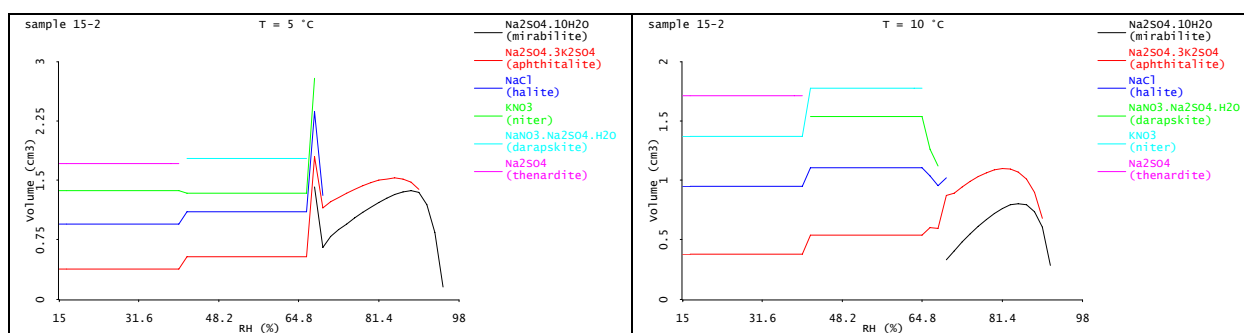


**Fig. 3-16.** ECOS crystallisation sequences at 5 and 10 °C for soluble salts extracted from plaster at location 15.

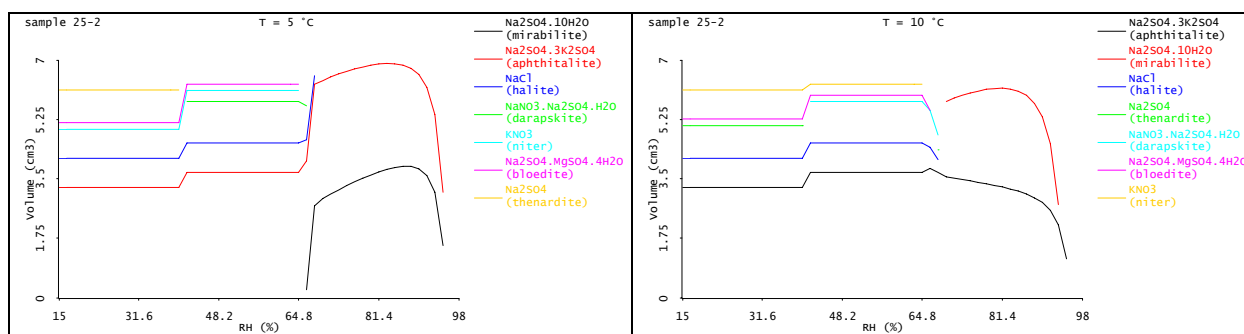


**Fig. 3-17.** ECOS crystallisation sequences at 5 and 10 °C for soluble salts extracted from plaster at location 25.

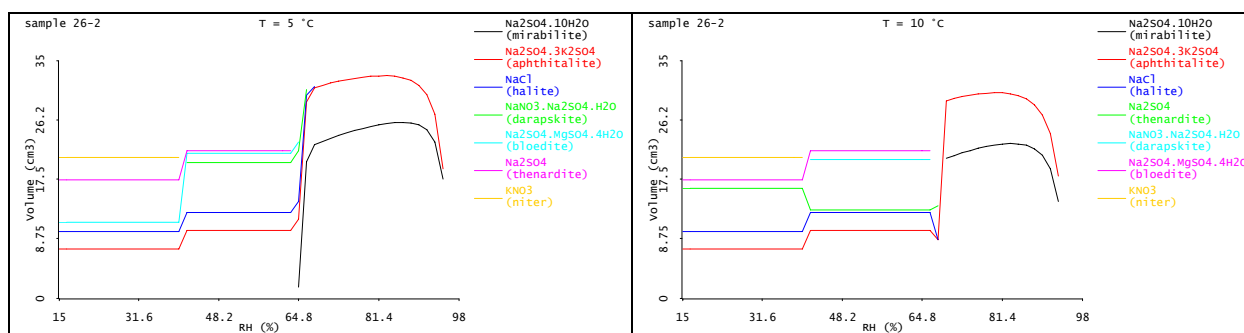


**Fig. 3-18.** ECOS crystallisation sequences at 5 and 10 °C for soluble salts extracted from plaster at location 26.

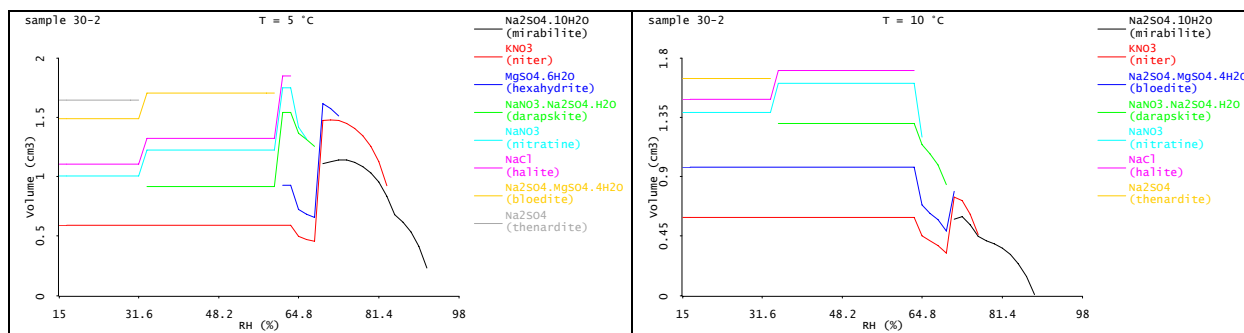


**Fig. 3-19.** ECOS crystallisation sequences at 5 and 10 °C for soluble salts extracted from plaster at location 30.

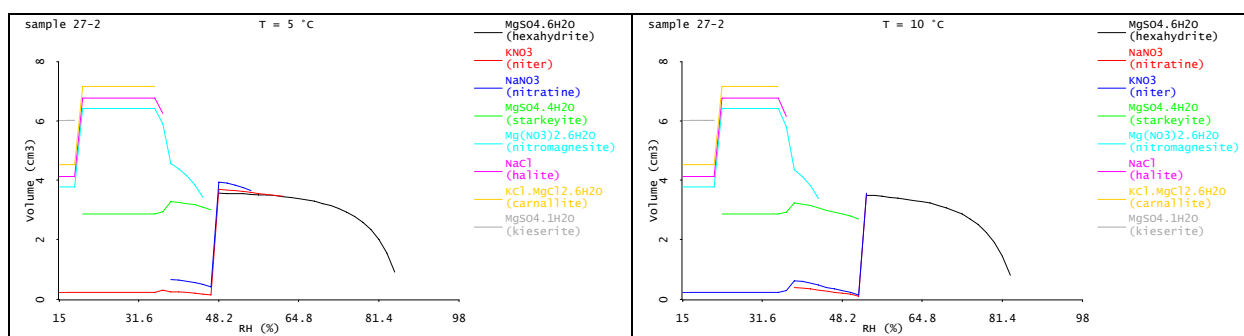


**Fig. 3-20.** ECOS crystallisation sequences at 5 and 10 °C for soluble salts extracted from plaster at location 27.

**Table 3-6.** Comparison of ECOS model predictions with observations.

sample	T=5 °C, RH=85%		T=10 °C, RH=45%	
	model	observation (26.1.2004)	model	observation (27.3.2004)
3-2	mirabilite	mirabilite	various salts thenardite only for RH<33%	thenardite
15-2	mirabilite and aphthitalite	mirabilite	various salts thenardite only for RH<40%	thenardite
25-2	mirabilite and aphthitalite	mirabilite	various salts thenardite only for RH<40%	thenardite
26-2	mirabilite and aphthitalite	mirabilite and thenardite	various salts and less thenardite	thenardite
30-2	mirabilite	mirabilite and trona	various salts thenardite only for RH<33%	thenardite and trona
27-2	all salts in solution	epsomite	starkeyite, niter and nitratine	epsomite

For locations 3, 15, 25, 26 and 30, at  $T=5\text{ }^{\circ}\text{C}$  and for  $\text{RH}=85\%$  ECOS predicts the occurrence of mirabilite, which was in fact the salt detected on the plasters under these environmental conditions. For three out of five samples (15-2, 25-2 and 26-2), ECOS additionally predicted the occurrence of aphthitalite, which however was not found. According to the output of the model, at  $T=10\text{ }^{\circ}\text{C}$  and for  $\text{RH}=45\%$  various salts should occur, which in fact were not observed. At this temperature, ECOS foresees the crystallization of thenardite starting at  $\text{RH}<33\text{-}40\%$  with exception of sample 26-2, where a very small amount of thenardite was also present at  $\text{RH}=45\%$ . Thenardite was however observed efflorescing at an  $\text{RH}$  of  $45\%$ . Over the humidity range considered for the simulations ( $15\text{-}98\%$ ), ECOS predicted additional salts that, with exception of niter, were never observed on the investigated plasters. Efflorescence of epsomite persisted during the whole monitoring period. However, epsomite never appears in the results of ECOS. Instead, generally the crystallization of hexahydrate is predicted (Fig. 3-20). This has been noticed for different samples and environmental conditions tested in the course of the present study. As reported in Bionda (2004), the computation of the phase transitions in the  $\text{MgSO}_4\text{-H}_2\text{O}$  system performed by ECOS are in disagreement with the experimental data. As an example, the relative humidity calculated by ECOS for the transition between epsomite and hexahydrate at  $20^{\circ}\text{C}$  is about  $82\%$ , which is well above published data of  $43\text{-}45\%$  (Gmelin, 1939) or  $47.5\%$  (Chou and Seal, 2003). In comparison with experimental data, the phase boundaries computed by ECOS for the pure  $\text{MgSO}_4\text{-H}_2\text{O}$  system are clearly shifted towards higher relative humidities (Fig. 3-21). In other words, ECOS predicts the formation of epsomite only at high relative humidity. This results in a narrow epsomite stability field, which explains why the presence of this salt is mostly not predicted by ECOS, although epsomite is the stable phase under the environmental conditions found in the investigated building.

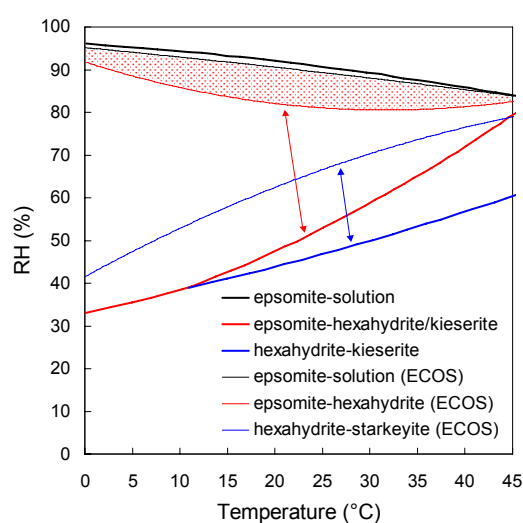


**Fig. 3-21.** Phase boundaries in the  $\text{MgSO}_4\text{-H}_2\text{O}$  system: comparison of ECOS predictions (thin lines) with experimental data (Chou and Seal, 2003) (thick lines). Note the shift towards higher relative humidities of the phase boundaries calculated by ECOS, resulting in a narrow epsomite stability field (stippled area).

### 3.3.5 Saturation state of pore solutions

Saturation indexes of the relevant soluble salt species were determined for salt-affected plasters in the case that these are impregnated with water. This was achieved in the following way:

- 1) Determination of the soluble salt content (aqueous extracts, see section 3.3.3).
- 2) Determination of the quantity of water that the plasters can absorb by capillarity ( $N_{48}$ , see data in Appendix G). This determination was performed for 14 samples. The resulting mean value of  $N_{48}$  is 24 vol.-%, which by a mean mortar density of  $1.9 \text{ g cm}^{-3}$  corresponds to about 130 ml water per kg mortar.
- 3) Calculation of the ionic concentrations for the case that:
  - a) The plasters contain the maximal amount of water that can be absorbed by capillarity ( $=N_{48}$ ).
  - b) The plasters contain only 50 % of the maximal amount of water that can be absorbed by capillarity. This roughly corresponds to the mean water content determined in two samples collected near location 4 (Fig. 3-8), at heights of 25 cm (80% of  $N_{48}$ ) and 40 cm (30% of  $N_{48}$ ) from the floor. Most investigated plasters are located in this height range.
- 4) Calculation of the saturation indexes with the PHREEQC code on the basis of the ionic concentrations.

The results obtained are an indicative estimate of the thermodynamic tendency of a specific mineral to precipitate in the pores of the mortar.

Fig. 3-22 shows the calculated saturation indexes for mirabilite and epsomite in the pore system of plaster 26, on which the observed efflorescing salts were mirabilite and thenardite. From the graphs it can be seen that mirabilite has a higher saturation index and thus a higher tendency to precipitate than epsomite. When the plaster is impregnated with the maximal amount of water that can be absorbed by capillarity, the solution is supersaturated with respect to mirabilite at temperatures below about 3 °C. In the situation that the impregnation is only 50 %, the temperature range for supersaturation is extended up to 9 °C. For plaster 24 (Fig. 3-23) the calculated saturation indexes indicate that the salt with higher tendency to precipitate is epsomite, which was in fact also the observed efflorescing salt. Supersaturation with respect to epsomite is reached for temperatures below about 3 °C, when the plaster is impregnated with only 50 % of the maximal amount of water that can be absorbed by capillarity.

The saturation index of thenardite is not shown in the figures, because thermodynamic data about this salt is missing from the *pitzer.dat* thermodynamic database used. The use of this database was necessary due to the high ionic strength ( $>5$ ) of the solutions (see 3.2.5).

However, due to the higher solubility of thenardite with respect to mirabilite, its saturation index is expected to be generally lower than that of mirabilite in the considered temperature range (0-30 °C), which was also confirmed by calculations using the *wateq4f.dat* database (accurate up to a ionic strength of ca. 0.7).

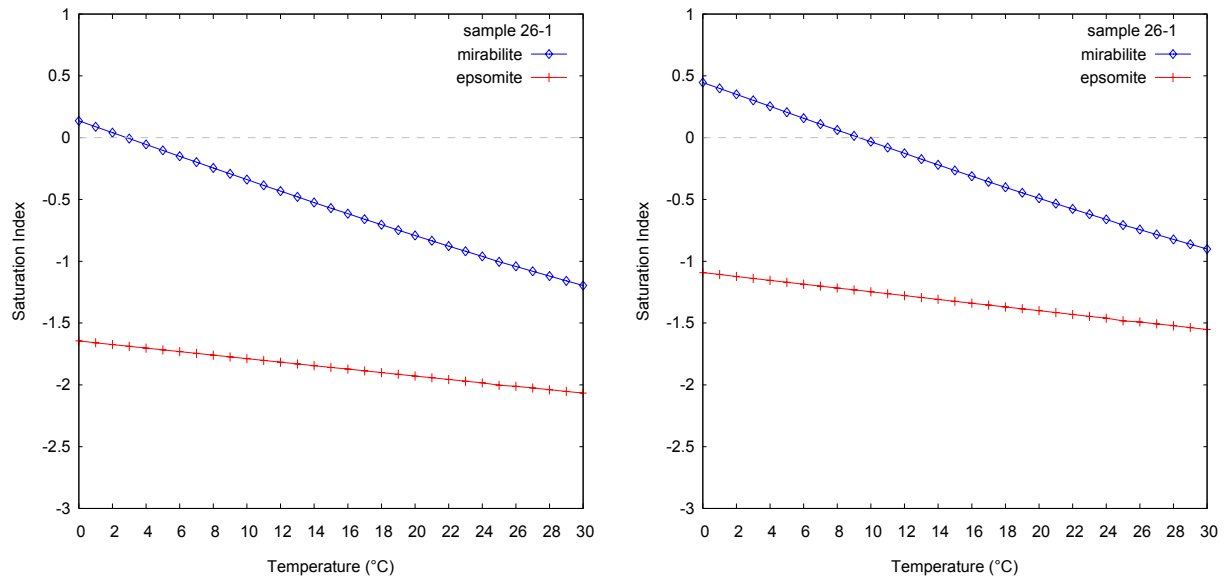


**Fig. 3-22.** Saturation indexes of mirabilite and epsomite in plaster at location 26 (sample 26-1, collected on the 25.4.2003). Left: pores filled with the maximal amount of water that can be absorbed by capillarity ( $N_{48}$ ). Right: pores filled with 50% of  $N_{48}$ . The observed efflorescing salt at this location were mirabilite and thenardite.

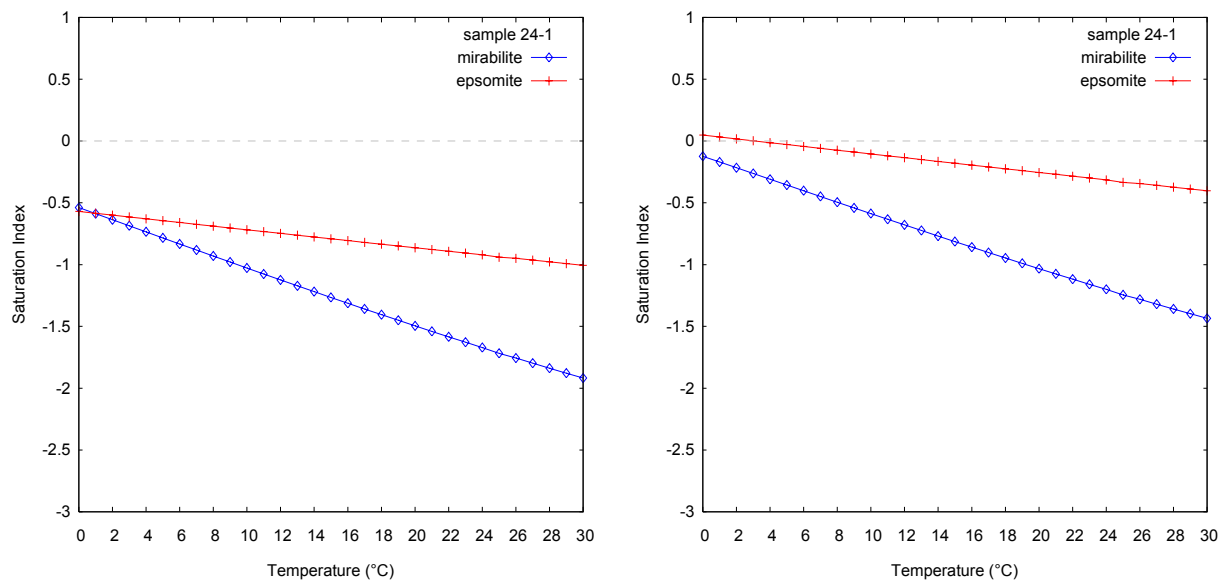


**Fig. 3-23.** Saturation indexes of mirabilite and epsomite in plaster at location 24 (sample 24-1, collected on the 25.4.2003). Left: pores filled with the maximal amount of water that can be absorbed by capillarity ( $N_{48}$ ). Right: pores filled with 50% of  $N_{48}$ . The observed efflorescing salt at this location was epsomite.

### 3.3.6 Reconstruction of phase transitions in the past

An estimation of the theoretical phase transitions during the period 1983-2002 was carried out for the pure salt systems  $\text{Na}_2\text{SO}_4\text{-H}_2\text{O}$  and  $\text{MgSO}_4\text{-H}_2\text{O}$ . Estimates are presented for the conditions on wall surfaces as well as for the conditions in the active layer of the plaster, as defined in 2.2.3.1.

Critical relative humidities of the considered salt systems were calculated on the basis of the simulated surface temperature, according to the equations in section 3.2.3. These were compared with the relative humidities simulated for the indoor air and for the active layer, respectively (simulations of T and RH for the period 1983-2002 are presented in section 2.3.5). In view of the observed salt behaviour (section 3.3.2), it was considered sufficient to perform the calculations with mean daily values of T and RH. Calculations made on the basis of hourly values would result in a larger number of transitions but, according to the observations, would be less realistic.

The theoretical phase transitions are given by the intersections between the curves of the relative humidity (of the air or of the active layer) with the ones of the critical relative humidity. As an example, the evolution for year 1995 is shown in Fig. 3-24. From this graph it can be clearly seen that the curve of RH in the active layer is smoother than the one of air RH. Accordingly, the number of the theoretical phase transitions within the plasters is smaller than on the surface of the walls (Fig. 3-25). It must however be emphasized that the results for the active layer are to be regarded as an indicative estimate; the effective environmental conditions within the plasters (i.e. the relative humidity) are in fact only computed and there is no verification of their correctness.

The calculated number of phase transitions on the wall surfaces lies between ca. 15 and 40 per year for mirabilite/thenardite and mostly between 0 and 6 per year for epsomite/hexahydrate (with the exception of year 1991, where 14 transitions were estimated). This result is accordance with the fact that the climate in the church during the twenty years in question was almost permanently within a range where phase transitions between mirabilite and thenardite should occur and where epsomite is supposed to be stable.

These estimates consider the case in which phase transitions occur each time the relative humidity of the air (or the one within the plaster) reaches the critical relative humidity of the salt, without taking into account the possible inertia of such salt systems.



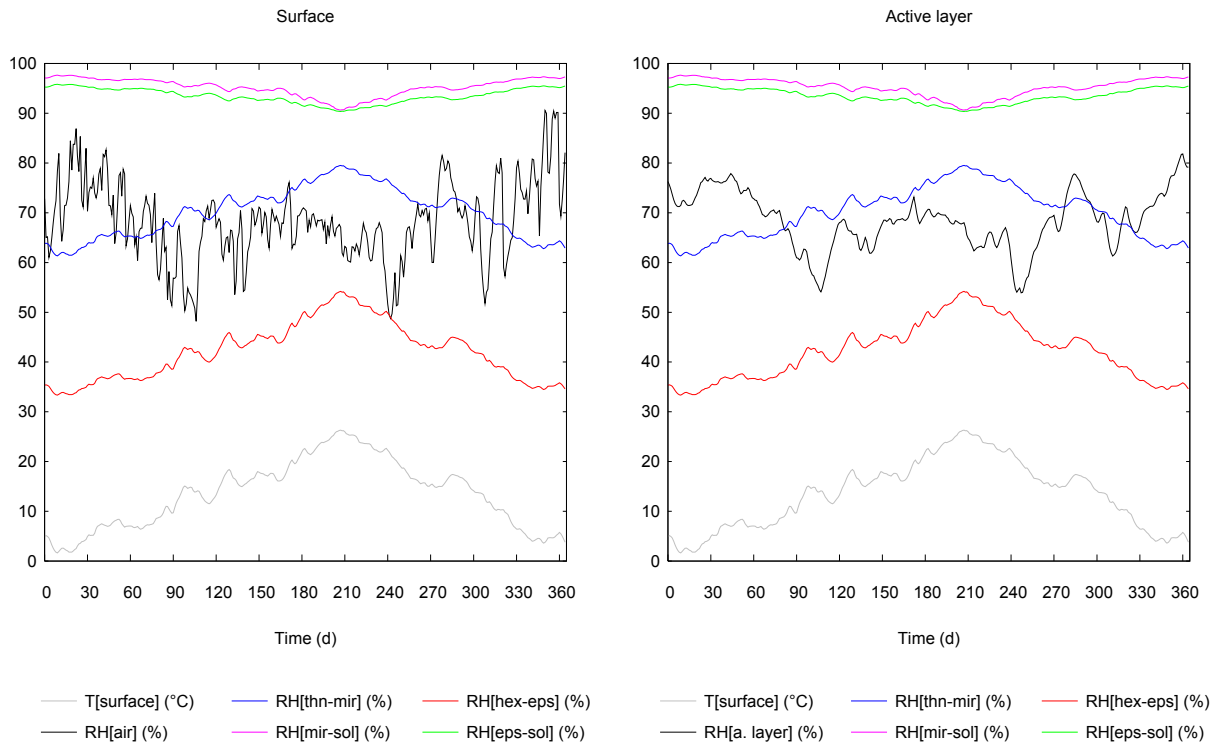


**Fig. 3-24.** Critical relative humidities of the systems  $\text{Na}_2\text{SO}_4\text{-H}_2\text{O}$  and  $\text{MgSO}_4\text{-H}_2\text{O}$ , RH of the air and RH of the active layer for year 1995 (daily mean values). Left: situation on wall surfaces. Right: situation in the active layer.

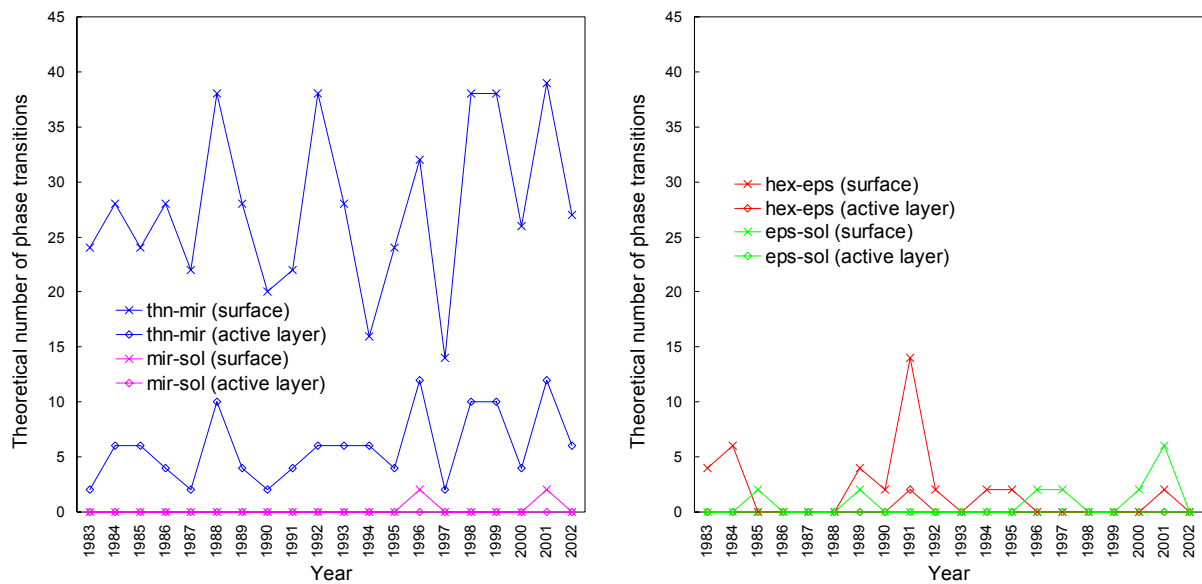


**Fig. 3-25.** Estimated yearly theoretical number of phase transitions for the period 1983-2002. Left:  $\text{Na}_2\text{SO}_4\text{-H}_2\text{O}$  system. Right:  $\text{MgSO}_4\text{-H}_2\text{O}$  system.

### 3.4 Discussion

The principal salt species observed in the church San Pietro Martire were mirabilite ( $\text{Na}_2\text{SO}_4 \cdot 10\text{H}_2\text{O}$ ), thenardite ( $\text{Na}_2\text{SO}_4$ ), epsomite ( $\text{MgSO}_4 \cdot 7\text{H}_2\text{O}$ ), trona ( $\text{Na}_3\text{H}(\text{CO}_3)_2 \cdot 2\text{H}_2\text{O}$ ) and niter ( $\text{KNO}_3$ ). Mirabilite, thenardite, epsomite and trona were recognized as being responsible for most of the observable damage. The majority of the affected areas was concentrated on the lower part of the walls, in the zone of rising damp. The most deteriorated surfaces, where the detachment of the plaster extended deeper into the wall, were associated with the occurrence of mirabilite/thenardite. Damage caused by trona was limited to the upper 0.5 cm, whereas deterioration caused by epsomite was even more superficial. Epsomite was also detected higher than the zone of rising damp, above the cornice, where water infiltration from the roof is supposed to have occurred. The observed damage caused by salt formation must have occurred after the early seventies, when the plasters were repaired and repainted.

On the basis of periodic surveys of salt-affected areas, which were performed over a period of two years (5 main sampling series), no other salt activity (i.e. crystallisation/dissolution or phase transitions between hydration states) than that of mirabilite/thenardite could be observed. This is in agreement with the theoretical behaviour of pure salts in relation to climate: trona is generally known to be extremely stable (see e.g. Gmelin, 1939) and the temperature as well as the relative humidity in the church were almost permanently within a range where epsomite and niter are supposed to be stable and where phase transitions between mirabilite and thenardite are to be expected (Fig. 3-10). The results of an estimation of the theoretical phase transitions for the systems  $\text{Na}_2\text{SO}_4\text{-H}_2\text{O}$  and  $\text{MgSO}_4\text{-H}_2\text{O}$ , performed on the basis of the simulated past indoor climate (see 2.3.5) and of the critical relative humidities, confirm this trend: the most frequent phase transition computed for the wall surfaces as well as for the active layer of the plasters during the period 1983-2002 has been that between mirabilite and thenardite (Fig. 3-25). Thenardite was observed both as a product of the dehydration of mirabilite (Fig. 3-11) and as a direct precipitate or recrystallized form (Fig. 3-12). Direct precipitation of thenardite from saturated solutions has been reported by Rodriguez-Navarro et al. (2000) to occur even at temperatures below the mirabilite-thenardite stability point of 32.4 °C, under conditions of low relative humidity. According to these authors, non-equilibrium crystallization is promoted by heterogeneous nucleation on a defect-rich support. Conversely, recrystallization can occur when thenardite that was formed by mirabilite dehydration is exposed to increasing humidity. Thenardite was found even in case of persistence of high relative humidity (up to 3-4 months, see salt sampling of 26.1.2004 in Fig. 3-10) where, according to the thermodynamics of the pure salt, the stable phase would be mirabilite (Fig. 3-2). This indicates a certain inertia of the transition from thenardite to mirabilite. This observation is in accordance with XRD measurements under controlled conditions of temperature and relative humidity carried out by Steiger et al. (2000): in some

cases the hydration of thenardite to mirabilite could not be observed although the conditions were such that mirabilite would be the stable form. According to the results of studies on the hydration-dehydration mechanism of  $\text{Na}_2\text{SO}_4$  by Charola and Weber (1992) and Doehne (1994), the hydration rate of thenardite is slowed down due to the formation of a hydrated film on the crystal surface. On the basis of the observations made during this study, the transition from mirabilite to thenardite seems to be faster (see sampling of 27.03.2004 in Fig. 3-10). It appears in any case that at least for the present salt system, daily mean values of temperature and RH provide enough resolution for investigating the relationships between indoor climate and salt dynamics.

The salt species observed in efflorescences show a clear relationship to the ionic content of the aqueous extracts from the underlying plasters (Fig. 3-13). Mirabilite and/or thenardite were efflorescing on plasters having a soluble salt content with a molar equivalent ratio  $\text{Na/Mg} > \sim 1$ . Epsomite was found for  $\text{Na/Mg} < \sim 1$ . For soluble salt compositions like those found in the investigated mortars, it is thus possible to roughly discriminate between the formation of sodium and magnesium sulphate solely on the basis of the ratio of the ions Na and Mg. Plaster samples collected in two different periods from the same location showed partly large variations in the composition of extractable ions. There is however no recognisable pattern, i.e. it is not possible to discriminate between a temporal variation of the composition and the variation due to the heterogeneous distribution of the salts within the plaster (Fig. 3-14).

The results of the analyses of the ions extracted from the mortars ( $\text{Na}^+$ ,  $\text{K}^+$ ,  $\text{Mg}^{2+}$ ,  $\text{Ca}^{2+}$ ,  $\text{Cl}^-$ ,  $\text{NO}_3^-$  and  $\text{SO}_4^{2-}$ ) were used as input data for the ECOS thermodynamic code (Price, 2000), which was combined with the RUNSALT user interface (Bionda, 2002-2005). Modelling was carried out for plasters showing efflorescence of mirabilite/thenardite or of epsomite. Plasters with trona efflorescence were not considered for the simulations because carbonates are not handled by ECOS; on the other hand, as mentioned above, trona is known to be stable under most environmental conditions. Plasters with niter efflorescence could not be considered because of the lack of analytical data (sampling not allowed at those locations).

The prediction of the phase transitions for the  $\text{MgSO}_4\text{-H}_2\text{O}$  system as performed by ECOS is in disagreement with published experimental data and should therefore be regarded as being incorrect. This problem was reported in Bionda (2004). The cause was later recognized (M. Steiger, pers. comm.) as being a parameterisation error in the ECOS code due to the use of an apparently too small value of the Gibbs free energy of formation for the  $\text{MgSO}_4\cdot 6\text{H}_2\text{O}$  phase. This explains the discrepancy between model predictions and observations made in the present study. In fact, although efflorescence of epsomite persisted throughout the whole monitoring period, this salt does not appear in the results of ECOS for the environmental conditions recorded in the church.

Model predictions for the occurrence of mirabilite complied with the observations, while those for thenardite were not always accurate. At a temperature of 10 °C, ECOS simulated the presence of thenardite at an RH<33-40%. In the reality, at this temperature thenardite has been observed also at an RH of 45%. For these environmental conditions (T=10°C and RH=45%) the model predicted instead the occurrence of various double salts, nitrates, as well as halite that, with exception of niter, were in fact not observed. The abovementioned discrepancy may suggest that the composition of the aqueous extracts does not reflect the heterogeneous distribution of the salts in the plasters. In other words efflorescences on the surface of the plasters, which by sampling are remixed with the salts in the pore system, in reality do not interact with ions in the pores in the way the simulation may suggest.

Being a thermodynamic model, ECOS can depict the state of a system at equilibrium, but does not provide any information about the speed at which a reaction will occur (see e.g. inertia of certain phase transitions). It is also to mention that the climatic conditions in the pore system of walls are mainly unknown. The climate below the surface of porous materials is not necessarily the same as in the indoor air. The hygric model presented in section 2.2.3 indicates that the amplitude and the frequency of RH fluctuations within a thin superficial layer of a wall (active layer) are smoothed in comparison to the RH of the indoor air. This estimation considers only the sorption of air moisture through the wall surface. In reality, the pore system in the zone of rising damp is also influenced by water movements through capillarity. In order to gain a better understanding of the behaviour of salts in walls, coupled heat, air, salt and moisture transport models are needed. Such models are under development, but are not yet available for a widespread use (see for instance the DELPHIN code by the Institute of Building Climatology of TU Dresden).

Saturations indexes give an indicative estimate of the thermodynamic tendency of a mineral to precipitate or dissolve in a given solution. The saturation indexes calculated show that the investigated pore solutions are near saturation with respect to the salts that were in fact observed in the efflorescences (section 3.3.5), namely mirabilite and epsomite. This is the case by a water impregnation of about 50% of the maximal amount of water that can be absorbed by capillarity, which can be considered roughly representative for the conditions in the lower zone of rising damp. It follows that lower water contents (e.g. by an increase of the evaporation rate triggered by a low RH), will readily lead to precipitation. In view of these considerations, dissolution and subsequent mobilisation of salt efflorescences by rising damp is not believed to play a major role in this specific case. Instead, such efflorescences will rather tend to accumulate, ultimately interacting with air humidity.

The calculation of saturation indexes allowed to extrapolate the crystallization of epsomite on plasters on which this salt was effectively observed. This is of particular interest in view of the fact that, as mentioned above, the ECOS code cannot correctly handle the  $\text{MgSO}_4\text{-H}_2\text{O}$  system.

## 4 CONCLUSIONS

Hygrothermal simulations of the indoor climate of an historical building (church San Pietro Martire in Gnosca) were performed with a novel hygric model (Simmler et al., 1995; 1996) used in combination with the HELIOS thermal code (Frank, 1982; Frank et al., 1982-1992). The simulations were compared with measurements performed in the study object. The results show that:

- Temperatures can be simulated with a good accuracy. The difference between measurement and model ranged from  $-1.4$  to  $+1.2$  °C for 95% of the values computed for the indoor air over a period of ten months. For a wall surface, the discrepancy ranged from  $-1.6$  to  $+0.9$  °C for 95% of the values computed over a period of three months. (Compare with the accuracy of the measuring equipment of  $\pm 0.5$  °C).
- For air humidity, computed on the basis of the simulated temperatures, the discrepancy between measurement and model varied from  $-0.9$  to  $+1.0$  g m<sup>-3</sup> (absolute humidity) and  $-6.5$  to  $+7.7\%$  (relative humidity) for 95% of the values over a period of ten months. (Compare with the accuracy of the measuring equipment of  $\pm 2\%$  RH). This discrepancy is partly explained by the fact that the RH is affected exponentially by inaccuracies in the temperature (a variation of  $\pm 1$  °C at a temperature of 15 °C and an absolute humidity of 10 g m<sup>-3</sup> causes an RH variation of nearly  $\pm 5\%$ ).
- The combination of HELIOS with the tested hygric model constitute a viable method for hygrothermal simulations in historical buildings, provided that thermal simulations are as accurate as possible.
- The applicability of the models is constrained by the difficulty of gaining sufficient knowledge of the building and material characteristics (see e.g. problem of destructive sampling, variety and complexity of materials). Under these circumstances it is important to recognise at least those parameters, which can mostly affect the simulations and that should thus be determined with care. As a general rule, it can be said that very important building elements are those through which a significant heat or humidity transfer may occur. Depending on the peculiarities of the building, these can be, as for instance in the present study object, the air change rate (important for both hygric and thermal simulation), the area of the ceiling and the window glazing (important for the thermal simulation) as well as the indoor moisture sources (important for the hygric simulation).
- The performance of indoor climate simulations is largely influenced by the quality and availability of meteorological data. Advanced building energy codes like HELIOS require as input a fairly large set of meteorological parameters that are not always

available or might not fit well the situation, as in the case that the measuring station is far away from the building's site. It is therefore advisable to perform a preliminary check of the suitability of the meteorological data used, for instance by a comparison of METEONORM data for the two sites.

- The use of advanced thermal codes can be demanding in both terms of time investment and required building physics knowledge. There might be however situations or a whole category of historical buildings (simple construction type), for which a reasonable estimate of the indoor temperature can be obtained with a very simple building specification and on the basis of only few meteorological parameters. This was shown by using a simple model developed in the course of this study.
- The applicability of hygrothermal models to historical buildings provides the opportunity to use these tools to perform risk assessment. This application can be of particular interest when renovation works are to be planned, in case a change of use of an edifice is foreseen or when the relation between climate and damage occurring in a building (e.g. salt weathering) is to be investigated. In all these situations, which are more and more topical, the consequences of a change like substituting old windows, setting up a new heating system or increasing the number of users of a building, can be comprehensively explored, thus substantially contributing to the implementation of the concept of sustainable conservation.
- The reconstructions of the indoor climate performed for the period 1983-2003 have shown that an extreme event like the heat wave of summer 2003 can have a major impact on the indoor temperature and relative humidity of historical buildings. This observation confirms the importance of assessing the risks bound to extreme climatic events or climate change scenarios as part of the concept of sustainable care. Combining indoor climate models with regional/global climate models or climate generators would allow to forecast possible indoor climate scenarios.
- Independently from the aims, models like the ones tested in this study offer the big advantage of allowing investigations of the climatic conditions over a period of many years (in the past or in the future), without having to rely on long-term in situ measurements of the climate.

The behaviour of hygroscopic salts in relation to the indoor climate in the church San Pietro Martire was investigated by means of in situ monitoring and of modelling.

- The principal salt species observed were mirabilite ( $\text{Na}_2\text{SO}_4 \cdot 10\text{H}_2\text{O}$ ), thenardite ( $\text{Na}_2\text{SO}_4$ ), epsomite ( $\text{MgSO}_4 \cdot 7\text{H}_2\text{O}$ ), trona ( $\text{Na}_3\text{H}(\text{CO}_3)_2 \cdot 2\text{H}_2\text{O}$ ) and niter ( $\text{KNO}_3$ ). Mirabilite, thenardite, epsomite and trona were recognized as being responsible for

most of the observable damage. The majority of the affected areas was concentrated on the lower part of the walls, in the zone of rising damp.

- It has been possible to roughly discriminate between the formation of sodium and magnesium sulphate salts on the basis of the ratio of the ions Na and Mg as determined in aqueous extracts from plasters: mirabilite and/or thenardite were efflorescing on plasters having a soluble salt content with a molar equivalent ratio  $\text{Na/Mg} > \sim 1$ . Epsomite was found for  $\text{Na/Mg} < \sim 1$ .
- The only salt activity observed was the phase transition between mirabilite and thenardite. Observations of the salt behaviour in relation to climate suggest that efflorescences behaved like pure salts. In this case the activity of efflorescences can be estimated solely on the basis of critical relative humidities for the pure salt system in question and of the relative humidity of the air in the building. An exception is represented by the persistence of thenardite at high relative humidity, indicating a certain inertia of the transition from thenardite to mirabilite, a behaviour that is also reported in the literature.
- The ECOS thermodynamic model (Price, 2000) was tested in real situations by comparing simulation results with efflorescences actually observed on plasters. Due to the restrictions of ECOS (e.g. inability to handle carbonates) and in view of the salt species found in the church, the test was restricted to plasters showing efflorescences of mirabilite/thenardite and of epsomite. It has been found that, due to a parameterisation error in the code, ECOS is not able to correctly model the behaviour of magnesium sulphate salts, in particular the transition epsomite-hexahydrite. The predictions for the occurrence of mirabilite complied with the observed efflorescences, while the computed RH range of stability of thenardite was not confirmed by observations. This discrepancy might be interpreted as an indication that the behaviour in relation to climate of investigated efflorescences is not affected by the salt composition in the pores.
- Saturation indexes of the relevant soluble salt species in pore solutions have been calculated using the hydrogeochemical code PHREEQC (Parkhurst and Appelo, 1999) in order to estimate the thermodynamic tendency of the salts to precipitate. A correlation between the obtained saturation indexes and the efflorescences on the plasters has been observed. The calculation of saturation indexes for highly concentrated solutions, like the ones to be found in walls, has been possible since a recent update of PHREEQC (version 2.12) includes an implementation of the Pitzer ion interaction formulation (Pitzer, 1973; 1991). This allows to use this code to model pore solutions in walls in connection with investigations on salt behaviour.

## 5 REFERENCES

- Ambrosetti, G. and Martella, A., 1991. Chiesa parrocchiale di San Pietro Martire, Gnosca - Analisi dell'edificio. G. Ambrosetti e A. Martella Architetti, Bellinzona.
- Anderes, B., 1998. Guida d'Arte della Svizzera italiana. Nuova Edizioni Trelingue SA, Società di Storia dell'Arte in Svizzera, 543 pp.
- Appelo, C.A.J. and Postma, D., 2005. Geochemistry, groundwater and pollution, 2nd edition. A.A. Balkema Publishers, Leiden, The Netherlands, 649 pp.
- Arendt, C., 1993. Raumklima in grossen historischen Räumen. Heizungsart - Heizungsweise - Schadensentwicklung - Schadensverhinderung. Verlagsgesellschaft Rudolf Müller, Köln, 152 pp.
- Arnold, A., 1984. Determination of mineral salts from monuments. *Studies in Conservation*, 29/3: 129-138.
- Arnold, A. and Zehnder, K., 1984. Evaporite und Verwitterung an Bauwerken. *Eclogae geologicae Helvetiae*, 77(2): 287-300.
- Arnold, A. and Zehnder, K., 1991. Monitoring Wall Paintings Affected by Soluble Salts. In: S. Cather (Editor), *The Conservation of Wall Paintings. Proceedings of a symposium organized by the Courtauld Institute of Art and the Getty Conservation Institute*, London, July 13-16, 1987. The Getty Conservation Institute, pp. 103-136.
- Ball, J.W. and Nordstrom, D.K., 1991. User's manual for WATEQ4F, with revised thermodynamic data base and test cases for calculating speciation of major, trace, and redox elements in natural waters. US Geological Survey, Open-File Report 91-183 (Revised and reprinted - April, 2001), 188 pp.
- Baumann, E., 1993. Energie in kirchlichen Gebäuden sinnvoll nutzen, Studie zum Beheizen von Kirchen im Auftrag des Kirchenrates der evang.-ref. Kirche des Kantons St. Gallen.
- Bianconi, P. and Vicari, V., 1968. Campanili del Ticino. Quaderni Ticinesi, 11. Società ticinese per la conservazione delle bellezze naturali ed artistiche. Arti grafiche La Malcantonese, Agno.
- Bionda, D., 2002-2005. RUNSALT computer program.
- Bionda, D., 2004. Methodology for the preventive conservation of sensitive monuments: microclimate and salt activity in a church, 10th International Congress on Deterioration and Conservation of Stone, June 27 - July 2. ICOMOS Sweden, Stockholm, pp. 627-634.
- Bionda, D. and Storemyr, P., 2002. Modelling the behaviour of salt mixtures in walls: a case study from Tenaille von Fersen, Suomenlinna, Finland. In: T. Von Konow (Editor),



- The study of salt deterioration mechanisms. Decay of brick walls influenced by interior climate changes. Suomenlinnan hoitokunta, pp. 95-101.
- Bläuer Böhm, C., 1994. Salzuntersuchungen an Baudenkmälern. Z. Kunsttechnologie und Konservierung, 8/1: 86-103.
- Bläuer Böhm, C., 1996. Assessment of quantitative salt analysis by the water extraction method on lime mortars, 8th International Congress on Deterioration and Conservation of Stone, Sept. 30 - Oct. 4, Berlin, pp. 1505-1519.
- CGB, 2000. Chiesa parrocchiale di San Pietro Martire, Gnosca. CGB restauri, Bellinzona.
- Charlesworth, P.S., 1988. Air exchange rate and airtightness measurement techniques - An Application guide. Air Infiltration and Ventilation Centre, 228 pp.
- Charola, A.E., 2000. Salts in the deterioration of porous materials: an overview. Journal of the American Institute for Conservation, 39(3): 327-343.
- Charola, A.E. and Weber, J., 1992. The hydration-dehydration mechanism of sodium sulphate. In: J. Delgado Rodrigues, F. Henriquez and J.T. Jeremias (Editors), 7th International Congress on the Deterioration and Conservation of Stone, Laboratorio Nacional de Engenharia Civil, Lisbon, pp. 581-590.
- Chou, I.-M. and Seal, R.R., 2003. Determination of Epsomite–Hexahydrate Equilibria by the Humidity-Buffer Technique at 0.1 MPa with Implications for Phase Equilibria in the System  $\text{MgSO}_4\text{--H}_2\text{O}$ . Astrobiology, 3(3): 619-630.
- Crank, J., 1975. The Mathematics of Diffusion. Oxford University Press, Oxford.
- Cunningham, M.J., 1992. Effective penetration depth and effective resistance in moisture transfer. Building and Environment, 27(3): 379-386.
- Doehne, E., 1994. In situ dynamics of sodium sulfate hydration and dehydration in stone pores: Observations at high magnification using the environmental scanning electron microscope. In: V. Fassina, H. Ott and F. Zezza (Editors), 3rd International Symposium on the Conservation of Monuments in the Mediterranean Basin, Venice, pp. 143-150.
- Doehne, E., 2002. Salt weathering: a selective review. In: S. Siegesmund, T. Weiss and A. Vollbrecht (Editors), Natural stone, weathering phenomena, conservation strategies and case studies. Geological Society Special Publication No. 205, London, pp. 51-64.
- Elberskirch, P., 1937. Der praktische Beizer und Polierer. Druckerei-Verlag Hans Rösler, Augsburg.
- Evans, I.S., 1970. Salt crystallization and rock weathering: A review. Revue de Géomorphologie Dynamique, 19(4): 153-177.
- Flatt, R.J., 2002. Salt damage in porous materials: how high supersaturations are generated. Journal of Crystal Growth, 242: 435–454.
- Frank, T., 1982. Programmbeschrieb HELIOS 1, EMPA Abteilung Bauphysik.

- Frank, T., Ghazi Wakili, K. and Simmler, H., 1999. HELIOS-HYGRO - Ein Simulationsmodell zur thermisch-hygrischen Gebäudeanalyse, Feuchtetag '99, Umwelt - Meßverfahren - Anwendungen, Berlin.
- Frank, T., Püntener, T.W., Mathis, K. and Heierli, J., 1982-1992. HELIOS. EMPA Abteilung Bauphysik, CH-8600 Dübendorf.
- Franzen, C., 2002. Historische Bauwerksteine in Südtirol. Verteilung und Verwitterungsverhalten. PhD Thesis, Leopold-Franzens-Universität Innsbruck.
- Gilardoni, 1972. I monumenti d'arte e di storia del Canton Ticino. Birkhäuser, Basel.
- Gmelin, 1939. Handbuch der Anorganischen Chemie. Magnesium Teil B. System-Nummer 27. Verlag Chemie, Berlin.
- Goudie, A. and Viles, H., 1997. Salt weathering hazards. Wiley, Chichester.
- Hagentoft, C.E., 2001. Introduction to Building Physics. Studentlitteratur, Lund, Sweden, 422 pp.
- Haible, B. and Steingold, S., 2004. CLISP version 2.33.1 - ANSI Common Lisp compiler, interpreter and debugger.
- Hardie, L.A. and Eugster, H.P., 1970. The evolution of closed-basin brines. Mineral. Soc. Am. Spec. Publ., 3: 273-290.
- Holm, A., Künzle, H.M. and Sedlbauer, K., 2003. The hygrothermal behaviour of rooms: combining thermal building simulation and hygrothermal envelope calculation, Eighth International IBPSA Conference, August 11-14, 2003, Eindhoven, Netherlands, pp. 499-506.
- Keller, B., 2004. Bauphysik. Teil 1: die Energetik des Gebäudes. Vorlesung für Studierende des Bauingenieurwesens. ETH Zürich, 221 pp.
- Klopfer, H., 1974. Wassertransport durch Diffusion in Feststoffen. Bauverlag, Wiesbaden, 235 pp.
- Künzle, H.M., Holm, A., Zirkelbach, D. and Karagiozis, A.N., 2005. Simulation of indoor temperature and humidity conditions including hygrothermal interactions with the building envelope. Solar Energy, 78: 554-561.
- Kusuda, T., 1969. Thermal response factors for multilayer structures of various heat conduction systems. ASHRAE Transactions, 75(1): 246-271.
- Luterbacher, J., Dietrich, D., Xoplaki, E., Grosjean, M. and Wanner, H., 2004. European seasonal and annual temperature variability, trends, and extremes since 1500. Science, 303: 1499-1503.
- METEOTEST, 2003. METEONORM - Global Meteorological Database for Engineers, Planners and Education. METEOTEST, Fabrikstrasse 14, CH-3012 Bern, Switzerland.
- Mitalas, G.P., 1968. Calculation of transient heat flow through walls and roofs. ASHRAE Transactions, 74: 182-188.
- Optics5. Lawrence Berkeley National Laboratory.

- Parkhurst, D.L. and Appelo, C.A.J., 1999. User's Guide to PHREEQC (Version 2) - A Computer Program for Speciation, Batch-Reaction, One-Dimensional Transport, and Inverse Geochemical Calculations. US Geological Survey, Water Resources Investigation Report 99-4259, 312 pp.
- Piper, A.M., 1944. A graphic procedure in the geochemical interpretation of water analyses. American Geophysical Union Transactions, 25: 914-923.
- Pitzer, K.S., 1973. Thermodynamics of electrolytes, I. Theoretical basis and general equations. J. Phys. Chem., 77: 268-277.
- Pitzer, K.S., 1991. Ion interaction approach: Theory and data correlation. In: K.S. Pitzer (Editor), Activity Coefficients in Electrolyte Solutions. CRC Press, Boca Raton, pp. 75-153.
- Plummer, L.N., Parkhurst, D.L., Fleming, G.W. and Dunkle, S.A., 1988. A Computer Program Incorporating Pitzer's Equations for Calculation of Geochemical Reactions in Brines. U.S. Geological Survey, Water Resources Investigations Report 88-4153.
- Price, C.A. (Editor), 2000. An expert chemical model for determining the environmental conditions needed to prevent salt damage in porous materials. European Commission Research Report No 11 (Protection and Conservation of European Cultural Heritage). Archetype Publications, London, 136 pp.
- Price, C.A. and Brimblecombe, P., 1994. Preventing salt damage in porous materials. In: A. Roy and P. Smith (Editors), Preventive conservation, practice, theory and research. International Institute for Conservation of Historic and Artistic Works, London, pp. 90-93.
- Rodriguez-Navarro, C., Doehne, E. and Sebastian, E., 2000. How does sodium sulfate crystallize? Implications for the decay and testing of building materials. Cement and Concrete Research, 30: 1527-1534.
- Sagelsdorff, R. and Frank, T., 1990. Wärmeschutz und Energie im Hochbau. Element 29. Schweizerische Ziegelindustrie.
- Sawdy, A., 2001. The Kinetics of Salt Weathering of Porous Materials: Stone Monuments and Wall Paintings. PhD Thesis, Institute of Archaeology, University College London.
- Sawdy, A. and Price, C.A., 2005. Salt damage at Cleeve Abbey, England. Part I: a comparison of theoretical predictions and practical observations. Journal of Cultural Heritage, 6: 125-135.
- Schär, C., Vidale, P.L., Lüthi, D., Frei, C., Häberli, C., Liniger, M.A. and Appenzeller, C., 2004. The role of increasing temperature variability in European summer heatwaves. Nature, 427: 332-336.
- Schellen, H.L., 2002. Heating Monumental Churches: Indoor Climate and Preservation of Cultural Heritage. PhD thesis Thesis, Technische Universiteit Eindhoven, 228 pp.

- Schijndel, A.W.M. and Hensen, J.L.M., 2005. Integrated heat, air and moisture modeling toolkit in Matlab, Ninth International IBPSA Conference, August 15-18, Montréal, Canada, pp. 1107-1114.
- Schmid, A.A. (Editor), 1976. Kunstführer durch die Schweiz. Begründet von Hans Jenny, Band 2: Genf, Neuenburg, Waadt, Wallis, Tessin. Böhler Verlag, Zürich.
- Sell, J., 1997. Eigenschaften und Kenngrößen von Holzarten. Buchreihe Lignum. Baufachverlag, Zürich, 88 pp.
- Simmler, H., Heierli, J., Rickert, H. and Vonbank, R., 1995. Humidity balance model for indoor environment, International Workshop on Mass-Energy Transfer and Deterioration of Building Components, Paris, January 9-11.
- Simmler, H., Heierli, J., Rickert, H. and Vonbank, R., 1996. Feuchtebilanzmodell zur Beschreibung des Feuchteverhaltens von Innenräumen, Heat, Air and Moisture Transfer in New and Retrofitted Insulated Envelope Parts. IEA Annex 24. EMPA Abteilung Bauphysik.
- Standard EN ISO 13370, 1998. Thermal performance of buildings - Heat transfer via the ground - Calculations methods.
- Standard ISO 6946, 1996. Building components and building elements - Thermal resistance and thermal transmittance - Calculation method.
- Standard SIA 381/1, 1980. Baustoff-Kennwerte. Schweizerischer Ingenieur- und Architekten-Verein.
- Steiger, M., 2003. Thermodynamische Eigenschaften von Salzgemischen. In: H. Leitner, S. Laue and H. Siedel (Editors), Mauersalze und Architekturoberflächen. Hochschule für Bildende Künste Dresden, 1-3 Februar 2002, pp. 25-35.
- Steiger, M., Beyer, R., Dorn, J. and Zeunert, A., 2000. Data compilation and experimental determinations. In: C.A. Price (Editor), An expert chemical model for determining the environmental conditions needed to prevent salt damage in porous materials. European Commission Research Report No 11 (Protection and Conservation of European Cultural Heritage). Archetype Publications, London, pp. 19-44.
- Steiger, M. and Dannecker, W., 1995. Hygroskopische Eigenschaften und Kristallisationsverhalten von Salzgemischen. In: R. Snethlage (Editor), Jahresberichte aus dem Forschungsprogramm Steinzerfall - Steinkonservierung. Band 5 - 1993. Verlag Ernst & Sohn, Berlin, pp. 115-128.
- Steiger, M., Neumann, H.-H., Grodten, T., Wittenburg, C. and Dannecker, W., 1998. Salze in Natursteinmauerwerk - Probenahme, Messung und Interpretation. In: R. Snethlage (Editor), Denkmalpflege und Naturwissenschaft - Natursteinkonservierung II. Fraunhofer IRB Verlag, Stuttgart, pp. 61-91.
- Steiger, M. and Zeunert, A., 1996. Crystallization properties of salt mixtures: comparison of experimental results and model calculations. In: J. Riederer (Editor), 8th International

- Congress on Deterioration and Conservation of Stone, Sept. 30 - Oct. 4, Berlin, pp. 535-544.
- Stephenson, D.G. and Mitalas, G.P., 1967. Room thermal response factors. ASHRAE Transactions, 73(2): III.1.1-1.7.
- Storemyr, P., 2002. The Regalia Room Mural Paintings Conservation Project, Trondheim, Norway: Conservation Measures and Monitoring of Salt Weathering 2001-2002. Report no. 2002-051, Expert Center für Denkmalpflege, Zürich.
- Weitzmann, P., Sasic Kalagasidis, A., Nielsen, T.R., Peuhkuri, R. and Hagetoft, C.E., 2003. Presentation of the International Building Physics Toolbox for Simulink, Eighth International IBPSA Conference, August 11-14, 2003, Eindhoven, Netherlands, pp. 1369-1376.
- Williams, T. and Kelley, C., 2004. gnuplot version 4.0 - An Interactive Plotting Program.
- Wit, M.H., 2004. WAVO - A model for the simulation of the thermal and hygric performance of building and systems. Eindhoven University of Technology.
- Zürcher, C. and Frank, T., 1998. Bauphysik - Bau und Energie. Leitfaden für Planung und Praxis, Band 2. vdf, Hochschulverlag an der ETH, Zürich, 231 pp.

## **Appendices**

## Appendix A

### Water vapour calculations

**:: Saturated vapour pressure (Pa)**

**:: Magnus formula from Tetens (1930) as given in Murray F.W., J. Appl. Met. 6, 1967**

**> ps:=100\*10^(7.5\*T/(T+237.3)+0.7858)**

**:: T=temperature (°C)**

**:: Vapour pressure (Pa)**

**> p:=ps\*RH/100**

**:: RH=relative humidity (%)**

**:: Absolute humidity (g/m<sup>3</sup>)**

**> ah:=p/(T+273.16)\*(M/R)**

**> M:=18.01534**

**> R:=8.314**

**:: Dew point (°C)**

**:: = temperature at which p=ps**

**:: 1) calculate p at RH, T**

**:: 2) substitute ps with p in the ps equation and solve for T**

**:: p=ps=100\*10^(log10(6.1078)+7.567\*T/(T+239.7))**

**> dp:=log10(p/610.78)\*239.7/(7.567-log10(p/610.78))**

# Appendix B

## HELIOS input file

```

METEO                                     BAUTEILE
-----
[-]                                     [-]
AAAAAAAAAAAAAAAAAAAAAAAAAAAAAAAAAAAAA AAAAAAAAAAAAAAAAAAAAAAAAAAAAAAAAAAA
LOCQ.BIN                                GNOSCA.KAT
*****
PROJEKT                                VAR
-----
[-]                                     [-]
AAAAAAAAAAAAAAAAAAAAAAAAAAAAAAAAAAAAA AAAAAAAAAAAAAAAAAAAAAAAAAAAAAAAAAAA
Gnosca, Chiesa San Pietro Martire
*****
VOL    AIRCR    QINT    THEAT    TCOOL    TINIT    LAMBDA    PHI    ZONE
-----
[M3]   [1/H]    [W]     [C]     [C]     [C]     [GRAD]   [GRAD]   [H]
XXXXX.XX XXX.XX XXXXX.X XX.X  XX.X  XX.X  XX.XX  XX.XX  XX
1200.00  0.10   0.0    -10.0  50.0  10.0  -9.02  46.24  -1
*****
HKL     HSB     HSW     QIK     QIS     QSK     QSB     QSW
-----
[-]     [-]     [-]     [-]     [-]     [-]     [-]     [-]
X.XX    X.XX    X.XX    X.XX    X.XX    X.XX    X.XX    X.XX
0.50    0.20    0.30    0.60    0.40    0.30    0.50    0.20
*****
NDAY    NMO     NYR     IHR     PFLG    OFLG    NFLG    NRFLG    WAB
-----
[-]     [-]     [-]     [-]     [-]     [-]     [-]     [-]     [-]
XX      XX     XXXX   XXXX   X      X      X      X      X
1       1     2002  9999  2      1      1      0      0
*****
KWIRK   VWIRK   QCA    GLARE   AIRCH
-----
[-]     [-]     [kW]   [W/M2]  [1/H]
X.XX    X.XX   XXX.XX XXXX.X XX.XX
1.00    1.00  -999.99 1000.0 10.00
*****
TLA     TGR     TVA     TRA     HN      CT      CW      CS
-----
[C]     [C]     [C]     [C]     [-]     [K]     [KS/M]  [M2K/W]
XX.XX   XX.XX  XX.XX  XX.XX  X.XX   X.XX   X.XX   X.XX
-10.00  20.00  45.00  30.00  1.33   0.00   0.00   0.00
*****
ND      NW     NKA     NB      NWI     NBI     NF
-----
[-]     [-]     [-]     [-]     [-]     [-]     [-]
XX      XX     XX     XX     XX     XX     XX
0       4      3      1      2      0      3
*****
CNAME   BAUTEIL    AS     EPS     FL     WAZ     SL     AI
-----
[-]     [-]         [-]     [-]     [M2]   [GRAD]  [GRAD]  [W/M2K]
AAAAA    XX/AAAAA    X.XX   X.XX  XXXX.XX XXX.XX  XX.XX   XX.XX
Wand_SW  WAND90_GSPM    0.55   0.97 105.00 -60.00  90.00   8.00
*****
CNAME   BAUTEIL    AS     EPS     FL     WAZ     SL     AI
-----
[-]     [-]         [-]     [-]     [M2]   [GRAD]  [GRAD]  [W/M2K]
AAAAA    XX/AAAAA    X.XX   X.XX  XXXX.XX XXX.XX  XX.XX   XX.XX
Wand_NW  WAND90_GSPM    0.32   0.97 95.00  -150.00 90.00   8.00
*****
CNAME   BAUTEIL    AS     EPS     FL     WAZ     SL     AI
-----
[-]     [-]         [-]     [-]     [M2]   [GRAD]  [GRAD]  [W/M2K]
AAAAA    XX/AAAAA    X.XX   X.XX  XXXX.XX XXX.XX  XX.XX   XX.XX
Wand_SO  WAND90_GSPM    0.32   0.97 105.00 30.00  90.00   8.00
*****
CNAME   BAUTEIL    AS     EPS     FL     WAZ     SL
-----
[-]     [-]         [-]     [-]     [M2]   [GRAD]  [GRAD]
AAAAA    XX/AAAAA    X.XX  XXXX.XX XXX.XX  XX.XX
Gewoelbe GEWOELB_GSPM 0.00 220.00 0.00 0.00
*****
AI      AA      TRED    TA      NTYP
-----
[W/M2K] [W/M2K]    [-]     [C]     [-]
XX.XX   XX.XX   X.XX   XX.XX   XX
8.00    4.17    1.00   0.00   0
*****
CNAME   BAUTEIL    AS     FL     WAZ     SL
-----
[-]     [-]         [-]     [M2]   [GRAD]  [GRAD]
AAAAA    XX/AAAAA    X.XX  XXXX.XX XXX.XX  XX.XX
Turmwand WAND100_GSPM 0.00 45.00 -150.00 90.00
*****
AI      AA      TRED    TA      NTYP
-----
[W/M2K] [W/M2K]    [-]     [C]     [-]
XX.XX   XX.XX   X.XX   XX.XX   XX
8.00    4.35    1.00   0.00   0
*****

```



CNAME	BAUTEIL	AS	FL	WAZ	SL		
[-]	[-]	[-]	[M2]	[GRAD]	[GRAD]		
AAAAAAAAAAAA	XX/AAAAAAAA	X.XX	XXXX.XX	XXX.XX	XX.XX		
Sakrwand	WAND70_GSPM	0.00	27.00	30.00	90.00		
*****							
AI	AA	TRED	TA	NTYP			
-----							
[W/M2K]	[W/M2K]	[-]	[C]	[-]			
XX.XX	XX.XX	X.XX	XX.XX	XX			
8.00	4.35	1.00	0.00	0			
*****							
CNAME	BAUTEIL	FL	AI	AA	TB		
-----							
[-]	[-]	[M2]	[W/M2K]	[W/M2]	[C]		
AAAAAAAAAAAA	XX/AAAAAAAA	XXXX.XX	XX.XX	XX.XX	XX.XX		
Boden	BODEN_GSPM	175.00	6.00	0.46	0.00		
*****							
CNAME	BAUTEIL	FL	AI				
-----							
[-]	[-]	[M2]	[W/M2K]				
AAAAAAAAAAAA	XX/AAAAAAAA	XXXX.XX	XX.XX				
Holzteile	HOLZ_GSPM	124.00	8.00				
*****							
CNAME	BAUTEIL	FL	AI				
-----							
[-]	[-]	[M2]	[W/M2K]				
AAAAAAAAAAAA	XX/AAAAAAAA	XXXX.XX	XX.XX				
Wandteile	WAND100_GSPM	6.00	8.00				
*****							
CNAME	BAUTEIL	FF	RZN	FAZ	FSL	AIF	SRED
-----							
[-]	[-]	[M2]	[M2K/W]	[GRAD]	[GRAD]	[W/M2K]	[-]
AAAAAAAAAAAA	XX/AAAAAAAA	XXXX.XX	XXX.XX	XXX.XX	XX.XX	XX.XX	X.XX
FensterNW	GLAS2MM_GSPM	4.60	0.00	-150.00	90.00	8.00	1.00
*****							
CNAME	BAUTEIL	FF	RZN	FAZ	FSL	AIF	SRED
-----							
[-]	[-]	[M2]	[M2K/W]	[GRAD]	[GRAD]	[W/M2K]	[-]
AAAAAAAAAAAA	XX/AAAAAAAA	XXXX.XX	XXX.XX	XXX.XX	XX.XX	XX.XX	X.XX
FensterSO	GLAS2MM_GSPM	6.90	0.00	30.00	90.00	8.00	1.00
*****							
CNAME	BAUTEIL	FF	RZN	FAZ	FSL	AIF	SRED
-----							
[-]	[-]	[M2]	[M2K/W]	[GRAD]	[GRAD]	[W/M2K]	[-]
AAAAAAAAAAAA	XX/AAAAAAAA	XXXX.XX	XXX.XX	XXX.XX	XX.XX	XX.XX	X.XX
FensterSW	GLAS2MM_GSPM	2.70	0.00	-60.00	90.00	8.00	1.00
*****							
SQ( 1)SQ( 2)SQ( 3)SQ( 4)SQ( 5)SQ( 6)SQ( 7)SQ( 8)SQ( 9)SQ(10)SQ(11)SQ(12)							
-----							
[-]	[-]	[-]	[-]	[-]	[-]	[-]	[-]
X.XX	X.XX	X.XX	X.XX	X.XX	X.XX	X.XX	X.XX
1.00	1.00	1.00	1.00	1.00	1.00	1.00	1.00
*****							
SQ(13)SQ(14)SQ(15)SQ(16)SQ(17)SQ(18)SQ(19)SQ(20)SQ(21)SQ(22)SQ(23)SQ(24)							
-----							
[-]	[-]	[-]	[-]	[-]	[-]	[-]	[-]
X.XX	X.XX	X.XX	X.XX	X.XX	X.XX	X.XX	X.XX
1.00	1.00	1.00	1.00	1.00	1.00	1.00	1.00
*****							
SH( 1)SH( 2)SH( 3)SH( 4)SH( 5)SH( 6)SH( 7)SH( 8)SH( 9)SH(10)SH(11)SH(12)							
-----							
[-]	[-]	[-]	[-]	[-]	[-]	[-]	[-]
X.XX	X.XX	X.XX	X.XX	X.XX	X.XX	X.XX	X.XX
1.00	1.00	1.00	1.00	1.00	1.00	1.00	1.00
*****							
SH(13)SH(14)SH(15)SH(16)SH(17)SH(18)SH(19)SH(20)SH(21)SH(22)SH(23)SH(24)							
-----							
[-]	[-]	[-]	[-]	[-]	[-]	[-]	[-]
X.XX	X.XX	X.XX	X.XX	X.XX	X.XX	X.XX	X.XX
1.00	1.00	1.00	1.00	1.00	1.00	1.00	1.00
*****							
SN( 1)SN( 2)SN( 3)SN( 4)SN( 5)SN( 6)SN( 7)SN( 8)SN( 9)SN(10)SN(11)SN(12)							
-----							
[-]	[-]	[-]	[-]	[-]	[-]	[-]	[-]
X.XX	X.XX	X.XX	X.XX	X.XX	X.XX	X.XX	X.XX
1.00	1.00	1.00	1.00	1.00	1.00	1.00	1.00
*****							
SN(13)SN(14)SN(15)SN(16)SN(17)SN(18)SN(19)SN(20)SN(21)SN(22)SN(23)SN(24)							
-----							
[-]	[-]	[-]	[-]	[-]	[-]	[-]	[-]
X.XX	X.XX	X.XX	X.XX	X.XX	X.XX	X.XX	X.XX
1.00	1.00	1.00	1.00	1.00	1.00	1.00	1.00
*****							

ANZ NR NR NR NR NR NR NR NR NR NR NR NR NR NR NR NR NR NR NR

-----

[-][-][-][-][-][-][-][-][-][-][-][-][-][-][-][-]

XX XX XX XX XX XX XX XX XX XX XX XX XX XX XX XX XX

A 4 1 15 19 6

W 1 1

W 1 1

W 1 1

W 1 1

W 1 1

K 1 1

K 1 1

K 1 1

B 1 1

I 1 1

I 0

F 1 1

F 1 1

F 1 1

## Appendix C

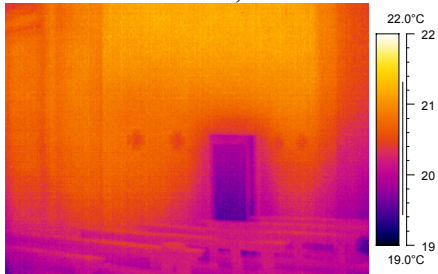
### Service attendance data

date	day	time	persons
20.10.2002	Sun	10:30	49
23.10.2002	Wed	17:30	9
27.10.2002	Sun	10:30	54
01.11.2002	Fri	10:30	86
01.11.2002	Fri	13:30	78
03.11.2002	Sun	10:30	70
06.11.2002	Wed	19:30	11
10.11.2002	Sun	10:30	75
13.11.2002	Wed	17:30	9
17.11.2002	Sun	10:30	63
20.11.2002	Wed	17:30	4
24.11.2002	Sun	10:30	65
27.11.2002	Wed	n.a.	n.a.
01.12.2002	Sun	n.a.	n.a.
04.12.2002	Wed	n.a.	n.a.
08.12.2002	Sun	10:30	74
11.12.2002	Wed	n.a.	n.a.
13.12.2002	Fri	15:00	155
15.12.2002	Sun	10:30	67
18.12.2002	Wed	n.a.	n.a.
22.12.2002	Sun	10:30	61
24.12.2002	Tue	22:00	160
25.12.2002	Wed	n.a.	n.a.
26.12.2002	Thu	n.a.	n.a.
29.12.2002	Sun	n.a.	n.a.
01.01.2003	Wed	n.a.	n.a.
05.01.2003	Sun	n.a.	n.a.
08.01.2003	Wed	n.a.	n.a.
12.01.2003	Sun	10:30	63
14.01.2003	Tue	15:00	160
15.01.2003	Wed	17:30	5
19.01.2003	Sun	10:30	76
22.01.2003	Wed	17:30	29
02.02.2003	Sun	10:30	70

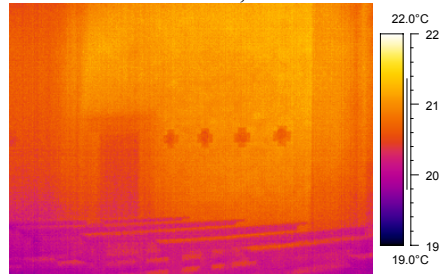
## Appendix D

### Examples of infrared thermographs

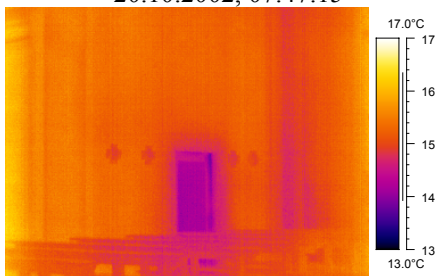
05.07.2002, 06:49:39



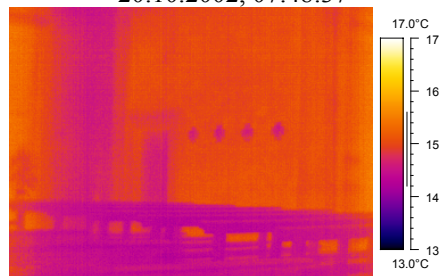
05.07.2002, 07:01:17



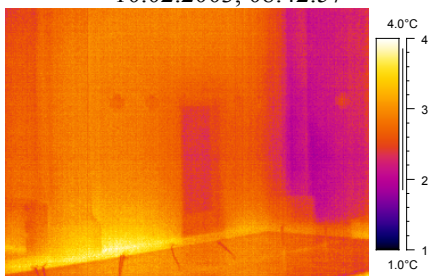
20.10.2002, 07:47:15



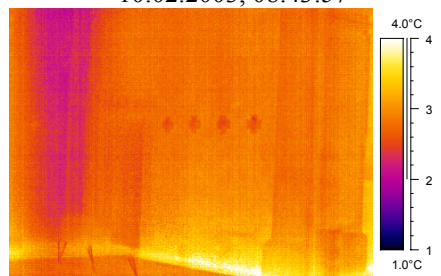
20.10.2002, 07:48:37



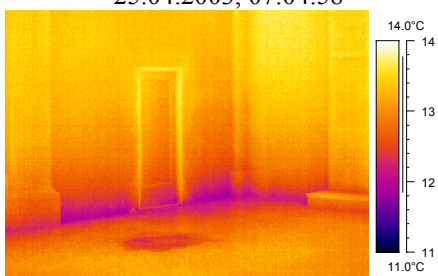
10.02.2003, 08:42:57



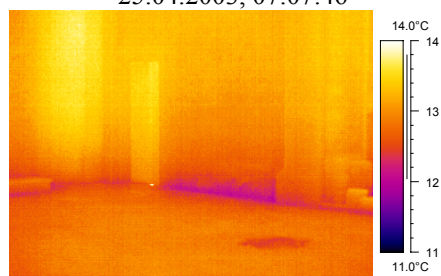
10.02.2003, 08:43:57



25.04.2003, 07:04:58



25.04.2003, 07:07:46



## Appendix E

### Theoretical description of the hygric model from Simmler et al. (1995; 1996)

Nomenclature	
$A$	surface area ( $\text{m}^2$ )
$b$	moisture transfer coefficient ( $\text{g h}^{-1} \text{m}^{-2} \text{Pa}^{-1}$ ), includes effective resistance of the active layer
$c_e$	moisture concentration of the outdoor air ( $\text{g m}^{-3}$ )
$c_i$	moisture concentration of the indoor air ( $\text{g m}^{-3}$ )
$c_{sat}$	saturation water vapour concentration ( $\text{g m}^{-3}$ )
$c_w$	moisture concentration in the pore volume ( $\text{g m}^{-3}$ )
$D$	diffusion coefficient of water in the material ( $\text{m}^2 \text{h}^{-1}$ )
$d$	thickness of the active material layer (m)
$j_s$	water vapour sorption flux ( $\text{g h}^{-1} \text{m}^{-2}$ )
$M$	mass of the hygroscopic material (g)
$\dot{m}_f$	moisture sorption of “fast” hygroscopic material ( $\text{g h}^{-1}$ )
$\dot{m}_q$	moisture sources flow rate ( $\text{g h}^{-1}$ )
$\dot{m}_s$	moisture sorption flow rate ( $\text{g h}^{-1}$ )
$n_L$	air change rate ( $\text{h}^{-1}$ )
$p_i$	water vapour pressure of the indoor air (Pa)
$p_{sat}$	saturation water vapour pressure (Pa)
$p_w$	water vapour pressure in the pore volume (Pa)
$R_D$	specific gas constant for water vapour ( $0.462 \text{ J g}^{-1} \text{K}^{-1}$ )
$s$	mean slope $du/d\phi$ of the sorption isotherm $u(\phi)$
$s_f$	mean slope of the sorption isotherm referred to the mass
$T_i$	temperature of the indoor air (K)
$T_w$	temperature of the active material layer (K)
$u_m$	moisture content relative to M (0-1)
$V_i$	indoor air volume ( $\text{m}^3$ )
$\beta$	water vapour transfer coefficient ( $\text{m h}^{-1}$ )
$\phi_i$	relative humidity of the indoor air
$\phi_w$	mean relative humidity in the pores of the material
$\sigma$	slope $du/dc$ of the sorption isotherm $u(c)$ ( $\text{g m}^{-3}$ )

A generalised moisture balance equation can be expressed as

$$\frac{dc_i}{dt} = n_L (c_e - c_i) + \frac{\dot{m}_q - \dot{m}_s}{V_i} \quad (6-34)$$

The 1-dimensional moisture transport between air and material surfaces can be described with the water vapour flux density

$$j_s = \beta (c_i(t) - c_w(x=0, t)) \quad (6-35)$$

and within hygroscopic materials, under isothermal conditions, by means of Fick's diffusion law (Crank, 1975)

$$\frac{\partial c_w}{\partial t} = \frac{D}{\sigma} \frac{\partial^2 c_w}{\partial x^2} \quad (6-36)$$

If the humidity of the air is raised abruptly, then the exact solution of (6-35) and (6-36) shows that the moisture content in a superficial layer of the material rapidly increases, possibly reaching saturation for a finite material thickness, according to the sorption isotherm.

An *active layer* of moderate thickness proportional to  $\sqrt{\tau}$  and homogeneous moisture content exists for a cyclic boundary  $c_i$  with period  $\tau$ . Thus, the present model accounts for material responses in a time interval  $\tau$  (no long-term behaviour). Cunningham (1992) discusses a similar two-node model and shows that for harmonic moisture variations with the period  $\tau$  the model gives the exact solution of the diffusion equation when the following effective penetration depth is applied

$$d_{eff} = \sqrt{\frac{D \tau}{4 \pi \sigma}} \quad (6-37)$$

The water vapour flux through the active layer and its moisture content are

$$\dot{m}_s = A \beta (c_i(t) - c_w(t)) \quad (6-38)$$

$$\frac{dc_w}{dt} = \frac{\beta}{d \sigma} (c_i(t) - c_w(t)) \quad (6-39)$$

By replacing vapour concentrations with pressures, the validity of (6-38) and (6-39) is extended to non-isothermal processes

$$j_s = b (p_i(t) - p_w(t)) \quad (6-40)$$

$$\frac{d\varphi_w}{dt} = \frac{b}{d s} (c_i(t) T_i(t) R_D - p_{sat}(T_w(t)) \varphi_w(t)) \quad (6-41)$$

The layer thickness  $d$ , the moisture transfer coefficient  $b$  and the slope of the sorption isotherm  $s$  can be determined experimentally.

The effect of hygroscopic materials with fast moisture uptake capacity (e.g. textiles) is described as follows (Simmler, to be published)

$$\dot{m}_f = M \dot{u}_m = M \frac{du_m}{d\varphi} \dot{\varphi}_i = M s_f \dot{\varphi}_i \quad (6-42)$$

With the variation of the indoor relative humidity with time

$$\dot{\varphi}_i = \frac{\dot{c}_i}{c_{sat}(t)} - \frac{c_i}{c_{sat}^2} \dot{c}_{sat} \quad (6-43)$$

then the moisture balance equation (6-34) becomes

$$\left(1 + \frac{M s_f}{V_i c_{sat}}\right) \dot{c}_i = n_L (c_e - c_i) + \frac{\dot{m}_q - \dot{m}_s}{V_i} + \frac{M s_f}{V_i c_{sat}^2} \dot{c}_{sat} c_i \quad (6-44)$$

### Determination of the hygric properties of materials

The increase in water content of a test material with surface  $A$ , following an abrupt raise of the relative humidity of the air, is given by

$$\dot{m} = A d s \dot{\varphi}_w \quad (6-45)$$

by combination with the water vapour flux density (6-40)

$$\dot{m}(t) = A b p_{sat}(T) (\varphi_i - \varphi_w(t)) = \frac{b p_{sat}(T)}{d s} (m_i - m(t)) \quad (6-46)$$

with

$$m_i = A d s \varphi_i \quad (6-47)$$

The solution of (6-46) is

$$m(t) - m(0) = \Delta m (1 - e^{-t/\tau}) \quad (6-48)$$

with

$$1/\tau = \frac{b p_{sat}}{d s} \quad \text{and} \quad (6-49)$$

$$\Delta m = A d s \Delta \varphi \quad (6-50)$$

$\Delta m$  and  $\tau$  can be obtained by fitting (6-48) to experimental data. The value of  $b$  and the product  $d s$  are calculated using (6-49) and (6-50).

## Appendix F

### XRD analyses

Analyses performed by the Institute for Geotechnical Engineering of the ETH.

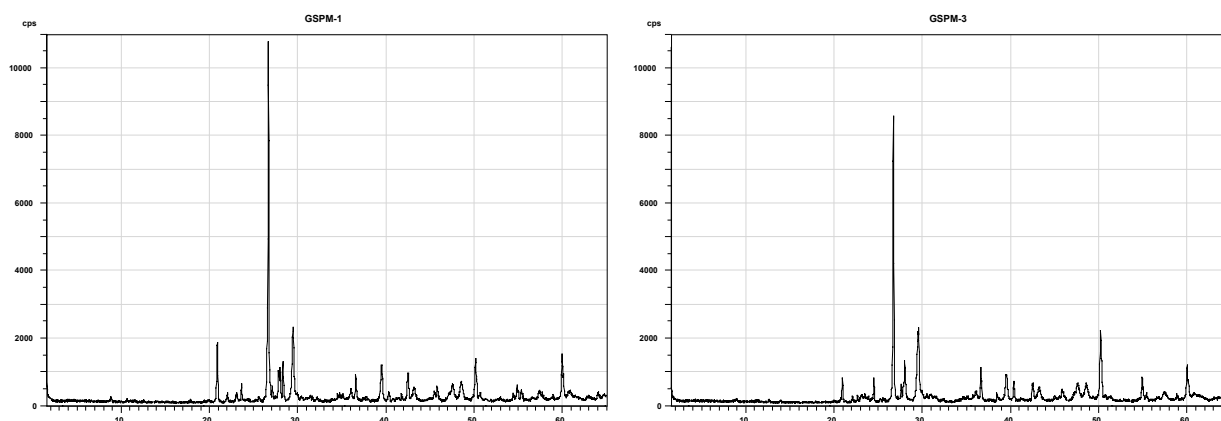
#### Sample preparation

About 2 g of the dry material were ground to a grain-size  $< 20 \mu\text{m}$  using a McCrone mill under addition of ethanol. Unoriented mounts were prepared from the dry powder. The samples were then analysed using a Philips PW1820 X-ray diffractometer fitted with a copper anode ( $\text{CuK}\alpha$  radiation, 40 kV, 30 mA) in Bragg-Brentano geometry. The diffractograms were recorded in the range  $1.5\text{--}65^\circ 2\theta$  by proceeding in steps of  $0.02^\circ 2\theta$  with a count time of 3 s per step. The qualitative analysis of the mineral phases was performed using the software DIFFRACplus (Bruker AXS). The phases were identified using the ICDD database on the basis of peak location and relative intensity. The quantitative determination of the relative percentages of each phase was carried out using the Rietveld software AutoQuan (Seifert) and has an accuracy of  $\pm 2\%$ .

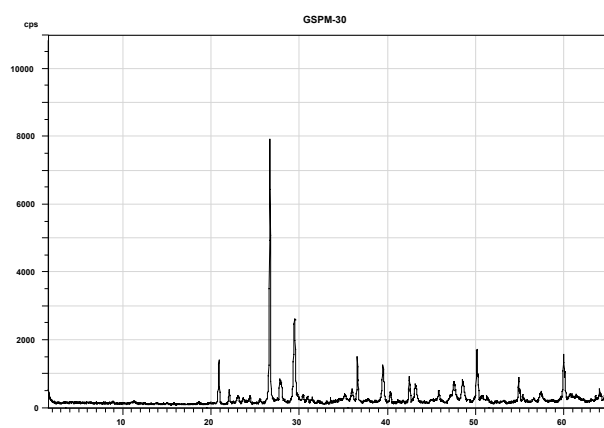
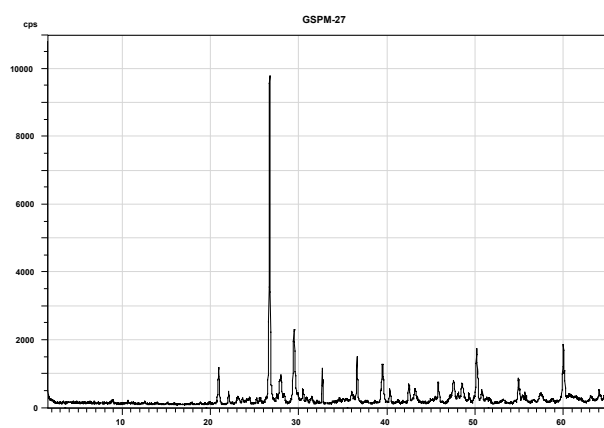
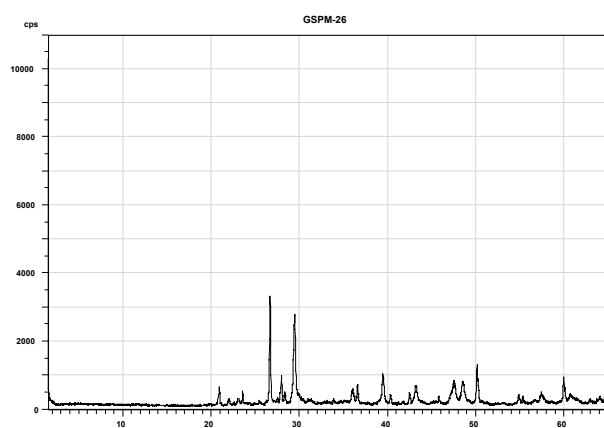
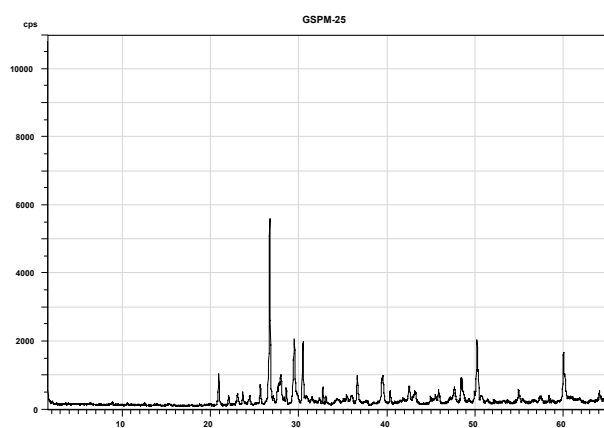
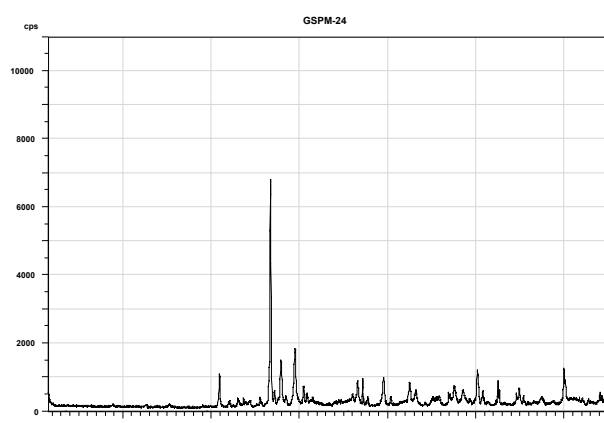
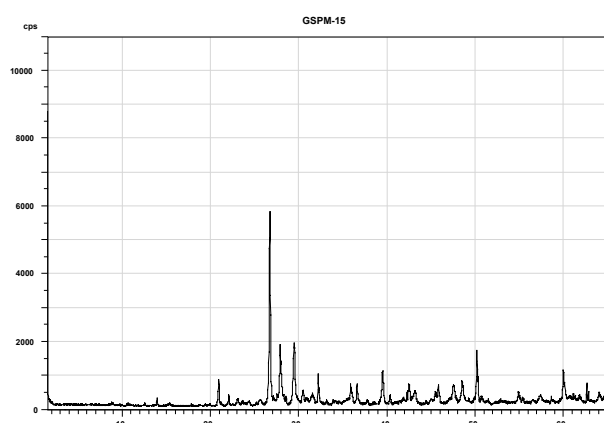
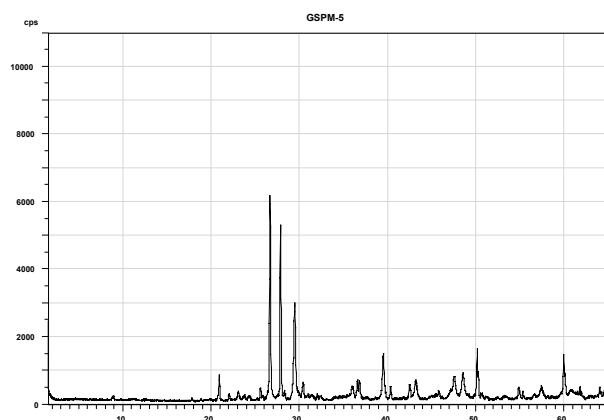
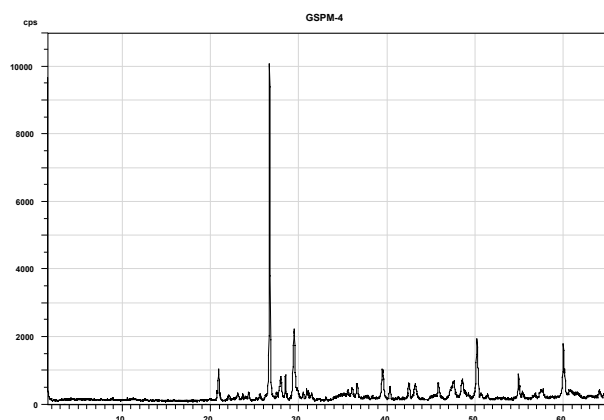
#### Quantitative determination

Sample	Calcite (+ dolomite, $< 1\%$ )	Feldspar	Quartz (+ cristobalite)	Mica (biotite + muscovite)	Other
	%	%	%	%	%
1	23	24	43	10	0
3	31	24	38	7	0
4	30	18	43	8	1
5	38	16	37	9	0
15	28	26	39	7	0
24	26	23	37	12	2
25	23	33	35	8	1
26	47	20	28	5	0
27	25	21	45	8	1
30	32	19	41	7	1

#### Diffractograms







## Appendix G

### Porosity data

The determination of the porosity was carried out by Expert-Center pour la Conservation du Patrimoine Bâti, EPFL, CH-1015 Lausanne.

$N_t$  = total connected porosity (RILEM I.1, 1978)

$N_{Hg}$  = mercury intrusion porosity (RILEM I.5, 1978)

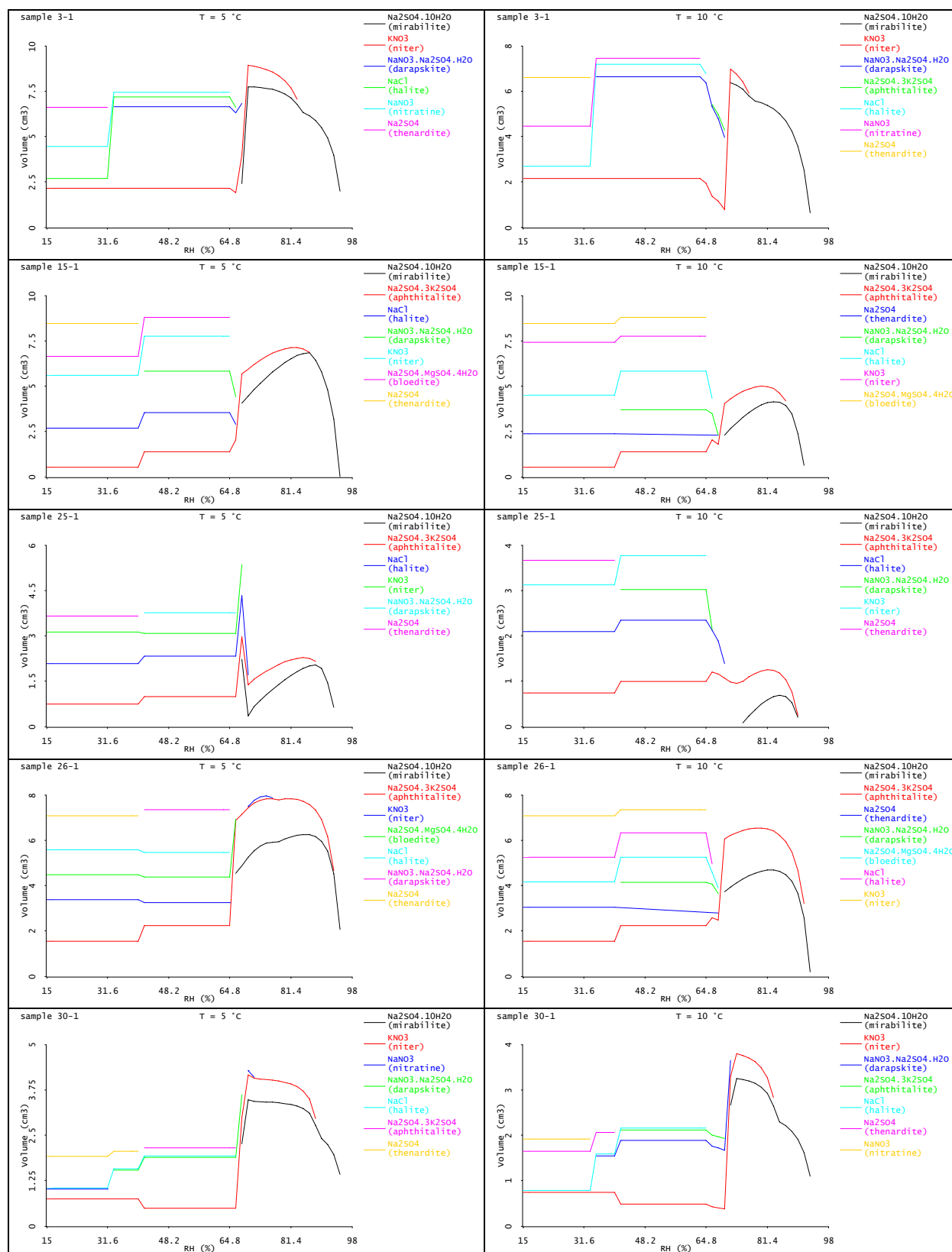
$N_{48}$  = 48-hours capillary suction porosity (on the basis of RILEM II.1, 1978)

sample	$N_t$ (vol.-%)	$N_{Hg}$ (vol.-%)	$N_{48}$ (vol.-%)	density ( $\text{g cm}^{-3}$ )	description
1	26.0	18.6	21.1	1.91	cement plaster
3	20.1	21.3	19.0	2.07	cement plaster
4	29.3	7.5	27.3	1.88	cement plaster
5	24.3	26.5	22.5	1.95	cement plaster
15	32.7	22.5	24.0	1.77	cement plaster
16	26.7	23.3	24.1	1.96	cement plaster
18	28.0	27.9	21.6	1.90	cement plaster
24	30.4	24.2	25.5	1.80	cement plaster
25	34.2	27.8	24.7	1.75	cement plaster
26	29.0	26.3	23.3	1.86	cement plaster
91	24.0	26.3	19.3	2.04	cement plaster
92	33.9	16.8	26.7	1.78	cement plaster
93	39.8	32.5	31.7	1.59	cement plaster
94	31.2	28.4	26.1	1.84	cement plaster
mean	29.3	23.6	24.1	1.9	
standard deviation	5.0	6.2	3.4	0.1	

# Appendix H

## ECOS results

Plasters sampled on the 25.4.2003. The efflorescing salt was mirabilite/thenardite.



# Appendix I

## The RUNSALT program

RUNSALT version 1.8, July 2005  
Copyright (c) 2002-2005 by Davide Bionda  
e-mail: bionda@arch.ethz.ch

```
=====
FILES IN THIS DISTRIBUTION
=====
- This file (README.TXT)
- RUNSALT.EXE
- salt.bat
- xlisp.wks
- COPYING
```

```
=====
WHAT IS IT?
=====
```

RUNSALT is a front end to the program SALT included in the ECOS package as described in Price, C. A. (Ed.), 2000: "An expert chemical model for determining the environmental conditions needed to prevent salt damage in porous materials". European Commission Research Report No 11, (Protection and Conservation of European Cultural Heritage). Archetype Publications, London.

```
=====
PROGRAM AVAILABILITY
=====
```

Free of charge. See below for distribution restrictions.  
Please acknowledge its use by an appropriate citation in any reports, publications, or other disclosure of results obtained with it.

```
=====
SYSTEM REQUIREMENTS
=====
```

Any 32-bit MS-Windows operating system (95, 98, ME, NT, 2000, XP\*).

\*IMPORTANT NOTE: although RUNSALT will run on Windows XP, the SALT executable from the ECOS distribution won't (it generates an abnormal program termination: stack fault CS:EIP = 000Fh:00001373h). If you plan on using the program on Windows XP, ask for an updated SALT executable.

```
=====
INSTALLATION
=====
```

No special installation necessary: move the RUNSALT directory to a convenient place on your hard disk and copy the file SALT.EXE from your personal ECOS distribution into it.

```
=====
PROGRAM USE
=====
```

Launch RUNSALT by double-clicking the RUNSALT icon. In addition to the self-explanatory menu items, Undo, Cut, Copy, Paste, Delete and Select All commands are available by clicking the right mouse button in the data input window. Clicking the mouse in the plot window will show the coordinates. If you prefer to have the program launched with maximized window (for example because your monitor resolution is less than 1024 by 768 pixels), create a shortcut to it, change the "Run" attribute in the "Property" dialog of the shortcut to "Maximized", then launch RUNSALT with the shortcut.

```
=====
SAVING DATA INPUT FILES
=====
```

The files are saved in standard ASCII format and can be viewed with any text editor. For your convenience, save them with the \*.txt extension or with the extension associated with your favourite text editor. Don't use an editor to modify them unless you know what you are doing.

```
=====
KNOWN PROBLEMS
=====
```

Pressing the ESC key while the input dialog is the active window will close it. This is a "feature" of the programming environment, there is no remedy at the time. If this happens, just quit and re-launch RUNSALT.

```

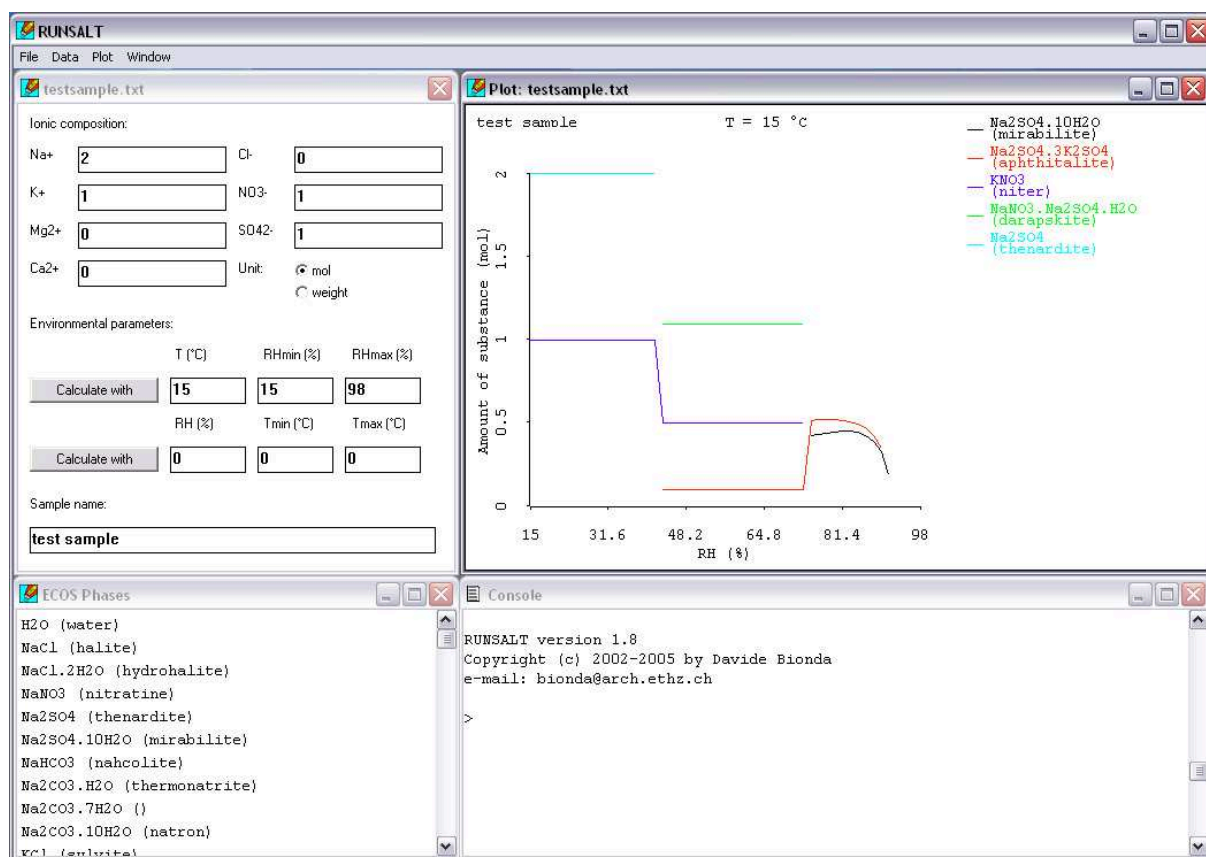
=====
AUTHOR
=====
Davide Bionda
bionda@arch.ethz.ch
Institute of Monument Conservation
Research Group for Conservation Science and Technology
Swiss Federal Institute of Technology (ETH)
Zürich, Switzerland

=====
CONTACT INFORMATION
=====
Please send all comments, questions or suggestions to me at bionda@arch.ethz.ch

=====
COPYING RUNSALT
=====
RUNSALT is Freeware. However, RUNSALT is still Copyright (c) 2002-2005 by Davide
Bionda. All rights reserved. You may not sell this program without the author's
permission. RUNSALT may be distributed freely, except where noted above,
provided it is distributed unmodified and with this README file.
RUNSALT was written in Lisp on a foundation consisting of XLISP and XLISP-STAT.
See the file COPYING for the license agreement for XLISP and XLISP-STAT.

=====
DISCLAIMER
=====
YOU EXPRESSLY ACKNOWLEDGE AND AGREE THAT USE OF RUNSALT IS AT YOUR EXCLUSIVE
RISK. RUNSALT, ANY RELATED FILES AND DOCUMENTATION ARE PROVIDED "AS IS" AND
WITHOUT ANY WARRANTY OF ANY KIND, EXPRESSED OR IMPLIED, INCLUDING, BUT NOT
LIMITED TO, THE IMPLIED WARRANTIES OF MERCHANTABILITY AND FITNESS FOR A
PARTICULAR PURPOSE.

```



# Curriculum Vitae

## **Davide Bionda**

Date of birth: 16 September 1968

Place of birth: Bellinzona TI

Nationality: Swiss

## **Education**

2002 - 2006      PhD Thesis at the Institute of Monument Conservation, ETH Zürich.  
Title of the thesis: Modelling Indoor Climate and Salt Behaviour in  
Historical Buildings: A Case Study.  
Examiners: Prof. Dr. Georg Mörsch, Prof. Dr. Renato Zenobi and  
Dr. Hans Simmler.

1990 - 1996      Diploma in geology at the University of Zürich.  
Title of the Thesis: Stable Isotope Geochemistry of the Middle Triassic  
Kalkschieferzone, Southern Alps (Ticino, Switzerland).  
Advisors: Prof. Dr. Daniel Bernoulli, Dr. Stefano Bernasconi,  
Dr. Heinz Furrer and Prof. Dr. Judith A. McKenzie.